This electronic thesis or dissertation has been downloaded from the King's Research Portal at https://kclpure.kcl.ac.uk/portal/

Using electrostatic interactions to control supramolecular self-assembly on metallic surfaces

Riello, Massimo

Awarding institution:
King's College London

The copyright of this thesis rests with the author and no quotation from it or information derived from it may be published without proper acknowledgement.

END USER LICENCE AGREEMENT

Unless another licence is stated on the immediately following page this work is licensed under a Creative Commons Attribution-NonCommercial-NoDerivatives 4.0 International licence. https://creativecommons.org/licenses/by-nc-nd/4.0/

You are free to copy, distribute and transmit the work

Under the following conditions:

- Attribution: You must attribute the work in the manner specified by the author (but not in any way that suggests that they endorse you or your use of the work).
- Non Commercial: You may not use this work for commercial purposes.
- No Derivative Works - You may not alter, transform, or build upon this work.

Any of these conditions can be waived if you receive permission from the author. Your fair dealings and other rights are in no way affected by the above.

Take down policy

If you believe that this document breaches copyright please contact librarypure@kcl.ac.uk providing details, and we will remove access to the work immediately and investigate your claim.

Download date: 01. Jan. 2025

King's College London
University of London

Using electrostatic interactions to control supramolecular self-assembly on metallic surfaces

by

Massimo Riello

A Thesis submitted in partial fulfillment for the
degree of Doctor of Philosophy

in the

School of Natural & Mathematical Science
Department of Physics

2013

Declaration of authorship

I, Massimo Riello, declare that this Thesis, which I submit to King's College London in partial fulfillment of my application for the Degree of Doctor of Philosophy, composes the original work completed under the supervision of Prof Alessandro De Vita.

I certify that the work here presented was entirely done during my permanence as a PhD candidate at King's College, from June 2010 to June 2013.

I declare that this Thesis is based entirely on my own original work. Where contributions from collaborators are used, the extent and quality of their assistance is clearly stated and acknowledged.

All the work presented here is original and was not previously submitted as an application for a degree or other qualification in any other institution.

Part of the work presented here was published or submitted for publication:

- S. Kervyn, N. Kalashnyk, M. Riello, B. Moreton, J. Tasseroul, J. Wouters, T. S. Jones, A. De Vita, G. Costantini and D. Bonifazi, *"Magic" surface clustering of borazines driven by repulsive intermolecular forces*, Angew. Chem. Int. Ed. **52**, 7410 (2013)
- A. Della Pia, M. Riello, A. Floris, D. Stassen, T. S. Jones, D. Bonifazi, A. De Vita and G. Costantini, *Anomalous coarsening driven by reversible charge transfer at metal-organic interfaces*, Submitted.

Signed:

Date:

Abstract

Supramolecular self-assembly on metallic surfaces is the ideal playground for studying a variety of physical and chemical phenomena. Adsorbed molecules will diffuse and self-organise to form assemblies dictated by their functionalities, while the more or less pronounced metal reactivity will accordingly affect both the supramolecular patterns and the interfacial chemistry. Besides structural aspects, electronic properties are central in determining the energy level alignment at the heterojunction and, thus, the performance of organic-based devices. Notably, charge reorganisation at the metal-organic interface will produce surface dipoles, whose effect is to add electrostatic repulsion to the dispersion-driven supramolecular self-assembly and to change the work function of the surface.

Herein, the relation between charge migration (*i.e.*, the creation of surface dipoles) and molecular self-assembly is addressed by studying the behaviour of on-purpose designed molecular units on selected metals. We will show that choosing the substrate on the basis of its work function can selectively allow or inhibit the transfer of charge from the organic material to the electrode. When charge transfer occurs, the growing supramolecular structures exhibit a phase modulation driven by the presence of competing interactions. Moreover, the introduction of reactive moieties in formerly inert *tectons* will be identified as a suitable strategy for promoting the formation of interfacial dipoles upon surface-mediated chemical reactions. Our work paves the way for a more rational approach to the design of metal-organic systems, as we speculate that charge transfer effects and surface chemistry can be predicted at the stage of molecular design, at variance with the current trial and error approach used in the field of organic electronics.

This thesis is based on multiscale theoretical modelling of selected metal-molecule couples and it is the result of a fruitful collaboration with the groups of Prof Davide Bonifazi (Université de Namur) and Prof Giovanni Costantini (University of Warwick).

Contents

List of figures

Abbreviations

CNL: **C**harge **N**eutrality **L**evel

DFT: **D**ensity **F**unctional **T**heory

DOS: **D**ensity **O**f **S**tates

GGA: **G**eneralised **G**radient **A**pproximation

HOMO: **H**ighest **O**ccupied **M**olecular **O**rbital

IDIS: **I**nduced **D**ensity of **I**nterfacial **S**tates

ICT: **I**nteger **C**harge **T**ransfer

LDA: **L**ocal **D**ensity **A**pproximation

LUMO: **L**owest **U**noccupied **M**olecular **O**rbital

MC: **M**onte **C**arlo

OFET: **O**rganic **F**ield **E**ffect **T**ransistor

OLED: **O**rganic **L**ight **E**mitting **D**iode

OMBE: **O**rganic **M**olecular **B**eam **E**pitaxy

PAH: **P**oly-**A**romatic **H**ydrocarbon

pDOS: **p**rojected **D**ensity **O**f **S**tates

STM: **S**canning **T**unneling **M**icroscopy

STS: **S**canning **T**unneling **S**pectroscopy

TBP: tetra[1,3-di(*tert*-**b**utyl)-phenyl]-**p**yrene

TCNQ: 7,7,8,8-**t**etra**c**yano**q**uinodimethane

UEG: **U**niform **E**lectron **G**as

vdW-DF: **v**an **d**er **W**aals **D**ensity **F**unctional

XPS: **X**-ray **P**hotoelectron **S**pectroscopy

Chapter 1

Supramolecular self-assembly on metal surfaces

The ability of generic elements to self-assemble (self-organise) can be defined as their aptitude to autonomously evolve into structures and patterns, with the only guidance of the information enclosed in the elements themselves (*i.e.*, without external direction) [1]. This general definition can be restricted to the field of organic chemistry, where the idea of self-assembly is indisputably linked to the formation of non-covalent molecular architectures. Indeed, the origins of the paramount interest in the research field of self-assembly are to be sought in its routine occurrence in a variety of biological processes fundamental in any living organism, such as the organisation (and reorganisation) of carbon-based molecules in specific higher-level structures [2].

The requirement that the knowledge necessary for the structural development of a physical system has to be embedded in its molecular components makes supramolecular self-assembly a prototypical *bottom up* fabrication technique, at variance with the commonly applied construction methods, whose *top down* approach consists of shaping a material from the bulk to the desired product [3]. Here lays the importance of bottom up technologies: suitable molecular building blocks can be tailored to contain the planned *a priori* information, which then drives the autonomous evolution to the desired “product” with a high degree of precision and reproducibility. Needless to say, the full understanding and control of matter at the atomic scale is necessary for handling bottom up nanofabrication. The technological improvements occurred in the last few decades – such as the invention of *scanning tunneling microscopy* (STM) [4,5,6], which allowed high resolution visualisation and manipulation down to the single atom level, together with advances in the synthesis of chemicals and nanomaterials with unprecedented properties – greatly improved the knowledge of structural and physical properties of such small systems [7].

These insights allow us to predict a new and more important role of nanotechnology, which might in the future answer the demands of continuous miniaturisation of devices, especially in the field of nanoelectronics [8,9]. However, the pursued development of new fabrication techniques – covering the 0.1–100 nm scale – will have to match the scalability, performances, reliability and cost effectiveness required for industrial applications, which calls for more in-depth efforts in studying the control of supramolecular self-organisation.

In this work, we aim to develop a highly novel approach to control the self-assembly of organic molecules at the metal surface and to understand related electronic effects, such as charge transfer. This knowledge will provide new elements useful to unravel the fundamental mechanisms involved in the energy level alignment at the metal-organic interface, which is central to determine the performances of organic-based optoelectronic devices. Moreover, it will be shown how charge transfer affects the organisation of adsorbed molecules, by the competition between short-range van der Waals-like attraction and electrostatic repulsion. Long-range interactions are important to extend the control of molecular self-assembly to length scales that are larger than the nearest neighbour, in the view of making the integration of bottom up and top down nanofabrication possible [10,11]. Our methodology will combine the chemical synthesis of suitable molecular units, the application of scanning probe techniques for the production and characterisation of organic thin films and theoretical modelling to assist the stage of molecular design and help the rationalisation of experimental observations. In particular, we will investigate whether long-range electrostatic forces between charged molecules can drive the formation of novel classes of supramolecular structures. At the same time, the observation of specific self-assembled patterns will reveal the occurrence of charge reorganisation at the metal-organic interface, providing useful information about the system's electronic properties.

1.1 Basic concepts in "on the surface" self-assembly

Many bottom up nanofabrication techniques start with the deposition of atoms or molecules on a substrate. In fact, these methods are based on the time-growth of structures, whose development is the result of the complex interplay between a wide range of atomistic processes. A balance between kinetics and thermodynamics will most likely control the structural evolution of self-assembling systems on surfaces, which can be regarded as an archetypal non-equilibrium process. In fact, interacting particles adsorbed on a substrate might experience kinetic limitations to their self-organisation (*e.g.*, due to strong coordination with the substrate itself), with the effect of hampering the spontaneous evolution of the system to its thermodynamic equilibrium [11].

The deposition of thin layers of molecules is routinely performed by *organic molecular beam epitaxy* (OMBE), an ultrahigh vacuum technique with which a gaseous molecular beam is generated upon thermal sublimation of a crystal powder. This step is followed by the actual growth of nanostructures, via transport and aggregation of particles on the surface. Of course, the transport of adsorbates implies that random hopping events are allowed, meaning that surface diffusion needs to be activated at the system temperature [12,13]. As a consequence, the diffusivity of adsorbates (defined as the mean square distance covered per unit time) will be described by an Arrhenius relation [14]: mobility on the surface is allowed or increased by supplying thermal excitation sufficient to overcome the energy barrier for moving a particle from an adsorption site to another, which is related to the surface reactivity and geometry.

Since we are interested in the study of systems approaching the thermodynamic equilibrium, our focus will be on the growth of nanostructures from the autonomous organisation of mobile molecular units, which are deposited at low rates on metal surfaces, so that the nucleation and coarsening of self-assembled aggregates will have the time necessary to reach a stable minimum energy configuration and to avoid kinetic limitations [15]. In this Chapter we will outline a brief introduction on concepts that are important to define the field in which our research work is located. In particular, we will provide a description of the metal-organic interface, by having a look at the fundamental phenomena related to the formation of supramolecular structures.

1.1.1 *Engineering self-assembling molecular units*

Single atoms are the smallest unit that can be used to grow potentially interesting nanostructures by means of self-organisation. This is usually obtained from the deposition of metal atoms on metal surfaces, provided that the mixing of the two species is unfavourable enough to prevent the formation of superficial alloys. However, the shape and size control of metal nanostructures is severely inhibited by the low selectivity of their self-organisation, which is inherent to their tendency to strongly coordinate with any neighbouring object (*i.e.*, kinetically limited self-assembly) [16].

On the contrary, a much higher degree of control can be achieved by using molecular units as self-assembling elements, since molecules interact with one another mainly via weak non-covalent coordination, whose strength and directionality can be fine-tuned at the stage of molecular design to give desired supramolecular patterns [11,17,18]. Synthetic chemistry gives access to a potentially unlimited range of molecular building blocks (*tectons* [19]), in which the desired self-assembly behaviour can be programmed by the *ad hoc* insertion of functional groups to promote the formation of, *e.g.*, hydrogen bonds [20], coordination chemistry [21], π stacking interactions [22] and other general dispersion forces. Even if the strength of these interactions, as a single contribution, is typically one order of magnitude lower than covalent coordination, the synergic cooperation of dispersion forces organised in ordered networks can lead to stable minimum energy structures. In addition, molecular symmetries and chirality [23] may be designed and used to transfer selected regularities to the supramolecular assembly (*e.g.*, formation of low dimensional structures [24] or porous two-dimensional crystals [25]). Nevertheless, the weak interactions regime proper of intermolecular coordination is both supporting and limiting the foreseen application of supramolecular structures in real-life devices. For instance, while the weak bonding confers important properties such as reversibility and the ability of self-correcting reticular defects [15], on the other hand, this structural flexibility – associated with thermal fluctuations – limits the stability of the supramolecular aggregates to low temperatures only.

The inherent short-range character of the intermolecular interactions mentioned above does not allow the control of molecular organisation beyond the sub-nanometric scale, which would be useful for the integration of these supramolecular structures with traditional top down fabrication [11]. Neglecting surface effects, the self-organisation of molecular units in the mesoscale (*i.e.*, 10 nm and above) can be achieved by incorporating long-range terms – such as electrostatic interactions between “charged adsorbates” – in the intermolecular interaction potential, as they are expected to promote structural reorganisation up to hundreds of Å length. Long-range forces are usually related to phenomena such as energy level alignment at the metal-organic interface or surface mediated chemical reactions [26,27], whose fundamental importance in organic electronics and heterogeneous catalysis increases the interest in understanding and controlling these electronic effects well beyond the mere supramolecular structure regulation.

Beside intermolecular interactions, another parameter controlling the self-assembly of adsorbed molecules is their mobility on the metal surface, which is dependent on the physical nature of the metal-organic coordination. The high degree of control in the synthesis of chemicals – and their consequent intermolecular interactions – cannot be generally transferred to the metal surface without taking into account the occurrence of effects related to the surface geometry, electronic properties and coordination chemistry, which may themselves play a role in the formation of supramolecular structures [11,28,29]. Moreover, metal-organic interactions can occasionally modify the electronic surface states, affecting the adsorption of molecules [30]. Similar effects are observed when the metal reactivity promotes chemical modifications in the adsorbate. In this case, the topology of the surface may also play an important role by offering preferential adsorption sites to reactive molecular moieties, with contribution to the total adsorption energy of small molecules of 0.3–5 eV per functional group [31].

In conclusion, the self-assembly of molecules on metals will depend on the chemical structure of the adsorbate, as well as on the substrate properties, making the rules governing the behaviour of molecules either in solution, or as a molecular crystal not directly applicable upon adsorption [32]. Therefore, while the design of functional molecular units is still a valuable tool to engineer the non-covalent interaction network, the choice of the metal substrate is also important in controlling supramolecular self-assembly, with both structural and electronic impacts.

1.2 Adsorption of organic molecules on metal surfaces

Supramolecular self-assembly is investigated primarily by means of STM experiments, where molecules are deposited and imaged on pristine metal surfaces prepared by cleavage along well defined crystallographic orientations. Metal atoms at the surface experience a bond deficiency that gives them a strong tendency to saturate their under-coordination by establishing interactions with any neighbouring matter. Adsorption is thus a process where atoms or molecules will interact with a proximal metal surface, experiencing different degrees of coordination (spanning from weak dispersion forces to covalent bonding).

It is then clear that – in the presence of adsorbed molecules – the metal substrate would not simply act as a steric constraint supporting the formation of two-dimensional structures, but it would rather interact with the adsorbate to the limit of overcoming the role of intermolecular forces in determining the evolution of supramolecular self-assembly. In the following Sections we will give a brief outline of the properties of metallic surfaces and their interactions with molecular species.

1.2.1 *Metal surfaces*

Metals are solid materials where atoms are mutually sharing valence electrons. These electrons are delocalised across a regular lattice of atoms, which tends to organise in dense, close-packed structures because of the lack of directionality in their coordination (metallic bond). The origin of the electronic delocalisation is found in the substantial overlap between valence orbitals in metal atoms, with the important consequence of creating the strong dispersion of electronic wavefunctions (bands) – in the reciprocal **k**-space – responsible for the good electronic conductivity of such materials.

Obviously, the presence of discontinuities such as surfaces will deeply modify the properties of the bulk, because of the interruption in the periodicity of the metal crystal. For instance, the electronic description of surfaces in *s* and *p*-block metals is provided by the *uniform electron gas* (UEG) model, where the charge of the ionic lattice is approximated by a uniform electrostatic potential. In correspondence to a surface, the electronic density is predicted to leak in the vacuum region due to the sudden fall of the nuclear electrostatic potential. The electronic profile is expected to readily return to the bulk value inside the slab, with some dumped fluctuation before stabilising to the asymptotic value (Friedel oscillations). This behaviour generates a small accumulation/depletion of charge density in the region immediately above/below the surface plane, and thus of a dipole layer. In particular, the magnitude of the surface dipole will be related to the atomic displacement at the interface, with important consequences on its electronic properties such as the work function ϕ [33,34], *i.e.*, the thermodynamic work required to move one electron from the metal to the vacuum at zero temperature, according to Eq. 1.1 below:

$$\phi \equiv eV(\infty) - E_{\mathrm{F}} , \tag{1.1}$$

where E_{F} is the Fermi energy of the surface, *i.e.*, the thermodynamic work required to remove the charge, while $V(\infty)$ is the electrostatic potential in the vacuum, which may be non-zero (thus giving a $eV(\infty)$ contribution to the electron energy, Fig. 1.1 left).

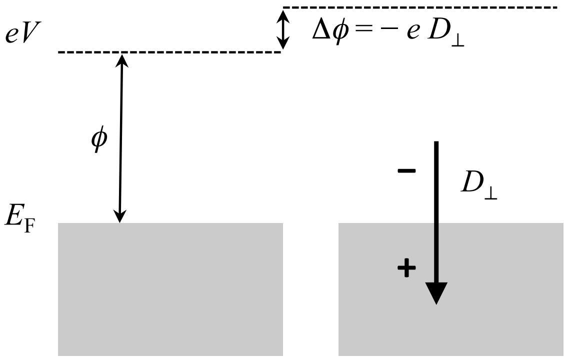

Figure 1.1 Energy level diagram for a generic metal surface (left). The work function shift $\Delta\phi$ caused by a *negative* dipole layer (black arrow) is sketched in the right panel.

The presence of a surface dipole will affect the work function by modifying the electrostatic potential profile at the metal-vacuum interface (Fig. 1.1 right), which will effectively shift the vacuum energy (Eq. 1.2):

$$\phi = \left[eV(\infty) - E_{\mathrm{F}}\right] + \Delta\phi \tag{1.2}$$

$$\Delta\phi = -eD_{\perp} , \tag{1.3}$$

where $\Delta\phi$ is the work function shift induced by the dipole moment of the layer, taking its component normal to the surface $D_{\perp}$ (Eq. 1.3) [35]. This means that the work function of a metal surface will be related to the strength of the electron binding to the bulk, as well as to the magnitude and nature of the surface dipole. The latter effect will be further detailed due to its importance in our investigations.

The limits of the UEG model become evident when approaching the description of *d*-bonded metals, where this approximation fails to give good description of their work function because of the reduced delocalisation of valence electrons, which are more bound to the nuclear positions. For such systems, the uniform ionic potential used in the UEG model has to be substituted with a periodic one, to take into account of the ionic lattice.

The structural stability of the surface is usually measured in terms of the energy needed for its creation per unit area, *i.e.*, the energetic penalty for breaking the bonds required for the cleavage of the bulk crystal. Therefore, the surface energy (γ) needed to split a crystal along different Miller directions will be lower for densely packed surfaces, as long as less bonds need to be broken. Furthermore, the creation of a surface is generally accompanied by more or less pronounced structural rearrangements. In fact, the under-coordination of the superficial atoms causes their displacement from the equilibrium bulk positions in order to minimise the system energy. This rearrangement may result in a simple shift of the frontier atoms towards or outwards the surface plane, or induce a more complex scenario, involving lateral displacements together with the variation of the interfacial atomic density. The latter effect is known as surface reconstruction, which is observed to occur on the dense Au(111) surface, with the formation of a peculiar herringbone pattern [36,37].

1.2.2 *Physisorption*

Molecules are generally adsorbed on metallic surfaces with different binding energies, whose magnitude is used as a criterion to distinguish between different adsorption types. Adsorption is usually referred to as *physisorption* when the binding energy does not exceed a few tenths of an eV, while values of 1 eV or more are generally associated with *chemisorption*.

Physisorption of particles on a metal surface is a weak physical binding, which does not yield substantial changes in the electronic structure of the adsorbate. The interaction forces involved in this adsorption process are short-range van der Waals contributions, generated by the attraction of the induced/permanent dipole moment of the adsorbate and its mirror image in the highly polarizable metal slab. Thus, physisorption can be easily understood by using the method of *image charge* to describe the interaction of a single hydrogen atom with an infinitely polarizable surface (Fig. 1.2).

In this simple system, the positive nucleus will have position $\mathbf{R} = (0, 0, Z)$, which is the centre of rotation of the electron located in $\mathbf{r} = (x, y, z)$. Both the nucleus and the electron will interact with their mirror images in the conductive solid (the mirror electron being located in $\mathbf{r}'$), with total electrostatic energy calculated as follow:

$$E_{im} = -\frac{e^2}{4\pi\varepsilon_0}\left[\frac{1}{|2\mathbf{R}|} + \frac{1}{|2\mathbf{R}+\mathbf{r}+\mathbf{r}'|} - \frac{1}{|2\mathbf{R}+\mathbf{r}|} - \frac{1}{|2\mathbf{R}+\mathbf{r}'|}\right], \qquad [1.4]$$

where ε_0 is the vacuum dielectric constant. The two attractive terms in Eq. 1.4 account for the interaction between the nucleus/electron and its image.

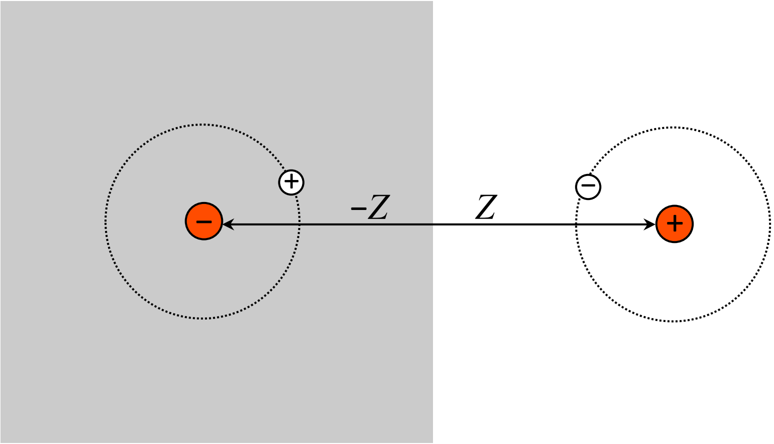

Figure 1.2 A single hydrogen atom in front of an ideal conductor (grey box) according to the image charge model (adapted from [38]).

Under the limit of adsorption distance larger than the electronic oscillation ($|\mathbf{R}| \gg |\mathbf{r}|$), the van der Waals binding energy can be calculated by modelling the electron motion with the simple oscillator model (Eq. 1.5):

$$E_{im} \approx E_{vdW} = -\frac{\hbar\alpha\omega}{16\pi\varepsilon_0 Z^3} = -\frac{C_{vdW}}{Z^3} \quad , \qquad [1.5]$$

where ω is the vibrational frequency of the electron. Eq. 1.5 shows that the van der Waals constant C_{vdW} is proportional to the atomic polarisability α, together with the Z^{-3} dependence of E_{vdW}. By taking into account of higher order corrections in the Taylor expansion of Eq. 1.4, it is possible to identify another important property of the metal surface, *i.e.*, the *image plane* Z_{im} (Eq. 1.6):

$$E_{vdW} = -\frac{C_{vdW}}{\left(Z - Z_{im}\right)^3} + O\left(Z^{-5}\right) \ . \qquad [1.6]$$

The image plane finds its origin in the spilling of electronic tails from the metal into the vacuum. This quantity corrects the position of the metal surface and allows for the application of classical electrostatic laws when describing adsorption on conductive surfaces.

Even though van der Waals interactions – as expressed in Eq. 1.5 and 1.6 – are purely attractive, a positive energy term appears when the adsorbate gets closer to the surface, because of the increasing overlap between the wavefunctions belonging to the two subsystems. This effect is translated into a short-range Pauli repulsion term, which balances the van der Waals attraction to determine the equilibrium surface/adsorbate distance (l_{ads}) and energy (E_{ads}) for the system (in the case of physisorption, typical values for E_{ads} and l_{ads} are found in the ranges 0.01–0.50 eV and 3–10 Å, respectively).

While physisorption plays an important role in many physical systems, its theoretical modelling is based on methods that often fail to provide satisfactory description of van der Waals interactions. In fact, adsorption of organic molecules on metals surfaces are commonly approached at the *density functional theory* (DFT) level, whose currently most applied exchange-correlation functionals fail to capture the Z^{-1} proportionality of the electron potential outside the metal slab [33,38]. This misrepresentation causes the inadequate description of the long-range van der Waals and image forces, which in turn affects the classical potentials relying on DFT parameterisation. These limitations were successfully overcome in the recent years by the implementation of self-consistent DFT functionals accounting for dispersion interactions (see Chapter 2, Section 2.3.2).

1.2.3 *Chemisorption*

At difference with physical adsorption, chemisorption is characterised by the instauration of definite chemical coordination between the adsorbate and the surface, with important effects on the electronic structure of both. This phenomenon is very important in heterogeneous catalysis, since the formation of chemisorbed intermediates is crucial in the development of reaction pathways. From a kinetic point of view, the first step involved in chemisorption is the trapping of particles at the surface. This requires the inelastic collision between an incoming particle and the surface, in such a way that the dissipation of momentum is sufficient to forbid its elastic reflection in the vacuum, with the particle remaining trapped at the surface potential well (similarly to physisorption). After that, the adsorbed particle can travel on the metal until a preferential chemisorption site is found, where the chemical coordination can take place [31,39].

The chemical bonding is reflected in the higher binding energy (usually ranging from one to few eV per molecule) and in adsorption distances close to the typical value for covalent or ionic coordination (1–3 Å).

As long as significant local variations of the electronic structure are expected to occur, chemisorption is investigated at the level of theory by electron *density of state* analysis (DOS) – in particular the analysis of its local features, *e.g.*, the DOS projected on selected atomic states (pDOS) – and by studying the total electronic charge or the differential charge density distribution (which compares the total density with the one of the subsystems taken separately). The DOS – calculated as the integral of the band structure over the **k**-space (Eq. 1.7) – describes the number of states available to electrons for each energy level, which is useful to characterise the electronic structure of metals in particular. The DOS can be formalised as:

$$\mathrm{DOS}(\varepsilon) = \sum_{n\mathbf{k}} \delta\left(\varepsilon - \varepsilon_{n\mathbf{k}}\right) \ , \tag{1.7}$$

where $\varepsilon_{n\mathbf{k}}$ are the eigenvalues of the Kohn-Sham Hamiltonian (see Chapter 2), with n and **k** being the band and Block vector indexes, respectively. The pDOS is useful for the characterisation of a chemisorbed system, since it is calculated by projecting its total DOS on the atomic orbitals of the non-interacting adsorbate in the gas phase, according to Eq. 1.8 below:

$$\mathrm{pDOS}(\varepsilon) = \sum_{n\mathbf{k}i} \delta\left(\varepsilon - \varepsilon_{n\mathbf{k}}\right) \left| \left\langle \psi_i \middle| \Psi_{n\mathbf{k}} \right\rangle \right|^2 \ , \tag{1.8}$$

where ψ_i are (pseudo) wavefunctions localised onto the molecular atom "*i*" and $\Psi_{n\mathbf{k}}$ the Kohn-Sham eigenstates of the total system. The comparison of the adsorbate pDOS with its total DOS in gas phase can thus assess the effects of the interaction with the surface, which is found to be stronger when significant modifications in the pDOS spectral features are evidenced. Moreover, the same analysis can provide information on the relative position of the frontier molecular orbitals with respect to the Fermi level of the molecule-surface system (since E_F falls within the DOS energy range [33]), which is used to understand if charge transfer from the adsorbate to the metal (or *vice versa*) is expected to occur (see Section 1.3).

Since these modifications/shifts of molecular levels upon adsorption are arising from the creation of new electronic states at the interface, more insights on the chemisorption process can be obtained by studying, *e.g.*, the adsorption of a hydrogen atom approaching a transition metal surface [40]. The frontier orbitals of hydrogen will be the ones playing a role in the interaction process, namely the 1*s* and 2*s* (the highest occupied and the lowest unoccupied, respectively). Initially, the hydrogen atom will interact with the *s*-electrons spilling from the metal surface into the vacuum region, causing the broadening and shift of the atomic orbitals to align the electron chemical potential to the Fermi level of the metal (the shift being usually accompanied to a fractional charge transfer). The broadened peak will present both bonding and anti-bonding character in its lower and higher energy, respectively. For even closer adsorption distance, adsorbate states will start to interact with the more localised d-levels, again splitting in a bonding/anti-bonding pair. The provenience of the electronic charge density included in the bonding states will define the nature of the chemisorption interaction (ionic when either the adsorbate or the metal are solely contributing the shared state charge, or covalent for equally shared contributions).

1.3 Energy level alignment and dipoles at the metal-organic interface

Our brief analysis of the adsorption process highlighted some of the phenomena occurring when molecular and metallic electronic states are close enough to mutually impact each other. In this regard, the metal-organic interface plays a fundamental role in the field of organic electronics, since the performances of devices like *organic light-emitting diodes* (OLEDs), *field effect transistors* (OFETs) or photovoltaic cells, rely on the efficient charge transport through the interface between the two materials [41]. The study of the transport of charge from/to a metallic electrode to/from an organic medium is challenging due to the theoretical limitations in the modelling of this complex problem and the difficulties encountered in getting a univocal experimental picture.

By taking the metal and the organic part separately, the fundamental energy levels in charge transfer processes are rather simply identified by the bare metal work function and the *highest/lowest occupied/unoccupied molecular orbitals* (HOMO/LUMO) of the organic material in gas phase. Anyway, the validity of the Schottky and Mott representation of the metal-semiconductor junction was disproved for the metal-organic one, since the simple vacuum level alignment at the interface was found to apply to a limited number of cases only. Accordingly to this model, the hole and electron injection barriers (ΔI and ΔA, respectively) would remain determined by the difference between the Fermi level of the metal (or its work function) and the ionisation potential (I) or the electronic affinity (A) of the organic molecules, respectively, which gives incorrect values of the charge transfer barriers (Fig. 1.3).

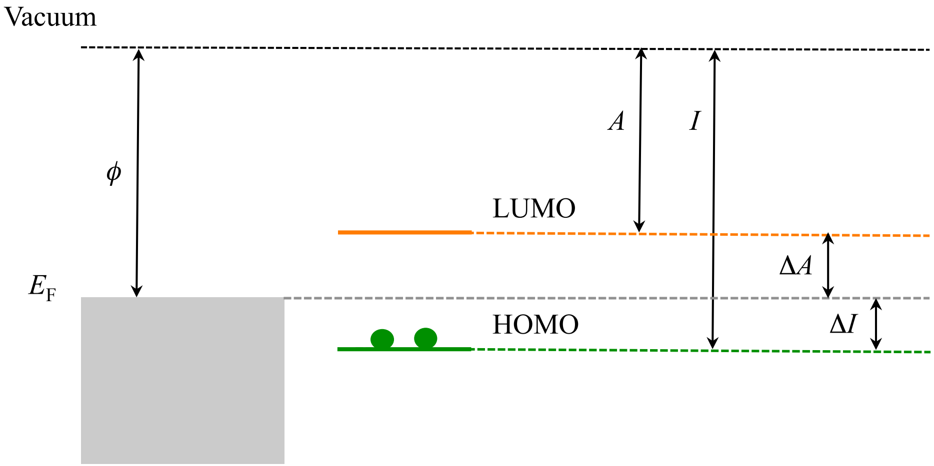

Figure 1.3 Energy diagram for the vacuum level alignment at the metal-organic interface, according to the Schottky and Mott representation of the metal-semiconductor junction.

A better representation is provided by considering the effect of the presence of a dipole layer at the metal-organic contact, which may shift the vacuum level of the metal (and thus its work function, see Eq. 1.3) by as much as 1 eV and induce Fermi level pinning [42-45]. Therefore, the formation of interfacial dipoles has a crucial importance in defining the properties of the electronic junction in organic devices, since the induced vacuum shift may control the energy level alignment and consequently the charge injection/extraction barrier at the metal-organic interface.

We note that a dipole – or its component perpendicular to the surface – with its negative pole directed towards the organic layer (*i.e.*, a *negative* surface dipole) will increase the metal work function as well as the HOMO energy of the organic material, effectively reducing the hole injection barrier. On the other hand, a *positive* surface dipole (positive pole pointing towards the molecular layer) will reduce the work function and the electron injection barrier (Fig. 1.4).

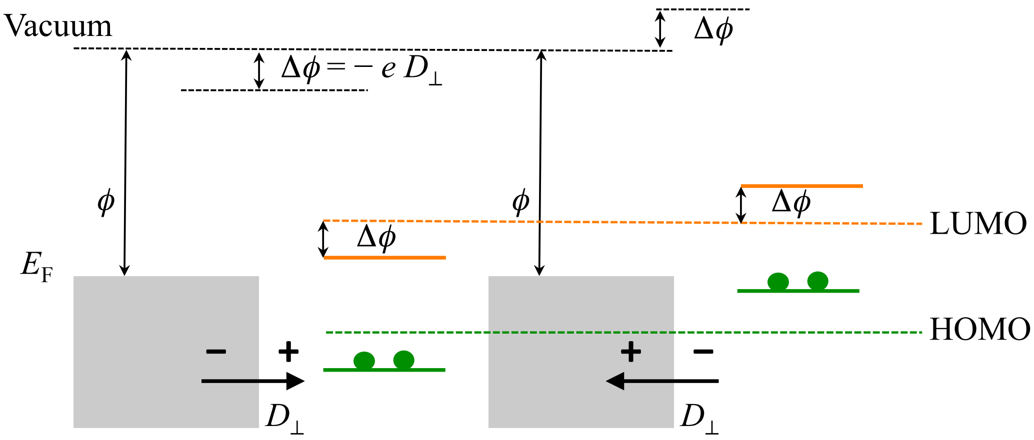

Figure 1.4 Energy level diagram for the metal-organic interface. The formation of dipole layers shifts the vacuum level (*i.e.*, the metal work function) with the effect of modifying the hole and electron injection barrier (see text).

Dipole layers at the metal-organic interface can arise from a variety of processes, including interfacial chemical coordination, formation of interface states, charge transfer, permanent molecular dipoles or even the local compression/displacement of the metal electronic tails upon adsorption of molecules (*pillow effect*) [46,47]. In the absence of covalent metal-organic bonding – as it is the case for a large part of potentially interesting organic optoelectronic devices, the most influential theoretical descriptions of the aforementioned phenomena are the *induced density of interfacial states* (IDIS) [48-50], useful to approach systems with rather strong hybridisation between molecular and metal states, and the *integer charge transfer* models (ICT) [45,51-53], for systems where no or very little hybridisation occurs.

The IDIS model assumes that the originally discrete molecular DOS can be broadened to a continuous distribution upon adsorption, due to the tunneling of surface wavefunction tails into the band-gap of the molecule itself. This effect will cause the presence of some induced DOS at the HOMO-LUMO gap, which may be filled by charge transfer. The energy level alignment at the metal-organic interface is then measured by the position of the metal work function (ϕ) relatively to the so-called molecular *charge neutrality level* (CNL) – calculated by distributing the electronic charge of the neutral molecule in the induced DOS, which determines the size and magnitude of any charge migration. Therefore, the position of the interfacial Fermi level E_F and the value of the surface dipole $\Delta\phi$ can be calculated as a function of a screening parameter S, which measures the dependence of E_F on ϕ (*i.e.*, the degree of Fermi level pinning):

$$E_F - \mathrm{CNL} = S(\phi - \mathrm{CNL}) \qquad [1.9]$$

$$\Delta\phi = (1 - S)(\phi - \mathrm{CNL}) \qquad [1.10]$$

$$S = \mathrm{d}E_F/\mathrm{d}\phi \ , \qquad [1.11]$$

where ϕ is the metal work function. While the screening parameter S ($0 \leq S \leq 1$) is quite sensitive to the molecular adsorption distance, the CNL value is not related to the conformation of the metal-organic interface. In addition, the work function reduction due to the pillow effect (*i.e.*, the orthogonalisation of the metal and molecular wavefunctions) can be accounted within the IDIS framework [50], further improving its predictivity.

At difference to the IDIS description, the ICT model approaches the energy level alignment by assuming that any charge migration at the interface will occur upon formation of discrete states, generated by *integer* charge transfer from electron tunneling. For instance, this representation implies that any surface adsorbed molecule will eventually transforms into a polaron – *i.e.*, a localised state typical in organic conductors – in case of charge transfer. In particular, the ICT model assumes that the Schottky-Mott limit will apply when the metal work function is higher than the formation energy of a negative polaron (*i.e.*, the molecular electronic affinity A) and lower than the formation energy of a positive one (*i.e.*, the molecular ionisation potential I), with no charge migration at the interface (see Fig. 1.3). On the other hand, charge transfer is predicted (with the formation of positive/negative polarons) when the metal work function is lower/higher than the ionisation potential/electronic affinity of the organic material, with Fermi level pinning of the polaronic level.

In case of molecular polarons, the positive and negative charge transfer states will correspond to their HOMO and LUMO levels.

A further term playing an important role in the energy level alignment at the interface is the surface polarisation, which is determined as the Coulomb interaction between the charged state of the adsorbate and its mirror image in the infinitely polarisable metal surface (Fig. 1.5).

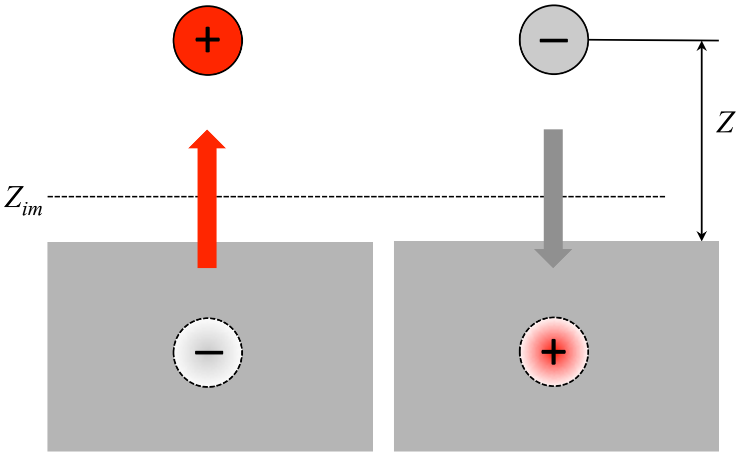

Figure 1.5 Schematic representations of ions adsorbed on a metal surface (grey boxes) according to the image charge model. The screening response of the conductor gives rise to vertical dipoles (represented by arrows).

This interaction will effectively stabilise the charged state by narrowing the molecular HOMO-LUMO gap, similarly to the polarisation of neighbours in organic crystals [54,55]. Remarkably, for weakly physisorbed organic molecules, the screening response is simply related to the image charge potential [56]:

$$U_{im}(Z) = \frac{1}{4|Z - Z_{im}|}, \qquad [1.12]$$

where Z is the distance between the centre of charge of the “polaronic state” (*i.e.*, the added hole/electron) and the substrate. Moreover, the surface screening of charged adsorbates generates strong *standing* dipoles (*i.e.*, perpendicular to the surface plane), whose sign we conventionally set to be positive/negative for positive/negative ions (Fig. 1.5). These *charge transfer dipoles* will significantly shift the work function of the interface – so that the occurrence of charge migration may be detected by spectroscopy techniques. These typically strong dipoles are responsible for the long-range electrostatic repulsion between adsorbates carrying a net charge [26].

1.4 Aims and outline of this work

Herein, we will present a novel approach to understand and control the formation of dipole layers at the metal-organic interface. Our aim is to shed light on the influence of charge transfer on supramolecular self-assembly, which is the origin of the strong, vertical dipoles discussed above. Despite the huge interest in the study of molecular charging and energy level alignment at the metal-organic interface, the formation of low-dimensional supramolecular structure as a consequence of electrostatic repulsion is either poorly understood or its analysis is limited to systems where repulsion arises from irreversible deprotonation [27] or molecular permanent dipoles [57-60].

We will demonstrate that the careful investigation of the relationship between molecular charging and self-assembly behaviour in the sub-monolayer coverage regime can be used to identify functional properties of the metal-organic interface that are important in controlling the contact properties of many devices, with potential application in the field of organic electronics. Our targets are to:

- Characterise how charge transfer effects or surface mediated chemical reactions can influence the formation of strong interfacial electrostatic dipoles, and whether such processes can be predicted by the appropriate selection of molecules, substrates and molecular coverage.
- Obtain new supramolecular aggregates from the competition between long-range electrostatic forces and attractive dispersive interactions.
- Identify if and how the observed self-assembly is related to charge rearrangement effects.

This Thesis will focus on three case studies, in which charge rearrangement at the metal-organic interface is observed in relation to the effect of different phenomena. The study of these systems was addressed by means of DFT calculations (to obtain the accurate description of the interfacial electronic structure), classical molecular dynamics (to resolve the interaction network of extended supramolecular structures), and Monte Carlo lattice gas simulations (useful to extensively sample the configuration pool of two-dimensional growth processes), in close collaboration with experimental group for the chemical synthesis of new molecular units and scanning probe experiments.

The description of the theoretical methods used throughout the Thesis is the object of *Chapter* 2, together with some information on the experimental investigation techniques.

Chapter 3 presents the characterisation of the self-assembly behaviour of a novel *polycyclic aromatic hydrocarbon* (PAH), designed in such a way that its ionisation potential (upon adsorption) is lower than the work function of the Au(111) surface, but higher than the Cu(111) one. Therefore, while the transfer of one electron from the molecule to the Au(111) surface is energetically favoured and indeed occur, charge transfer will not happen on the second substrate where the molecule adsorbs in its neutral state. This has important consequences on the self-assembly phase diagram and suggests a new strategy for the control of the energy level alignment at the metal-organic interface.

In *Chapter* 4 we show how the presence of an electron donor molecule can locally modify the metal work function, inducing charge transfer from the metal to a second molecular species, which would otherwise remain adsorbed in its neutral state. This will be demonstrated by codepositing on Au(111) the same PAH presented in Chapter 3 and a second molecule with acceptor character, but whose electronic affinity alone would not be sufficient to cause charge uptake from the metal.

Chapter 5 will be dedicated to the discussion of the self-assembly of an unprecedented class of organic functionalised borazine molecules adsorbed on

Cu(111). Here the molecular charging will be obtained by following the route of surface mediated chemical reactions. In particular, we will show that electrostatic repulsion arising from the deprotonation of reactive hydroxyl moieties is controlling the size distribution of supramolecular clusters. Our results predict that the molecular structure can be tuned in order to selectively favour specific sizes of the supramolecular aggregates.

Finally, the main outcomes and conclusions of our investigations will be summarised in *Chapter* 6.

Chapter 2

Methods of investigation

This Chapter is entirely devoted to provide a brief introduction to the methods used throughout our work. We will start from the theoretical modelling tools we applied to rationalise the experimental outcomes. In particular, our focus will regard the fundaments of atomistic classical and quantum mechanical simulations, together with stochastic Monte Carlo methods. Because of the central role of experiments in our investigations, some details on scanning probe techniques will also be discussed. Since the vast amount of arguments involved forces us here to a very synthetic presentation, a more complete picture of the methodology can be found in [61,62] (for *ab initio* and classical atomistic simulation methods), [63] (for scanning probe microscopy) and the further references indicated along the Chapter.

2.1 Molecular dynamics

The dynamical behaviour of a system of interacting particles can be simulated by means of a wide class of computational techniques. The idea at the basis of these simulation methods is that the structural and physical characteristics of matter in all its forms can be "calculated", provided that a mathematical model for the selected case is available. In fact, once interactions between particles are described by a suitable Hamiltonian form, all the forces acting in the system are defined. Thereafter, the dynamical evolution of the system can be followed by integrating the appropriate equation of motion over time lengths consistent with the *ergodic hypothesis*, so that the simulated trajectory can be translated into the time average of thermodynamic properties. Thus, molecular dynamics is a useful tool for the calculation of equilibrium properties, but it can also be extended to the characterisation of non-equilibrium processes and to structural optimisation problems.

Our brief discussion of the theoretical modelling of matter starts from the time-independent Schrödinger equation, whose solution provides the complete characterisation of a general many-body system:

$$\hat{H}\Psi(\mathbf{r},\mathbf{R}) = E\Psi(\mathbf{r},\mathbf{R}) \ , \qquad [2.1]$$

Where Ψ is the combined electronic/nuclear wavefunction and $\hat{H}$ is the Hamiltonian energy operator with eigenvalues E. The operator $\hat{H}$ corresponds to the total energy of the system and can be written in the extended form:

$$\hat{H} = \left[\hat{T}_n(\mathbf{R}_I) + \hat{U}_{nn}(\mathbf{R}_I)\right] + \left[\hat{T}_e(\mathbf{r}_i) + \hat{U}_{ee}(\mathbf{r}_i)\right] + \hat{U}_{en}(\mathbf{r}_i,\mathbf{R}_I) \ , \qquad [2.2]$$

where the operator $\hat{T}$ accounts for the kinetic energy and $\hat{U}$ for the potential energy (inter-particles interactions). The subscripts *e*/*i* and *n*/*I* indicates electronic and nuclear terms/particle indices, respectively, of a system counting N electrons and N_n nuclei with positions $\mathbf{r}_i$ and $\mathbf{R}_I$.

Unless dealing with very simple problems, the direct solution of the Schrödinger equation is not viable because of its excessive computational cost. The huge complexity of the many-body problem calls for the introduction of simplifications, among which the first important example is provided by the Born-Oppenheimer *adiabatic approximation*. This approach exploits the large mass difference between nuclei and electrons with the aim of decoupling their dynamics. In particular, it is assumed that the mass of electrons is so small that they can adapt in negligible time to the eventual displacement of nuclear positions, with no effect on their energy state. This assumption allows treating the electrons ($\tilde{\Psi}$) and the nuclei (Φ) as two separate contributions to the global wave function (*quasi-separable ansatz*, Eq. 2.3), with the electronic term parametrically depending on the nuclear positions:

$$\Psi(\mathbf{r},\mathbf{R}) = \tilde{\Psi}(\mathbf{r};\mathbf{R})\Phi(\mathbf{R}) . \qquad [2.3]$$

Hence, Eq. 2.1 can be divided into two parts, the first of which describes the motion of electrons around fixed nuclear positions (Eq. 2.4):

$$\hat{H}\tilde{\Psi}(\mathbf{r};\mathbf{R}) = \varepsilon_0(\mathbf{R})\tilde{\Psi}(\mathbf{r};\mathbf{R}) . \qquad [2.4]$$

The solution of Eq. 2.4 gives the ground state energy ε_0 (*i.e.*, the adiabatic contribution of electrons to the total energy), while the nuclei can be treated as classical objects moving on the ground state surface $E_0(\mathbf{R}) = \varepsilon_0(\mathbf{R})+\hat{U}_{nn}(\mathbf{R})$, so that their dynamics can be followed by solving the Newton's equation:

$$m_I\ddot{\mathbf{R}} = -\nabla_I \; E_0(\mathbf{R}) , \qquad [2.5]$$

where m_I is the nuclear mass. The potential gradient, in Eq. 2.5, returns the force acting on all the atoms in the system (which sums the internuclear repulsion and the derivative of the electronic eigenvalues), so that its evolution can be tracked down starting from an initial time t, with known positions and velocities. Thus, Eq. 2.5 can be numerically solved by means of time discretisation, which is implemented by choosing an integration step Δt sufficiently long to sample the trajectory for meaningful time lengths, but small enough to minimise discretisation errors. Therefore, the atomic coordinates and velocities at (t +Δt) are usually calculated by means of fast and stable integration methods, among which the Verlet algorithm is the most applied [64]. Having chosen the discretisation step Δt, this method takes the sum of the Taylor series expansions for the atomic positions immediately before and after a generic time t, to calculate the positions at (t +Δt):

$$\mathbf{R}(t+\Delta t) = \mathbf{R}(t) + v(t)\Delta t + \frac{a(t)}{2}\Delta t^2 + O(\Delta t^4)$$

$$\mathbf{R}(t-\Delta t)=\mathbf{R}(t)-v(t)\Delta t+\frac{a(t)}{2}\Delta t^2+O(\Delta t^4)$$

$$\mathbf{R}(t+\Delta t)=2\mathbf{R}(t)-\mathbf{R}(t-\Delta t)+a(t)\ \Delta t^2+O(\Delta t^4)\ , \qquad [2.6]$$

where v and a are the velocity and the acceleration, respectively.

However, the derivation above – that is valid within the Born-Oppenheimer description – still requires at least a reasonable expression for the potential $E_0(\mathbf{R})$. This could be made available from the explicit solution of the electronic Schrödinger equation (Eq. 2.4), which usually requires further approximations (see Section 2.3). An alternative and very popular route is represented by classical molecular dynamics, where the real potential is replaced with an empirical or semi-empirical one, whose formulation – included in the framework of classical mechanics – is meant to imitate the effects of $E_0(\mathbf{R})$.

2.2 Classical molecular dynamics

Classical molecular dynamics is a simulation technique that aims to mimic the electronic contributions by means of a classical potential, commonly referred to as *force field*. The key requisite for this class of force fields is the accurate representation of the real potential for a large variety of systems, *i.e.*, a challenging combination of accuracy and transferability.

The mathematical formulation of a generic force field distinguishes between *bonded* (atomic bonds and bonding angles) and *non-bonded* potential terms (expressing electrostatic and dispersion interactions) (Eq. 2.7). Bonded contributions to the system's energy are calculated using harmonic terms, where the equilibrium values of bond lengths and angles are inferred either from quantum mechanical calculations or experiments. Likewise, non-bonded interactions are usually described via Coulomb and Lennard-Jones potentials, which require specific parameterisation to model the electrostatic contributions associated to each atomic position (*i.e.*, partial atomic charges) and the van der Waals forces. In particular, partial charges and are usually extrapolated from the electrostatic potential calculated at the quantum mechanical level – to reflect the charge distribution of the system, while the van der Waals parameters can be extracted either from theory or experiments. The typical mathematic formulation of a classical force field is the following [65]:

$$\begin{aligned} H = & \sum_{BONDS} K_r\left(r - r_{eq}\right)^2 + \sum_{BONDS} K_\theta\left(\theta - \theta_{eq}\right)^2 + \\ & + \sum_{TORSION} \frac{V_n}{2}\left(1 + \cos\left(n\alpha - \gamma\right)\right) + \\ & + \sum_{i<j}\left[\frac{A_{ij}}{R_{ij}^{12}} + \frac{B_{ij}}{R_{ij}^{6}} + \frac{q_i q_j}{R_{ij}}\right] \end{aligned} , \qquad [2.7]$$

where the first two sums are harmonic potentials modelling the stretching and bending of interatomic bonds, while the third one represents the torsional potential involved in the relative rotations within quartets of bonded atoms. The last sum accounts for the non-bonded van der Waals and electrostatic contributions, where the first are described by a 12-6 Lennard-Jones potential and the latter by the elementary Coulomb potential between partial atomic charges. To limit the computational cost associated to the calculation of short and long-range interactions, a cutoff distance is chosen to define a finite volume beyond which the contribution of the potential is neglected. Electrostatic interactions are usually treated with Ewald summation techniques in the Fourier-space [66], to achieve convergence with improved efficiency.

Although representing a useful tool for the modelling of large systems and to give access to time scales necessary for the investigation of their structural evolution [67], classical molecular dynamics suffers from several limitations, inherently related to the neglection of electronic effects. In fact, systems where chemical interactions occur cannot be addressed at this level of theory and even physical phenomena related to local fluctuations of charge density – such as polarisation screening – cannot be reproduced. Although new types of polarisable and reactive force field were made available in the recent years [68-70], their diffusion is inhibited by the huge difficulty in recovering the parameterisation required for the meaningful and reliable representation of systems where several interatomic interactions are involved. Anyway, classical potentials are still very important for the study of problems where complex electronic effects play a negligible role.

2.3 Density functional theory

The many-body wavefunction describing a group of interacting electrons – as given by the direct solution of the Schrödinger equation – is out of reach except for the most trivial systems. Therefore, the numerical solution of the electronic eigenvalue problem (Eq. 2.2) requires the introduction of approximations intended to preserve as much as possible the accuracy of the results, while significantly reducing the computational effort. Among these approaches, one of the first and most notable is the Hartree-Fock method, which was introduced shortly after Schrödinger's formulation. This method – based on the *antisymmetric product ansatz* – is still in use, but it finds little application due to the large computational cost for a still substantially approximated solution. A more convenient way for approaching the solution of the Schrödinger equation was provided with the introduction of *density functional theory* (DFT), which constituted a major breakthrough in the field of theoretical material science, as it allowed mapping a many-body system onto a single-particle one. The relatively moderate computational cost, together with the continuous improvements in the representation of electronic exchange-correlation contributions to the total energy and other physically important effects, contributed to make DFT the most successful quantum mechanical computational tool.

The basis of the DFT method was set in 1964 by the work of Hohenberg and Kohn [71], in which it was demonstrated that the electronic charge density is the central variable in treating the electronic problem. In particular, Hohenberg and Kohn pointed out that (*i*) the total energy – and the external potential u – are uniquely determined by the electronic density $\rho(\mathbf{r})$ (Eq. 2.8) and that (*ii*) the density obtained by minimising the total energy is the ground state. The energy of the system is thus defined as a functional of $\rho(\mathbf{r})$ (Eq. 2.8):

$$E\left[\rho(\mathbf{r})\right]=\int u(\mathbf{r})\rho(\mathbf{r})\mathrm{d}\mathbf{r}+F_{HK}\left[\rho(\mathbf{r})\right] , \qquad [2.8]$$

where F_{HK} is an universal functional of the electronic density (accounting for the kinetic and electron-electron interaction energies). The solution of the Schrödinger equation is then obtained by simply minimising the energy functional $E[\rho]$ with respect to the electron density:

$$E_0\left[\rho(\mathbf{r})\right]=\min_{\rho}\left\{E\left[\rho(\mathbf{r})\right]\right\}=\min_{\rho}\left\{U\left[\rho(\mathbf{r})\right]+F_{HK}\left[\rho(\mathbf{r})\right]\right\} , \qquad [2.9]$$

where the only part missing is a practical analytic expression for the functional F_{HK}. This issue was addressed by Kohn and Sham [72], whose approach consisted of approximating the kinetic and Hartree electrostatic contributions – the latter being defined as the potential arising from the electronic charge distribution – with those of a fictitious system of non-interacting electrons moving in the same external potential (Eq. 2.10 and 2.11, respectively):

$$T_s[\rho]=-\frac{1}{2}\sum_{i}^{N}\langle\psi_i|\nabla^2|\psi_i\rangle , \qquad [2.10]$$

$$E_H[\rho]=\frac{1}{2}\iint \mathrm{d}^3\mathbf{r}\ \mathrm{d}^3\mathbf{r}'\frac{\rho(\mathbf{r})\rho(\mathbf{r}')}{|\mathbf{r}-\mathbf{r}'|} . \qquad [2.11]$$

In this way, a system of N non-interacting electrons can be tracked down to the single-particle scheme and described by a single determinant wavefunction in N orbitals ψ_i (with charge density defined as $\rho(\mathbf{r}) = \Sigma_i |\psi_i|^2$).

When moving back to a system of mutually interacting electrons, the additional energy contributions can be "stored" in the *exchange-correlation functional*:

$$E_{xc}[\rho]=F_{HK}[\rho]-T_s[\rho]-E_H[\rho] . \qquad [2.12]$$

Hence, the total energy expression can be updated to include the exchange-correlation term (Eq. 2.13):

$$E_0\left[\rho\right]=\min_{\rho}\left\{T_s\left[\rho\right]+U\left[\rho\right]+E_H\left[\rho\right]+E_{xc}\left[\rho\right]\right\}, \qquad [2.13]$$

from which the Kohn-Sham functional V_{KS} is defined as the sum of the last three terms on the left:

$$V_{KS}\left[\rho\right]=U\left[\rho\right]+E_H\left[\rho\right]+E_{xc}\left[\rho\right] \ . \qquad [2.14]$$

For a system of non-interacting electrons, the same minimum condition expressed in Eq. 2.13 is valid for the Kohn-Sham potential, which reads:

$$v_{KS}(\mathbf{r})=u(\mathbf{r})+\int \mathrm{d}^3\mathbf{r}'\frac{\rho(\mathbf{r}')}{\left|\mathbf{r}-\mathbf{r}'\right|}+\frac{\delta E_{xc}\left[\rho(\mathbf{r})\right]}{\delta\rho(\mathbf{r})} \ . \qquad [2.15]$$

Finally, the ground state charge density of the interacting many-electron system in an external potential – originally described by a many-electron Schrödinger equation – can be calculated by solving a set of non-interacting single-particle problems in the fictive potential v_{KS} (Kohn-Sham equations):

$$\left[-\frac{1}{2}\nabla^2+v_{KS}(\mathbf{r})\right]\psi_i(\mathbf{r})=\varepsilon_i\psi_i(\mathbf{r}) \ , \qquad [2.16]$$

where ψ_i are the so-called Kohn-Sham orbitals. The solution of this nonlinear problem is carried out via self-consistent iterative methods, provided that an expression for the exchange-correlation potential is available.

2.3.1 *Local exchange-correlation functionals*

The DFT formalism, presented in the previous Section, is strictly exact within the Born-Oppenheimer approximation. However, in order to solve the Kohn-Sham equations, the many-body effects left aside in the exchange-correlation potential require to be properly represented. In this regard, the exchange interactions are directly related to the antisymmetry of the many-body wavefunction – *i.e.*, to the Pauli exclusion principle, which is exactly represented in the Hartree-Fock method (leading to development of hybrid DFT/Hartree-Fock functionals). The treatment of the correlation energy is way more challenging, since it is equal to the difference between the real and the Hartree-Fock energy of the system. This contribution cannot be directly calculated, but a good description is provided by Quantum Monte Carlo calculations.

However, the exchange-correlation term is quite successfully estimated with the *local density approximation* (LDA), where it is assumed to be equal to that of a homogeneous electron gas and to depend only on the local density as:

$$E_{xc}^{LDA}\left[\rho(\mathbf{r})\right]=\int \varepsilon_{xc}^{\mathrm{hom}}\left(\rho(\mathbf{r})\right)\,\rho(\mathbf{r})\;\mathrm{d}^3\mathbf{r}\;. \qquad [2.17]$$

The popularity of the LDA functional is generally attributed to its systematic cancellation of errors, arising from the overestimation of the exchange energy. This effect is responsible for the successful application of LDA to a range of systems much wider than the simple metals and intrinsic semiconductors classes, which were originally proposed in view of their smooth charge density. However, even though LDA is proven to give good result for condensed matter, its description of molecular systems is much less accurate, leading to an overestimations of bond lengths and energies of the 20% in average.

The LDA approach to the calculation of the exchange-correlation energy was extended by taking into account the local gradient of the charge density, which is referred to as *generalised gradient approximation* (GGA):

$$E_{xc}^{GGA}\left[\rho(\mathbf{r})\right]=\int \varepsilon_{xc}\left(\rho(\mathbf{r}),\nabla\rho(\mathbf{r})\right)\,\rho(\mathbf{r})\;\mathrm{d}^3\mathbf{r}\;. \qquad [2.18]$$

The GGA functional guarantees a better representation of binding energies, for a moderate increase of the computational cost. In addition, GGA yields improved results for the modelling of strong intermolecular interactions such as hydrogen bonds or chemisorption at the metal-organic interface, whose effect would be badly overestimated by LDA.

2.3.2 *Non local exchange-correlation functionals*

When dealing with sparse systems, the interparticle distances are typically so large that *non local* (dispersion) forces need to be considered. This is the case of van der Waals complexes, soft matter or – as it is relevant for our study –

organic molecules physisorbed on metal surfaces. Simulating adsorption is challenging within the aforementioned *local* (LDA) and *semilocal* (GGA) density functionals. In fact, while GGA yields satisfactory representation of chemisorption, the weaker physisorption binding is usually misrepresented to the point of being totally omitted. On the other hand, LDA was found to give better results just because of its known overbinding, which somehow mimics the van der Waals long-range interactions. For these reasons, GGA/LDA results are usually regarded as a lower/upper limits for van der Waals binding energies, and the combination of the two can give a more coherent picture for the properties a sparse system [73].

The reason for the failure of local or semi-local functionals in representing long-range dispersion forces is to be found in their intrinsic mean-field approach, which treats the charge as a localised entity and in turn cuts any long-range tail. However, when two atoms (*A* and *B*) are separated in such a way that their respective wavefunctions are not overlapping, their polarisabilities (α_A and α_B) generate induced dipole interactions calculated as:

$$E^{nl} = \frac{-C_6^{AB}}{R^6} \ , \qquad [2.19]$$

where C_6 (known as the Hamaker constant) is a parameter accounting for the dispersion interactions strength for the *AB* couple (E^{nl}), neglecting both the influence of the medium and quantum perturbations. The constant C_6 is calculated as:

$$C_6^{AB} = K\hbar\omega_0\alpha_A\alpha_B \ , \qquad [2.20]$$

where K is a dimensionless factor and ω_0 the frequency of the harmonic oscillator. Even if very simple, the potential in Eq. 2.19 captures the $1/R^6$ dependence of van der Waals interactions determined by a dipolar field. These effects were accurately reproduced at the *ab initio* level by using second-order Møller-Plesset perturbation theory (MP2 method), which is however too computationally demanding to find wide application.

In recent years, non local contributions have been explicitly included in *van der Waals density functionals*, based on implementation schemes relying on efficient fast Fourier transform algorithms [74,75]. These approaches express the non local correlations in terms of density-density interactions – fully defined by the local charge density and its gradient.

2.3.3 *Limitations of density functional theory*

Even though DFT is successfully applied in the characterisation of many physical systems, its current development is still affected by major shortcomings [76]. First of all, the interactions between electrons and their own field should cancel, which is not the case within the actual approximations. This flaw is known as the *self-interaction error* [77], which is particularly important in the presence of localised electrons and for truncated geometries.

A second issue is evidenced for systems containing both atomic-like (*d* or *f* electrons) and delocalised states (usually associated to *s* and *p* electrons), where the filling of the localised *d*/*f* states increases their energy – due to the high electron-electron Coulomb repulsion – and may affect the validity of the Kohn-Sham way of filling electronic orbitals.

Ultimately, the bandgap of solids is usually strongly under/overestimated since DFT is a ground state theory, where the Kohn-Sham eigenvectors and eigenvalues are mathematical quantities with no physical meaning.

2.3.4 *Plane waves in the reciprocal lattice*

In accord with the Bloch' theorem (Eq. 2.21), the Kohn-Sham wavefunctions for periodic systems can be treated as the product between an exponential term (plane wave) and a periodic Bloch function (with periodicity equal to that of the system's potential, Eq. 2.22):

$$\psi_{n,\mathbf{k}}(\mathbf{r}) = e^{i\mathbf{k}\cdot\mathbf{r}}\, f_{n,\mathbf{k}}(\mathbf{r}) \qquad [2.21]$$

$$f_{n,\mathbf{k}}(\mathbf{r}+\mathbf{R}) = f_{n,\mathbf{k}}(\mathbf{r}) \ , \tag{2.22}$$

where **R** is the lattice vector of the periodic system and **k** is a vector in the reciprocal lattice. Each Bloch state $\psi_{n\mathbf{k}}$ corresponds to an energy eigenstate $\varepsilon_n(\mathbf{k}) = \varepsilon_n(\mathbf{k} + \mathbf{K})$ (**K** being the **k**-space periodicity), where the eigenstate ε_n is a continuous function of **k**, which identifies the n^{th} band. Therefore, each energy band n presents the same periodicity of the **k**-space and is uniquely defined by the set of **k**-vectors included in the first Brillouin zone.

The periodic functions f can be expanded as Fourier series:

$$f_{n,\mathbf{k}}(\mathbf{r}) = \sum_{\mathbf{G}} c_{n,\mathbf{G}} \ e^{i\mathbf{G}\cdot\mathbf{r}} \ , \tag{2.23}$$

where **G** are vectors in the reciprocal space, satisfying the condition $\mathbf{G}\cdot\mathbf{R} = 2\pi m$ (m an integer), and c are the expansion coefficients. Hence, the linear combination of plane waves gives the electronic wavefunctions:

$$\psi_{n,\mathbf{k}}(\mathbf{r}) = \sum_{\mathbf{G}} c_{n,(\mathbf{k}+\mathbf{G})} \ e^{i(\mathbf{k}+\mathbf{G})\cdot\mathbf{r}} \ . \tag{2.24}$$

The potentially infinite plane waves basis set is in practice reduced to include only those with kinetic energy lower than a threshold (*cutoff energy*), which has to be anyway sufficient to guarantee the convergence of the total energy. In addition, as long as the electron wavefunctions is similar for **k**-vectors that are close, the wavefunctions over an entire region of the **k**-space can be represented by the wavefunction at a selected point. This allows one to limit the number of **k**-points used for the orbitals expansion, provided that the sampling is sufficient to assure the convergence of the total energy. The advantages of the plane wave formalism are directly connected to its inherent non-locality, together with the diagonal character of the gradient operator in the reciprocal space, which greatly simplifies the computation.

Importantly, the periodicity can be exploited also for non-continuous systems (such as molecules or surfaces), with the only requirement that the supercell dimensions are sufficient to avoid interactions between periodic replicas.

2.3.5 *Core states and pseudopotentials*

The computational cost associated with the plane wave approach is connected to the magnitude of the energy cutoff, which should ideally be as small as possible in order to limit the number of basis functions to be handled. However, in proximity of nuclear positions, the valence orbitals are bound to strongly oscillate to fulfil the orthogonality condition with the core states, which would require setting a very high value of energy cutoff in order to include plane waves with short wavelength (*i.e.*, increasing the size of the basis set and consequently the time required to have converged results).

This issue is usually circumvented with the implicit description of core electrons, *i.e.*, by replacing them with an effective potential (*pseudopotential*) mimicking the core states. The pseudopotential approach finds support from two simple considerations, namely: (*i*) low energy core electrons are highly localised and are not expected to play a significant role in the “chemistry” of the system of interest, (*ii*) valence orbitals are rapidly varying only in correspondence of nuclear positions, their shape being much smoother elsewhere. Obviously, such a fictitious potential will have to match the important requirements of (*i*) reproducing the same valence spectrum as the real potential, (*ii*) define a “core radius” outside which the pseudo wavefunctions are reproducing the all-electron ones and (*iii*) being transferable.

The general representation of pseudopotential in the *bra ket* notation is the following (Eq. 2.25):

$$V_{ION} = \sum_{lm} |lm\rangle V_l \langle lm| \ , \qquad [2.25]$$

where $\langle lm|$ are spherical harmonics and V_l are components of the pseudopotential acting on the respective wavefunction components (with angular momentum l). Pseudopotentials are known in either their *local* formulation (where V_l is taken to be the same for each l), or in their *non local* Kleinman-Bylander one [78] (which is required to obtain accurate results). In particular, *norm-conserving* pseudopotentials are constructed in such a way that the norm of the pseudo wavefunction has the same value of the all-electron one inside the core radius. This condition is relaxed in *ultrasoft* pseudopotentials, which have found wide application as they further reduce the size of the basis set (*i.e.*, the energy cutoff) by partitioning the valence charge in different contributions [79]. The application of the pseudopotential method to describe core states brings the advantages of effectively reducing the total number of electrons to be treated explicitly and the energy cutoff, due to the smoother oscillations around atomic cores.

2.3.6 *Total energy minimisation*

For a group of fixed nuclear position, the solution of the Kohn-Sham equations set is traditionally performed by a self-consistent loop, *i.e.*, the Kohn-Sham eigenvalues – calculated for a guess charge density $\rho(\mathbf{r})$ – are in turn used to calculate an updated charge density with matrix diagonalisation algorithms, this loop being performed until self-consistency is reached.

When the electronic states of a system are fully defined by the procedure above, the forces acting on each atomic position can be calculated using the Hellmann-Feynman theorem:

$$F_I = -\frac{\partial E}{\partial \mathbf{R}_I} = -\sum_i \langle \psi_i | \frac{\partial \hat{H}}{\partial \mathbf{R}_I} | \psi_i \rangle \ , \qquad [2.26]$$

where F_I is the force acting on the I-ion with position $\mathbf{R}_I$. Once the forces acting on all the atoms are known, the Newton's equation of motion can be integrated to follow the dynamic of the systems. This knowledge can be also easily translated into geometry optimisation procedures, noting that the global force has to be (at least nearly) null at the equilibrium, so that (Eq. 2.27):

$$F_I = -\frac{\partial E}{\partial \mathbf{R}_I} = 0 \ . \qquad [2.27]$$

This geometry optimisation problem in multi-dimensional space is usually tackled by means of Quasi-Newton-Raphson methods.

2.4 Monte Carlo simulations of lattice gas models

The two-dimensional Ising magnet is a flexible tool that can be easily adapted to the modelling of liquid-gas phase transitions or, more generally, of the two-dimensional aggregation of generic particles [80]. In fact, the Ising lattice of spin can be thought of as a grid of cells, which can be either empty ($\sigma = 0$) or occupied by a particle ($\sigma = 1$). The value of σ is then the cell occupation number and it is defined by the following change of variable:

$$s_i = 2\sigma_i - 1 \ , \qquad [2.28]$$

where $s = \pm 1$ is the magnetic spin and the subscript i indicates the lattice position index. Eq. 2.28 immediately shows that the “spin up” state translates into an occupied lattice cell ($s = +1 \rightarrow \sigma = 1$), while the “spin down” remains associated to an empty position ($s = -1 \rightarrow \sigma = 0$). The parallel between the magnetic and the *particle lattice* can be further extended to the Ising Hamiltonian, as the coupling constant J of the magnet can be directly translated into the van der Waals attraction between neighbouring particles, whereas the eventual action of a magnetic field would define the chemical potential μ. Hence, in analogy with the Ising model, the grand canonical partition function for the isomorphic *particle lattice* can be written as:

$$\Xi = \sum_{\nu} \exp\left[\frac{1}{kT}\left(\mu\sum_{i=1}^{N}\sigma_i + J\sum_{\langle i.j\rangle}\sigma_i\sigma_j\right)\right] \ . \qquad [2.29]$$

The external sum in Eq. 2.29 is extended over all the system’s microstates ν, while, in the exponential term, the first sum is made over all the N lattice positions i and the latter over the nearest neighbours couples $\langle i, j\rangle$. A system with such a partition function is commonly referred to as *lattice gas*, whose implementation can be prepared to include more states per lattice position (*e.g.*, multicomponent case), different potential terms or even more complicated morphologies (for relevant examples see [81,82]).

The typical system we aim to investigate here is one were mutually interacting molecules are constrained (*i.e.*, adsorbed) onto a two-dimensional plane, where they are freely hopping between degenerate adsorption positions. It is then clear that Monte Carlo simulations of the two-dimensional lattice gas model represent the ideal tool to study the configurational evolution of such systems, provided that a suitable parameterisation of the intermolecular interactions is available. The Hamiltonian is usually made available from calculations at the atomistic level of the molecule-molecule attraction (*e.g.*, using classical force fields or DFT modelling), while electrostatic interactions – if necessary – can be parameterised on the basis of the image charge screening model, together with the geometrical information obtained from DFT structural-optimisation.

Once the Hamiltonian for the system is defined, its equilibrium is searched by means of the statistical sampling of the configurational space (so that the probability of falling in a specific configuration is proportional to the Boltzmann one), instead of following the route of molecular dynamics. More specifically – restricting our analysis to the case of the (N,V,T) canonical ensemble, one can start from a randomly generated configuration "o" with known energy $U(o)$, and generate a new configuration by, say, exchanging the position of two particles to give a new configuration "n" with energy $U(n)$. The swap can be then tested accordingly to the Metropolis scheme [83] by, *e.g.*, accepting it if the energy difference associated with the swap is negative ($[U(n) - U(o)] < 0$) or accepting it with probability $a = exp\{-[U(n)-U(o)]/kT\}$ otherwise.

The further screening of the move for the condition $[U(n) - U(o)] > 0$ is performed by generating a random number r $(0 \leq r \leq 1)$ and refusing the configuration swap only if $exp\{-[U(n) - U(o)]/kT\} < r$. Therefore, the direct consequence of the Metropolis method is that – at finite temperature – there is always a non-null probability for accepting a configurational change, even when it is associated to an increase in the total energy of the system. This is useful to avoid the system's evolution to get trapped in local minima, but at the same time it may require an extensive sampling in order to reach the actual equilibrium. The convergence is usually helped using the method of *simulated annealing*, which involves the controlled cooling of the system (*i.e.*, a gradual reduction of the probability of accepting energetically unfavourable Monte Carlo moves).

2.5 Scanning tunneling microscopy

Scanning tunneling microscopy (STM) is a technique based on the quantum mechanical electron tunneling effect, which allows the imaging of surfaces with atomic resolution. With this method, introduced by Binning and Roherer in 1981 [84,85], the atomic imaging is obtained with lateral resolution of ~1 Å by taking an ideally atomic sharp tip to a distance of 10 Å or less from the surface of the sample. A small current is then generated and measured (~ 1 nA) by applying a bias voltage sufficient to trigger the tunneling of electrons through the vacuum region separating the tip and the sample. The actual intensity of the current is related to the tunneling transition probability, whose exponential dependence on the tip-sample distance increases the resolution of vertical displacements up to tenths of Å. Piezoelectric devices guarantee the precise control of the tip position, while either the current or the tip height can be kept fixed to give *constant current* or *constant height* topographic maps, respectively.

In the limit of zero temperature and small bias voltage, Tersoff and Hamann [86] showed that the tunneling current I is proportional to the local density of state of the sample (N_s) at E_F, in correspondence to the tip position $(I \propto N_s(\mathbf{r}_0, E_\mathrm{F}))$, where N_s is calculated as (Eq. 2.30):

$$N_s(\mathbf{r}_0, E_\mathrm{F}) = \sum_\nu |\Psi_\nu(\mathbf{r}_0)|^2 \delta(E_\nu - E_\mathrm{F}) \ , \qquad [2.30]$$

where the sum is made over surface states ν, giving essentially the charge density of states at Fermi.

The sign of the applied bias voltage is important because it defines the direction of the tunneling current flux. In particular, at positive bias (*i.e.*, the tip being the negative pole) electrons are flowing from occupied tip states to unoccupied sample ones, while at negative bias (*i.e.*, the sample being the negative pole) electrons are flowing from occupied sample states to the tip. Consequently, measures at positive/negative bias will map the density of states of LUMO/HOMO levels, provided that STM images are not iso-N_s surfaces but rather the sum of N_s in the interval comprised between E_F and $E_\mathrm{F} + eV$, where V is the applied bias. Since the features observed in STM images are a mixture between geometrical and electronic effects, theoretical modelling is often required to support the interpretation of the experimental results.

2.6 Scanning tunneling spectroscopy

Since the STM method allows for the local probing of the density of electron states, its application was readily extended to perform local spectroscopy measurements. The chance of applying the same STM technology to gather information about the local density of states was evidenced in the early works of Binning and Rohrer, who noticed changes in the atomic imaging when varying the applied tip/sample bias.

Scanning tunneling spectroscopy (STS) uses the same STM apparatus to record N_s as a function of the electrons energy (*i.e.*, the tip/sample bias). This is routinely performed by placing the tip in a selected position, at fixed height, and then measuring the tunneling current by moving the bias in a defined range of energies. The recorded I-V curve is the STS spectrum and its derivative dI/dV is proportional to the local density of states, even though the direct proportionality between I and N_s, shown in Eq. 2.30, is only valid in the limit of small bias. Within this limit, the current can be expressed (using the Wentzel-Kramers-Brillouin approximation) as a convolution of the tip and sample density of states (N_t and N_s, respectively) (Eq. 2.31):

$$I(V) \propto \int_0^{eV} N_s(E)\, N_t(E-eV)\, T(E,eV,Z)\; \mathrm{d}E \ , \qquad [2.31]$$

where the integration is made over all the states contributing to the tunneling current (zero corresponds to the Fermi level) and T is the tunneling transition probability. Assuming constant tip density of states, the derivative of Eq. 2.31 reduce to the form:

$$\frac{\mathrm{d}I(V)}{\mathrm{d}V} \approx N_s(0)\, N_t(eV)\, T(E,eV,Z) \ . \qquad [2.32]$$

The equation above shows the relationship between dI/dV and N_s, which defines the local STS spectra.

Similarly, STS can be performed at constant V, by measuring the response of the current to the variation of the tip/sample distance Z. This type of spectroscopy is used to measure the work function of the surface, since its value is related to the differential conductivity dI/dZ from the relation:

$$\phi \approx 0.95\left(\frac{\mathrm{d}\ln(I)}{\mathrm{d}Z}\right)^2 , \qquad [2.33]$$

which is valid in the small bias limit and for tip/sample distances >5 Å. Recently, the introduction of tip height modulation techniques allowed the simultaneous acquisition of constant current STM and dI/dZ STS maps. This approach sums a high frequency modulated voltage to the actual tip/sample bias, which in turn generates a small sinusoidal displacement of Z (typically of few tenths of an Å). This small oscillation is accompanied by an alternating current response, whose component in-phase with the modulation gives directly the dI/dZ spectra and, thus, the work function [63].

Chapter 3

Reversible charge transfer upon energy level alignment: Pyrene derivative on Cu(111) and Au(111)

The deposition of thin molecular layers onto metallic electrodes represents the first step in the fabrication process of devices such as organic solar cells. In these applications, the efficiency of charge injection and transport is dependent on both the electronic properties of the interface and the structure of the molecular layers. The initial arrangement of the molecules in the growing film is particularly crucial to set the device performance, since it determines the energy level alignment at the interface and the efficiency of the charge transport through the molecular medium.

Within this framework, the electronic properties of *polycyclic aromatic hydrocarbons* (PAHs) place them among the best candidates for the development of "green", cost-effective technologies and of optoelectronic devices in particular. In fact, PAHs are suitable electron donor molecules thanks to their ionisation potential being close to the Fermi energy of several transition metals [87-89].

The work presented in this Chapter is the result of a novel approach that aims to obtain some degree of control in the experimental construction of supramolecular self-assembled systems through the theoretical understanding of the charge injection processes at the metal-PAH interface. We will present the characterisation of the self-assembly behaviour of a novel pyrene derivative (tetra[1,3-di(*tert*-butyl)-phenyl]-pyrene (TBP)) upon deposition on the Cu(111) and Au(111) surfaces. Our approach will combine scanning tunneling microscopy/spectroscopy and theoretical modelling, to obtain a comprehensive description of the metal-organic interface.

The *ad hoc* molecular functionalisation permits the fine tuning of the gas phase ionisation potential, in such a way to trigger charge transfer from the molecule to the noble Au(111) surface only. Moreover, the interplay between intermolecular electrostatic repulsion arising from charge transfer and van der Waals attraction generates a complex self-assembly phase diagram, which we attribute to an *anomalous coarsening* process, related to the non-trivial energy level alignment at the interface. The observed organisation behaviour reveals the possibility of controlling molecular self-assembly beyond the nearest neighbour scale by means of long-range electrostatic interactions, which can be useful for the integration of bottom up and top down nanofabrication techniques.

This work results from the synergic collaboration with Daphne Stassen, Prof Davide Bonifazi (chemical synthesis of the molecule, Université de Namur), Ada Della Pia and Prof Giovanni Costantini (STM/STS characterization of the metal-organic system, University of Warwick) and Dr Andrea Floris (*ab initio* theoretical modelling, King's College London). Part of the study presented here has been recently edited and submitted for publication [90].

3.1 Charge transfer dipoles and long-range ordering

It is well established that short-range attractive interactions are the dominant driving force for the organisation of molecules on atomically flat metal surfaces with smooth potential adsorption energy profile. Indeed, they dictate the formation of extended structures whose regularity is a function of the strength and directionality of the intermolecular forces [17]. On the other hand, the effect of long-range interactions between charged molecules is much less understood and calls for further in-depth analysis. In this direction, ordering on length scales larger than the nearest neighbour was recently obtained via electrostatic intermolecular interactions, achieved by depositing either strong [91] or weak molecular donors [26] on metal surfaces. It was observed that molecules with strong donor character do not show any self-assembly, but rather organise as isolated monomers, while a weaker donor character (*i.e.*, higher ionisation potential) results in a richer self-assembly behaviour, with the formation of complex low dimensional supramolecular structures. This is related to the possibility for a donor molecule to become a cation upon injection of one or even more electrons into a metal substrate (*i.e.*, *integer charge transfer* (ICT)), which would then screen the charged molecule to generate a strong surface dipole. Therefore, several molecular ions adsorbed on a metal would translate into an equal number of charge transfer dipoles (directed normally with respect to the surface), which would repel each other adding a long-range energy term proportional to R^{-3} (R being the distance between dipoles), competing with short-range van der Waals attraction. This balance between competing forces is analogous to those observed in many other physical systems [92,93] and it suggests that the control of the energy level alignment at the metal-organic interface – that would constitute in itself a formidable achievement – could be the key to control supramolecular self-assembly by tuning the ratio between short-range attraction and long-range repulsion.

Beside self-assembly alterations, surface dipoles are important because they shift the vacuum level of the metal-organic interface, with the effect of modifying the work function of the metal by as much as 0.5−1 eV, thus playing an important role in the control of the energy level alignment at the interface (see Chapter 1, Section 1.3). This is fundamental in organic electronics, since pinning the Fermi level of the molecular charge carriers to the one of the electrode guarantees the efficient charge transport and thus the efficiency of a hypothetical optoelectronic device [42,94].

3.1.1 *Selection of surface and molecule*

The aim of our study is to understand the formation of charge transfer dipoles at the metal-organic interface, in order to determine whether this process can be controlled *a priori* via a careful choice of molecule and metal. In this regard, the first condition to be met is that the ionisation potential and Fermi energy of the chosen molecule and substrate are close enough to permit charge migration. Secondly, to achieve full control over the processes occurring at the interface, it is quite helpful to work with molecules that cannot establish strong coordination bonds with the surface. In this way, complex behaviours introduced by strong hybridisation at the interface are avoided [95] and the gas phase electronic structure of the adsorbed molecule is preserved, allowing a more direct comparison between experimental and theoretical results. Moreover, weak adsorption enables high molecular mobility, which is useful to avoid kinetic limitation in the self-assembly process and thus, to observe the formation of low dimensional patterns deriving from repulsion between weakly adsorbed molecular ions.

Cu(111) and Au(111) were identified as suitable substrates to match the aforementioned requirements. Their atomic-level flatness results in a smooth potential energy surface [96], whose effect is to ensure high planar mobility of physisorbed molecules. Furthermore, while the work function of both Cu(111) and Au(111) (4.9 and 5.3 eV, respectively) is in line with the typical ionisation energy of PAH hydrocarbons, their difference is still sufficient to result in a greater "oxidising power" for the nobler gold surface.

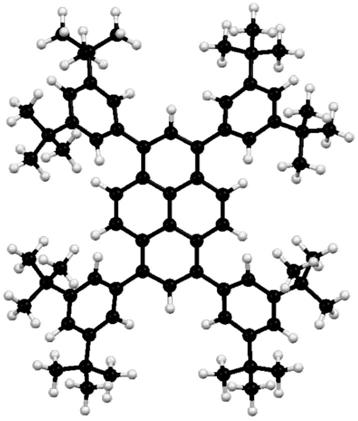

Figure 3.1 Ball-and-stick model of TBP molecular structure (colour code: black C, white H).

About the organic side, we designed a model tecton derived from pyrene, namely tetra[1,3-di(*tert*-butyl)-phenyl]-pyrene (TBP) (Fig. 3.1). The parent pyrene molecule was found to strongly interact with the Cu(111) surface [97], as revealed from the registry of self-assembled structures with the substrate (consistently with what observed for other planar pyrene derivatives on Au(111) [98]). Here, the strong interaction of the pyrene core with the surface was reduced with the addition of four symmetric 1,3-di(*tert*-butyl)-phenyl residues, which effectively increased the adsorption distance and, thus, decoupled the molecule from the substrate. It is noteworthy that the functionalization diminished the gas phase ionisation potential of TBP to 6.15 eV (to be compared to 7.39 eV for the parent pyrene), a value much closer to the Fermi level of Au(111). This effect produced important consequences on the energy level alignment at the metal-organic interface, which will be thoroughly discussed in the next Sections, where the supramolecular self-assembly of TBP will be characterised by means of scanning probe techniques and theoretical modelling.

3.2 Methodology

Before addressing the characterisation of the system of interest, we provide here the details of the theoretical and experimental methodology used in the next Sections. This includes DFT and classical molecular dynamics calculations, together with STM imaging and work function measurements by means of STS.

3.2.1 *Computational methods*

DFT calculations were performed with the plane-wave package Quantum-ESPRESSO [99], using ultrasoft pseudopotentials [79] and the PBE-GGA exchange-correlation functional [100] within the non-local vdW-DF formalism [74] to account for dispersion interactions. The molecular structure was relaxed both in gas phase and on the substrate, with wavefunction energy cutoff of 408 eV and 204 eV, respectively. The calculations of charge transfers to the substrate were re-computed increasing the cutoff to 408 eV. The sampling of the Brillouin zone was limited to the $\mathbf{k} = \Gamma$ point. The total energy of charged molecules was corrected accordingly to the Makov-Payne scheme [101], while a counter dipole term [102,103] was included in molecule-surface calculations. Au(111) and Cu(111) surfaces were approximated with a two-layered slabs (equivalent to a 9×9 cell), allowing ~10 Å vacuum between periodic replicas. Only forces acting on the first metal layer and the molecular atoms were minimised during structural optimisation (up to 0.026 eV/Å).

Classical molecular dynamics simulations were carried out with the LAMMPS and Amber packages [104,105], using the General Amber Force Field (GAFF) [106] to model the geometry and the intermolecular interactions of TBP molecules. Non-bonded interactions at the metal-organic interface were described using a semi-empirical force field fitted from experimental desorption energies of organic molecules on Au(111) and second order perturbation theory (MP2) calculations [69]. This parameterisation was assumed to be valid also for the Cu(111) surface, since the measured adsorption energies of small π-conjugated hydrocarbons – *e.g.* ethylene, benzene and naphthalene – on Cu(111) [107] and Au(111) surfaces [108] are nearly equivalent. The structural relaxation of metal atomic layers was not considered to affect the molecular self-assembly. Hence, metal atom positions were kept fixed by setting to zero all their force components [109]. All atomistic models were prepared with the Mercury crystal structure analysis package [110].

3.2.2 *Experimental methods*

STM experiments were performed with a commercial variable-temperature STM (Createc) operated in ultrahigh vacuum (typical residual pressure of 4×10^{-11} mbar). Cu(111) and Au(111) crystal surfaces were prepared via repeated cycles of Ar^+ sputtering (1 keV) and annealing (up to 800 K). After complete degassing, TBP molecules were deposited by means of organic molecular beam epitaxy (OMBE) onto the metal crystals held at 300 K. STM images were acquired after quenching at 77 K, using chemically etched tungsten tips in the constant current mode. Typical values for bias voltage and tunneling current were $V = -2$ V (occupied state imaging) and $I = 20$ pA.

Spatial variations of the sample work function (work function maps) were measured by means of STS experiments, where a sinusoidal modulation voltage was added to the z-piezo controlling the STM tip height, via an external lock-in amplifier, and recording the induced alternating current output. Measurements were done using modulation frequencies of 3÷5 KHz (higher than the bandwidth of the z-piezo feedback system [63]) and peak-to-peak amplitudes of 0.2÷0.6 Å, with the sample chamber temperature kept at 5 K. All STM images were processed using the WSXM software [111].

3.3 Self-assembly of TBP on Cu(111) and Au(111): STM analysis

We begin our discussion by presenting the STM characterisation of TBP self-assembly upon deposition on the Cu(111) and Au(111), performed by Ada Della Pia (University of Warwick, Coventry). The experimental outcomes will be then thoroughly investigated by means of *ab initio* and classical theoretical modelling.

Upon deposition on both substrates, single TBP molecules appeared as eight bright lumps arranged at the perimeter of an oval. These features are attributed to the *tert*-butyl residues, with the four internal ones being brighter (*i.e.*, higher) than the external ones (Fig. 3.2 left panel). These observations are in good agreement with the molecular dynamics adsorption conformation (which was further relaxed at the DFT level (Fig. 3.2 right)). For both the Cu(111) and Au(111) substrates, the calculated structures show a significant deviation from planarity for the pyrene core (which assumes a pronounced saddle shape), while the (*tert*-butyl)-phenyl substituents are forced to rotate upwards due their mutual steric hindrance and the presence of the substrate (see Fig. 3.8). This concave adsorption geometry produces a permanent molecular dipole of 0.90 and 1.53 D on Cu(111) and Au(111), respectively.

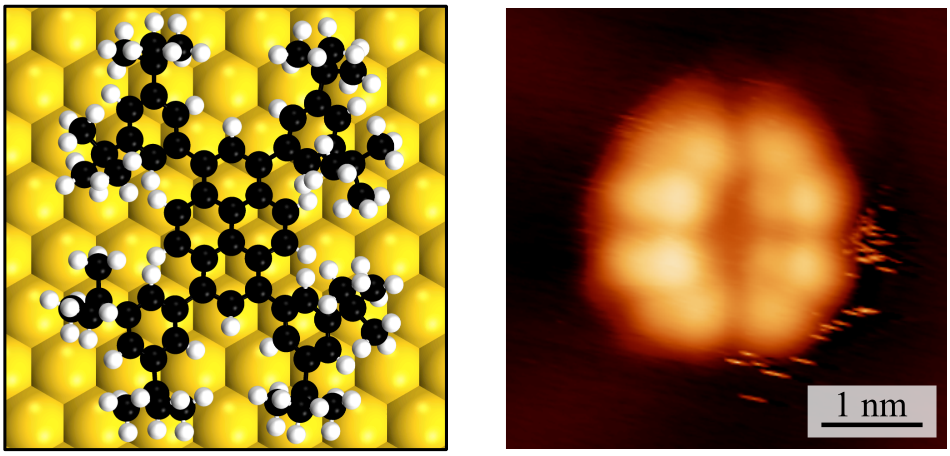

Figure 3.2 *Right*: top view of the DFT-optimised adsorption configuration of TBP on Au(111). *Left*: STM rendering of an isolated molecule (−2 V bias voltage).

STM imaging of deposited TBP molecules revealed their tendency to self-assemble, with hexagonal packing, into compact islands on both metal surfaces, similar to what was observed for a wide range of molecular species [17]. Consistently with a weak molecule/molecule and molecule/surface interaction regime, the *evaporation* of TBPs from the edges of the aggregates was found to occur on both Au(111) and Cu(111) at the liquid nitrogen temperature (~77 K) and isolated molecules were observed only in the presence defects or impurities, which suggests that molecular diffusion must be highly activated at any higher temperature. However, the size and distribution of molecular islands was very different on the two metals.

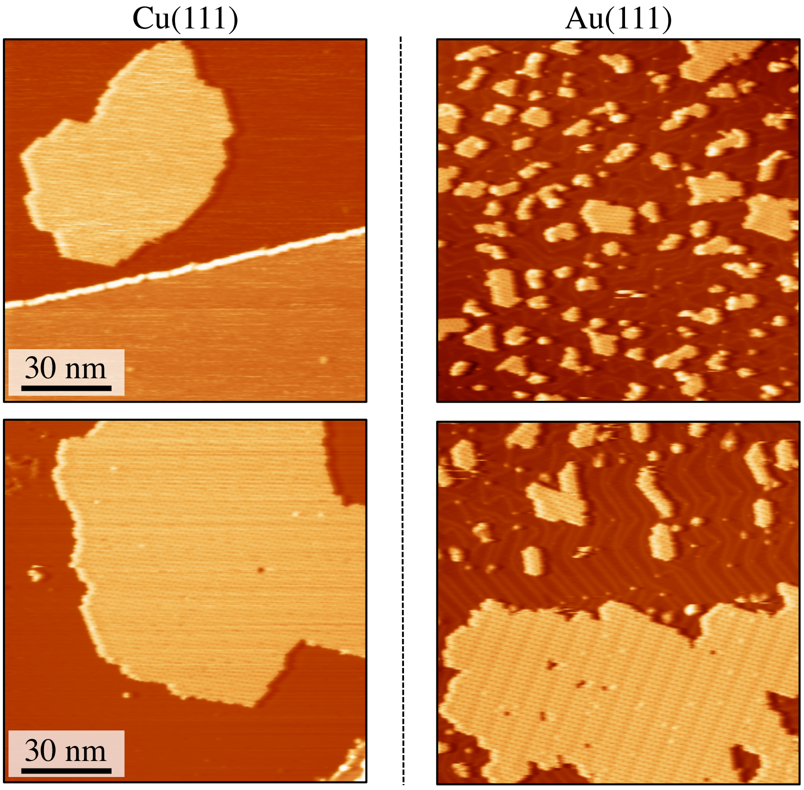

Figure 3.3 Supramolecular self-assembly of TBP on Cu(111) and Au(111) (left/right panels) at low and high coverage (top/bottom). The metal surface appears in dark orange (–2 V bias voltage for all images).

We observed the formation of large, typically single TBP aggregates on every Cu(111) terrace (Fig. 3.3 left panels), which can be regarded as the result of a standard Ostwald ripening process [112]. This implies that the self-assembly of TBP on copper is driven solely by van der Waals intermolecular interactions. Unsurprisingly, the average size of the single islands was found to increase with the molecular coverage, and annealing cycles at temperature up to 400 K did not result in altering the observed self-assembly, which is an ulterior proof that the system is at the thermodynamic equilibrium. On the other hand, the molecular self-organisation found on Au(111) was completely different (Fig. 3.3 right panels). Our STM topographies revealed that, at low molecular coverage (< 0.4 monolayers, ML), the deposition of TBP produced the formation of several small aggregates, which appeared uniformly distributed over the terraces with no evident registry to the rims of the herringbone reconstruction of the surface.

3.4 Anomalous phase coarsening of TBP on Au(111): The fingerprint of charge transfer?

The observed high molecular mobility brought us to exclude that kinetically inhibited diffusion might be the origin of the self-assembly observed on the atomically flat Au(111) (whose limited reactivity and consequently smooth potential energy surface are well established [96]).

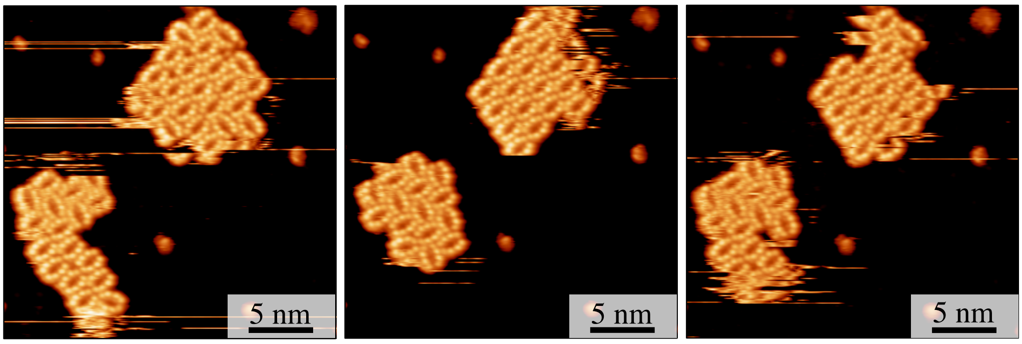

Figure 3.4 Sequence of STM images (taken with time interval of 5 minutes, from left to right), showing a couple of small clusters on Au(111) exchanging molecules with the environment (−2 V bias voltage for all images).

In case of kinetically limited growth, annealing cycles should increase/decrease the average cluster size/density as a function of the heating time and temperature [113,114]. However, our annealing experiments for time/temperature up to 20 min/420 K did not change the self-organisation of TBP on the Au(111) surface, eventually proving that the small islands shown in Fig. 3.3 are also an equilibrium structure.

STM frames taken with fixed time intervals confirmed that clusters exchange particles. By having a closer look at Fig. 3.4, the images show that the total number of molecules decreases from 43 to 36 (frame 1 to 2), and then increases to 41 (frame 2 to 3) in about 10 minutes. Even though very approximated, this allowed an estimation of the average "molecular sublimation rate" at 77 K ($N_2/N_1 = 0.042$, which is the ratio between "unbound" and "bound" molecules) and consequently of the intermolecular binding energy ΔE, since the Boltzmann population $N_2/N_1 = exp[-\Delta E / (kT)]$ links the two quantities. The cohesive energy is estimated in the range 0.06–0.12 eV/molecule, consistently with the highly activated evaporation and exchange of molecules between clusters at the liquid nitrogen temperature.

The experimental observations are thus suggesting a thermodynamic explanation for the self-assembly of TBP molecules on Au(111), which we refer to as *anomalous ripening*, in contrast with the standard Ostwald ripening observed on the less noble Cu(111) surface. As is usually the case, attractive interactions alone cannot produce a self-assembly different from the collective aggregation of molecules [17] (as consistently found for TBP deposited on Cu(111)), especially when no strong coordination with the substrate hampers molecular diffusion. For this reason, we suggest that a second interaction opposite to the van der Waals forces must be present to explain the distribution of the isolated aggregates observed on Au(111). We tentatively interpret this unexpected structure as the fingerprint of charge transfer, which is occurring via donation of one electron from a TBP molecule to the gold surface (*i.e.*, ICT). This surface mediated "oxidation" would result in the presence of adsorbed molecular cations, which mutually repel each other as standing positive dipoles (due to the image charge effect deriving from the metal polarisation). The observed self-assembly on Au(111) could be then understood as the result of a fine balance between attractive dispersion and repulsive dipolar interactions. This hypothesis will be validated all along the discussion by means of *ab initio* modelling, scanning tunneling spectroscopy experiments and an *ad hoc* Monte Carlo lattice gas model.

However, a first support for our tentative explanation was offered by the analysis of the molecular tiling in the aggregates. In fact, TBP molecules adsorbed on Cu(111) were found to self-organise following a "zigzag" pattern only (where one half of the molecules is rotated by 90°, Fig. 3.5, left), while on Au(111) they can adopt either the same "zigzag" or a less dense "row" tiling (where all the molecules are parallel with respect to their major axis, Fig. 3.5 right) even within the same island, without apparent distortion of the structure (Fig. 3.6).

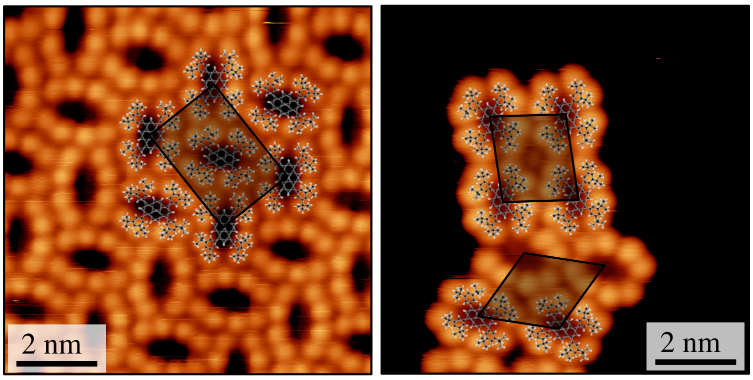

Figure 3.5 "Zigzag" (left) and "row" (right) tiling observed in TBP aggregates on Au(111). Molecular dynamics models are superimposed, together with experimental unit cells (shades).

Our classical force field estimated the cohesive energy for neutral molecules packed in the "row" tiling to be ~0.05 eV/molecule lower than that calculated for molecules in the "zigzag" one (molecular dynamics structures are superimposed to STM topographies in Fig. 3.5). This identifies the latter as the preferred packing for neutral TBPs (*i.e.*, neutral molecules can produce only "zigzag" islands), in agreement with our observations on Cu(111).

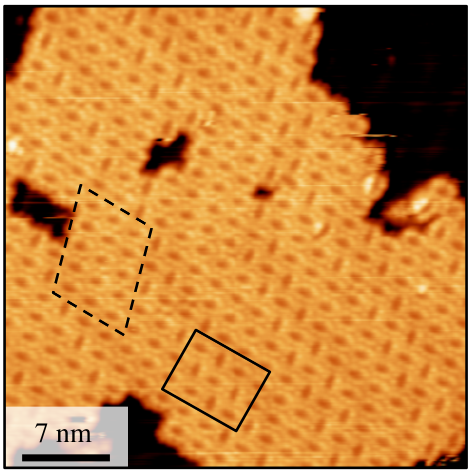

Figure 3.6 Large TBP island where both tiling patterns are observed (Au(111)).

On the other hand, the less dense tiling motif observed on Au(111) seems to indicate that charging is actually present. Indeed, despite the smaller cohesive energy, the new unit cell would favour the self-assembly of charged elements, it allows a slight increase of the intermolecular distance and therefore a significant reduction of the hypothesised electrostatic repulsion.

3.5 DFT model of the gas phase and adsorbed TBP molecule

We will present here the DFT-based modelling we have performed, with the aim to disclose the phenomena at the origin of the different self-assembly behaviour observed for TBP molecules adsorbed on Cu(111) and Au(111). This analysis will be further developed in Sections 3.6 and 3.7, where we will show how, by combining *ab initio* calculations, surface screening models and STS experiments, we could obtain a more complete picture strongly supporting the hypothesis that TBP molecules are subjected to charge transfer when adsorbed on Au(111), while they remain in their neutral state on Cu(111).

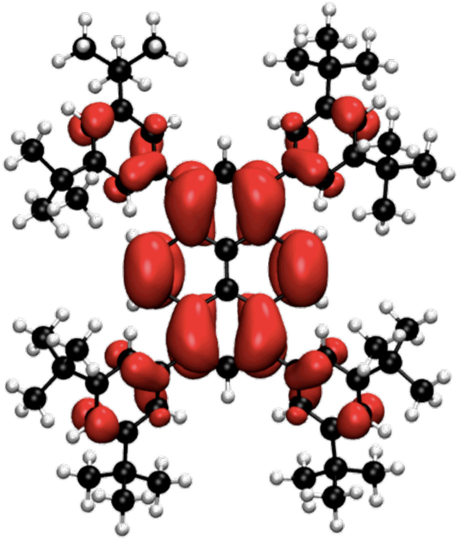

Figure 3.7 HOMO spatial distribution for gas phase TBP (courtesy of Dr A. Floris).

Calculations were carried out for both the gas phase and the adsorbed TBP molecule, in order to test the effect of the interaction with the metal substrate on its electronic properties.

The gas phase molecular HOMO orbital is mainly located in correspondence of the pyrene core, but it shows features extending on the lateral (*tert*-butyl)-phenyl residues (Fig. 3.7). The higher delocalisation of the TBP HOMO in comparison to that of the unsubstituted pyrene translates into a significant reduction of the gas phase ionisation potential (I = 6.15 eV and 7.39 eV, respectively). This result reveals the fundamental importance of TBP functionalisation, as moving the HOMO level closer to the Fermi energy of Au(111) (5.3 eV) favours the charge transfer to the surface, consistent with the observed self-assembly and our hypothesis. The gas phase ionisation potential was simply obtained from total energies difference as $I = E_{N-1} - E_N$, N being the total number of electrons. We note that no structural relaxation was performed upon electron removal and that the Makov-Payne correction was applied for the total energy calculation of the charged molecule [101].

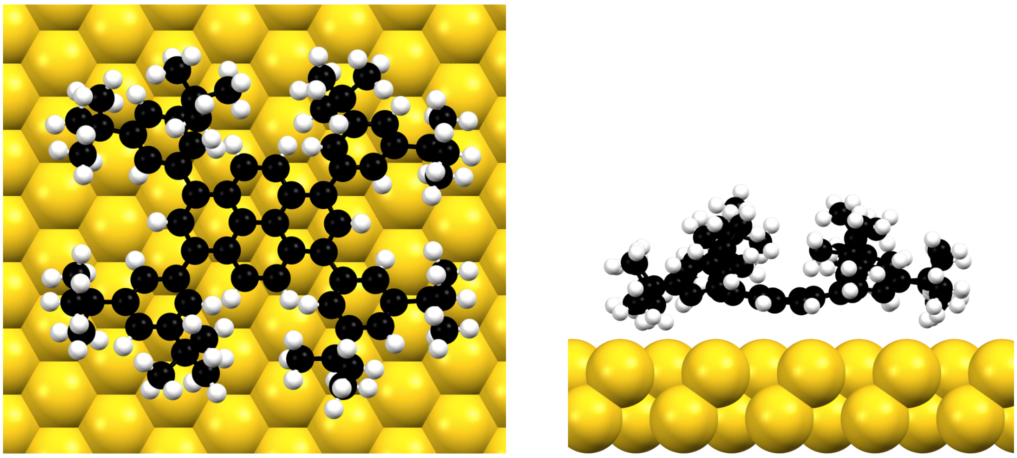

Figure 3.8 Top (left) and side (right) view of the calculated adsorption equilibrium structure.

The calculated molecular adsorption conformation is presented in Fig. 3.8. The substantial non-planarity of adsorbed TBP leads to a non-negligible intrinsic dipole, which is defined as the electrostatic dipole calculated in the gas phase for the molecule in its adsorption conformation. The average distance between the pyrene core and the topmost surface layer was 3.59 and 3.65 Å for Cu(111) and Au(111), respectively. The relatively large separation between the molecule and the substrate is consistent with a physisorption picture and, owing to the concave adsorption geometry, the distance between the molecular centre of mass and the surface was significantly larger (*i.e.*, 4.34 Å and 4.68 Å for Cu(111) and Au(111)). We note that the different values for the molecular intrinsic dipoles derives indeed from the different vertical extension of the molecule on the metal (values for TBP adsorbed on Cu(111) and Au(111) are 0.90 D and 1.53 D, respectively).

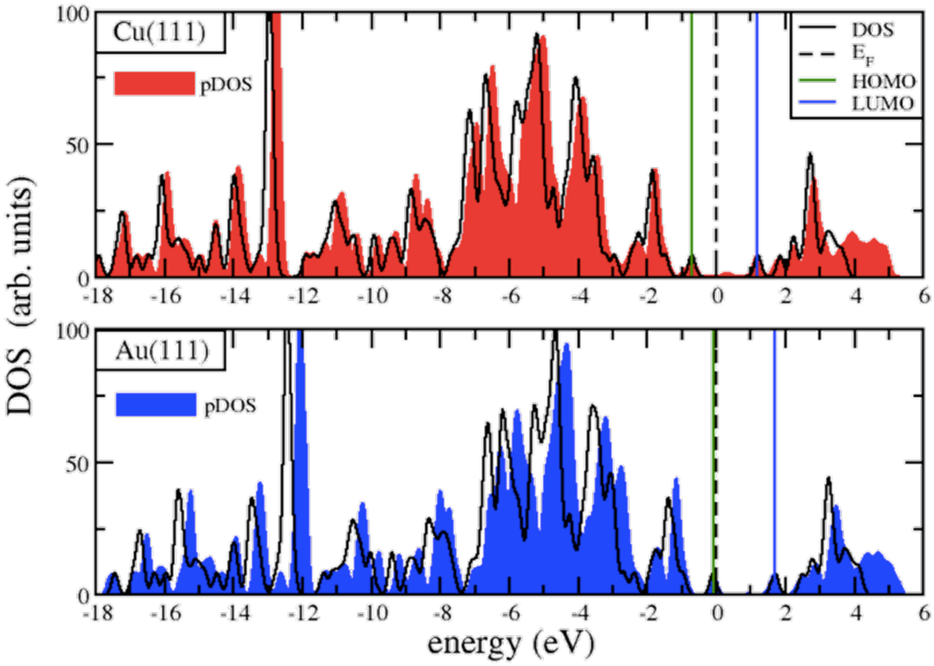

Figure 3.9 pDOS of TBP on Cu(111) and Au(111) (filled areas), compared with the gas phase molecular DOS (solid back line). The gas phase DOS was aligned to match the HOMO/LUMO peaks of the adsorbed molecule (courtesy of Dr A. Floris).

The pDOS of an adsorbed TBP molecule, together with the gas phase molecular DOS, are shown in Fig. 3.9 for both substrates. The pDOS were calculated as $\mathrm{pDOS}(\varepsilon) = \sum_{n\mathbf{k}i} \delta(\varepsilon_{n\mathbf{k}}-\varepsilon)\, |\langle \psi_{\mathrm{n}\mathbf{k}} | \psi^{i} \rangle|^2$, where ψ^{i} are (pseudo) wave functions of molecular atoms, $\varepsilon_{n\mathbf{k}}$ and $\psi_{n\mathbf{k}}$ are the Kohn-Sham eigenvalues and eigenstates and the indices n and $\mathbf{k}$ identify the bands and Bloch vectors, respectively. We find no significant broadening of the frontier molecular orbitals or hybridisation with surface states upon adsorption, further indicating weak physisorption on both metals. We note that the absence of chemical interaction is very likely due to the large molecule-surface distance, differently to more planar PAHs for which mixing between molecular and metal states was observed [95,115]. In this case, the most relevant surface induced effect is the shift of the HOMO level of TBP adsorbed on Au(111), which results in it being aligned to the Fermi level of the metal (whereas HOMO lays below Fermi for TBP on Cu(111)). This result is generally interpreted as an indication of partial occupation (the corresponding fractional value is an artefact due to the well known limitations of standard DFT functionals [100]), further indicating that the molecule can act as an electron donor only when adsorbed on Au(111). However, the nearly null spatial overlap between the molecular and surface wave functions suggests the occurrence of ICT [45,115] from the molecule to Au(111).

3.6 Effect of the surface screening: energy level alignment of TBP upon adsorption

A natural test for assessing the occurrence of ICT is the comparison of the molecular HOMO level relatively to the Fermi energy of the substrate. In fact, the energy of the frontier molecular orbitals is modified when a molecule arrives in the proximity of a metallic substrate.

The high polarisability of a metal results in the ability to effectively screen any external electric field (*e.g.*, a molecule or a molecular ion), in accord with the image charge model, with the result of upshifting/downshifting the HOMO/LUMO of an adsorbate and reducing the HOMO-LUMO gap. This means that the energy required to remove an electron from the adsorbate (*i.e.*, the ionisation potential/HOMO energy) will be reduced by the Coulomb interaction between the electron hole and its negative “reflection” in the metal slab. Of course, the same effect is expected for the opposite case, so that the energy gained in adding one more electron to a molecule (*i.e.*, electron affinity/LUMO energy) will be increased by the added interaction between the electron and its positive image inside the surface (see Section 1.3).

However, DFT calculations within the GGA approximation are not suitable to obtain the real HOMO-LUMO gap reduction [100], which was instead reproduced by GW calculations for weakly coupled systems [56]. Interestingly, the latter approach calculated a value for the HOMO upshift almost equal to the image charge correction, *i.e.*, the simple electrostatic interaction between a charge and its screened image. This allowed us to estimate the HOMO upshift for TBP upon charging as $P_{\mathrm{HOMO}} = -\,e^2 / 4(Z_{CC} - Z_{im})$, where Z_{CC} is the HOMO centre of charge and Z_{im} is the position of the surface image plane [116].

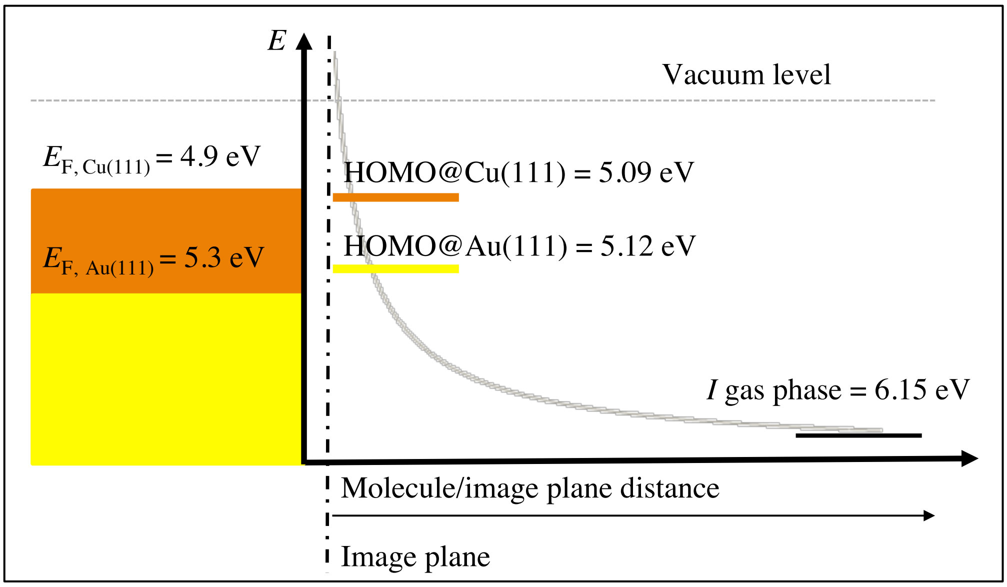

Figure 3.10 Schematic representation of the energy level alignment at the TBP/metal interface. The molecular HOMO shifts above the metal Fermi level upon adsorption on Au(111), making the transfer of one electron from TBP to the surface energetically possible (see text).

The calculated P_{HOMO} = 1.24 eV for a TBP molecule adsorbed on Au(111) decreases the ionisation potential to an effective I_{eff}= 4.91 eV, significantly below the surface work function (5.3 eV), making the donation of one electron to the substrate energetically favoured. On the contrary, by applying the same correction to a TBP molecule adsorbed on Cu(111), the calculated effective ionisation potential is higher than the surface work function by ~0.06 eV. This positive difference (which we can refer to as a “hole injection barrier”) indicates that copper would less likely succeed in oxidising for its lower work function (4.9 eV).

Moreover, the concave adsorption geometry of TBP is expected to produce itself a correction to the P_{HOMO} upshift, which has to be added to the above-calculated electrostatic term. In fact, the bent molecular conformation was found to generate an intrinsic positive dipole, which acts in the direction of slightly opposing CT. The consequent HOMO downshift was calculated by means of a classical capacitive model as 0.21 and 0.13 eV for Au(111) and Cu(111) adsorption respectively [35,117]. This second effect takes the differences between the work function of the substrates and the HOMO of the adsorbed

TBP to the final values of $\Delta I_{\mathrm{Au}} = -0.18$eV and $\Delta I_{\mathrm{Cu}} = 0.19$ eV, which enforces the picture of neutral adsorption on Cu(111) for the increased hole injection barrier (from 0.06 to the actual 0.19 eV) (Fig. 3.10). The confirmed negative value obtained for TBP adsorbed on Au(111) further supports the prediction of ICT, which implies the formation of molecular ions and consequentially of strong vertical dipoles.

3.7 Work function modulation at the metal-organic interface

Scanning tunneling spectroscopy (STS) experiments were carried out to look for a fingerprint of ICT. Indeed, the presence of ICT molecular dipoles is expected to generate a local electric field with a strong reduction of the local work function ϕ as main effect [118].

To this aim, the surface work function was thoroughly resolved by measuring the tunneling current *vs*. STM tip/sample distance spectra ($I(z)$), as a function of the tip position on the sample [118-120]. The adopted experimental set-up allowed the molecular-resolved mapping of the surface work function shift $\Delta\phi\,(x,y) = \phi\,(x,y) - \phi_{\mathrm{M}}$, where $\phi\,(x,y)$ is the work function detected in the position (x,y) and ϕ_{M} its value on the clean metal. The analysis of the maps shown in Fig. 3.11 (*a*) and (*b*) revealed a diminution of the work function on molecular islands, which was calculated to be 0.2 eV more pronounced on Au(111) with respect to Cu(111) (Fig. 3.11 (*c*)).

However, charge transfer is not the only effect contributing to these negative $\Delta\phi$ values, since also the intrinsic molecular dipoles and the pillow effect modify the distribution of charge at the interface and therefore contribute to the measured value [26,42,45,94]. In this regard, DFT calculations were used in order to shed light on the relative weight of the different contributions to the total surface dipoles D_{tot}.

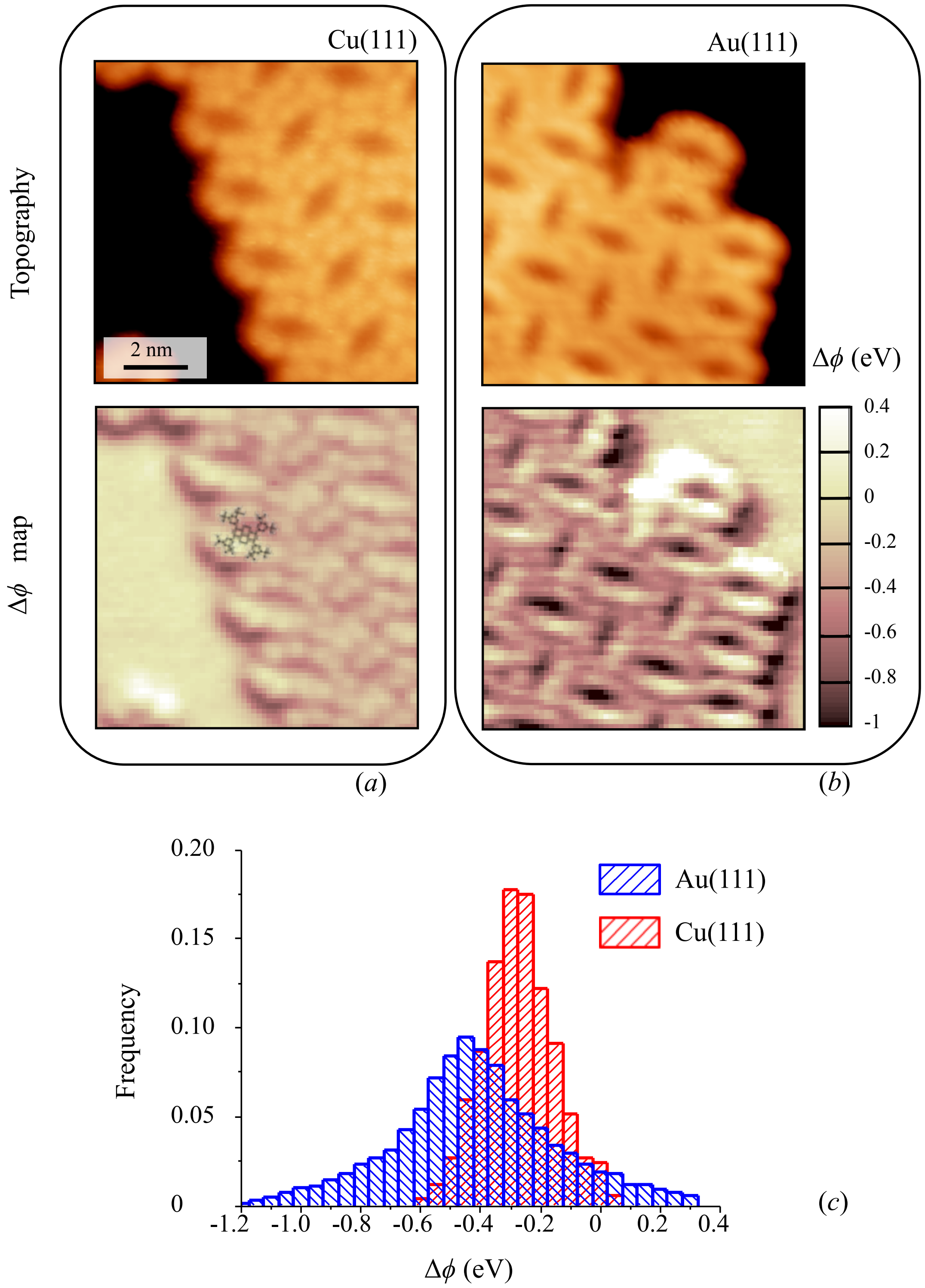

Figure 3.11 Constant current STM topographies and simultaneously acquired $I(z)$ maps on Cu(111) (*a*) and Au(111) (*b*). $I(z)$ maps show the work function variation $\Delta\phi$ with respect to the bare metal surfaces. The $\Delta\phi$ distributions measured on TBP islands are reported in panel *c*, for both metals.

The aforementioned total dipole can be considered as the sum of three components: $D_{tot} = D_{sub} + D_{mol} + D_{ind}$, the first one ($D_{sub}$) being the surface dipole of the bare metal surface (which is zero for a symmetric slab), the second (D_{mol}) being the intrinsic molecular dipole and the latter (D_{ind}) resulting from the molecule-metal interaction (*i.e.*, charge transfer and pillow effect). The total surface dipole calculated for a TBP molecule on Au(111) was 8.41 D, which compared to the intrinsic dipole (D_{mol} = 1.53 D) identifies the combined effect of charge transfer and pillow effect (D_{ind} = 6.88 D) as the main contribution. A similar behaviour was found on Cu(111), where the total dipole (D_{tot} = 4.74 D) was definitely smaller than the one on Au(111). Here the total dipole was attributed to the sum of the intrinsic dipole and pillow effect only (which is stronger on Cu(111) [121]), the charge transfer contribution being much lower on this surface.

Going back to the $\Delta\phi$ maps for TBP adsorbed on Au(111), their intramolecular resolution allowed us to observe a strong modulation of the local work function for TBP adsorbed on Au(111), which revealed a minimum (~ −1 eV) located within the pyrene core (Fig. 3.11 (*b*)). This modulation was much less pronounced on Cu(111) (Fig. 3.11 (*a*)).

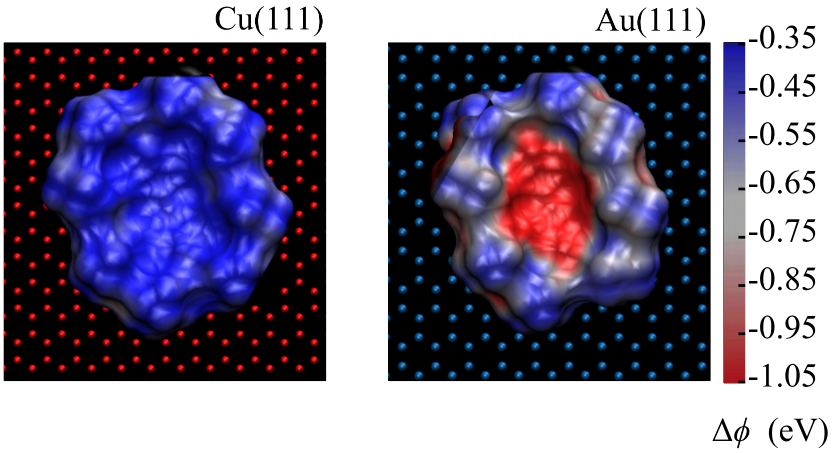

Figure 3.12 Calculated electrostatic potential energy shift ($\Delta\phi$) with respect to the clean metal surfaces for a single molecule adsorbed on Cu(111) (left) and Au(111) (right). The work function reduction is more pronounced upon adsorption on Au(111), consistent with donation of charge from the molecule to the gold surface.

This scenario was quantitatively reproduced at the DFT level by evaluating the electrostatic potential energy shift of an adsorbed TBP molecule, where the HOMO partial occupation – expected on Au(111) – was enforced by removing one electron. Similarly to the experiments, the $\Delta\phi$ was close to -1 eV on the molecular core, but definitely less pronounced in correspondence to the lateral residues (Fig. 3.12). Thus, the charge density distribution of a TBP molecule – upon withdrawal of one electron – resembles a positive hole state localised on the pyrene core. The electrostatic potential energy shift calculated for a neutral molecule adsorbed on Cu(111) did not show noticeable modulation, again in quantitative agreement with our experiments (cf. Fig. 3.11 (*b*) and Fig. 3.12). This result is consistent with a neutral adsorption picture, where a small reduction of work function is anyway expected for the stronger pillow effect on Cu(111) [121].

3.8 Increasing TBP surface concentration: Fermi level pinning

The physical picture emerging from the results presented so far suggests that adsorbed TBP molecules remain neutral on Cu(111), where they interact only through attractive van der Waals forces and form single large islands via standard Ostwald ripening process. Conversely, molecules adsorbed on Au(111) are expected to undergo ICT and to carry strong electrostatic dipoles because of the surface screening.

For this reason, the self-organisation of TBP on Au(111) can be explained in terms of the simultaneous presence of short-range van der Waals attractions and long-range electrostatic repulsion between molecular ions. It is known that the action of competitive forces – acting on different length scales – may drive the formation of characteristic patterns in a variety of physical systems [92,93], such as the formation of magnetic domains, camouflage patterns in animal skin/fur, block-copolymer organisation, as well as in two-dimensional supramolecular assembly [26,122-124], which is brought as a first simple explanation of the “bubble phase” (*i.e.*, anomalous Ostwald ripening) observed at low coverage (Fig. 3.3 right). At higher molecular deposition, bubble phases are expected to evolve to striped domains, in order to minimise the electrostatic repulsion by maximising the average intermolecular distance (provided that the ratio between attraction and repulsion does not depend on coverage).

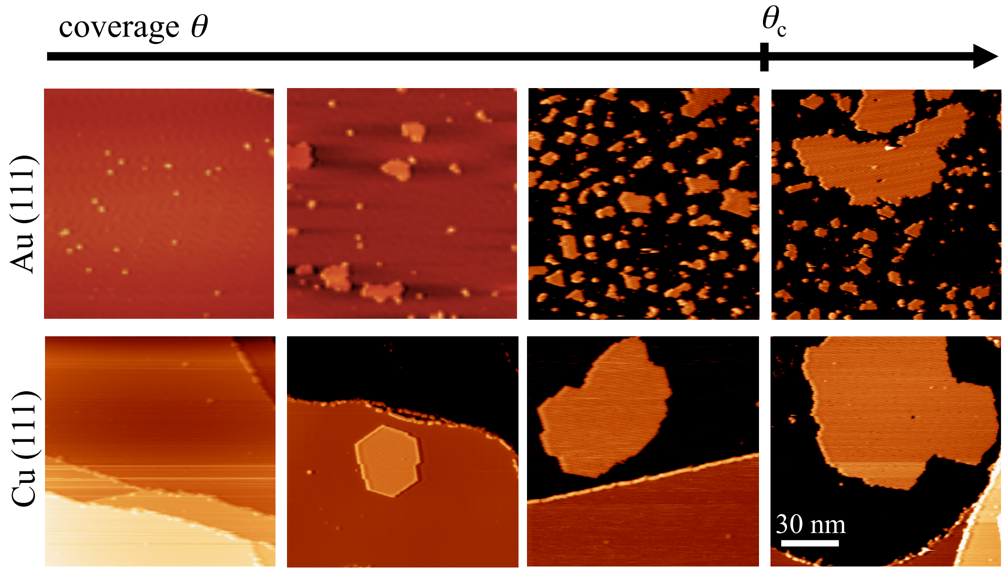

Figure 3.13 Self-assembly of TBP versus molecular coverage. The coexistence of small and large aggregates on Au(111) starts at critical coverage $\theta_c \approx 0.4$ ML.

However, our STM experiments at coverage $\theta \geq \theta_c = 0.4$ ML never revealed the presence of striped-phases, while showing instead the unusual coexistence of small and large islands (Fig. 3.13 for $\theta > \theta_c$). We attribute this behaviour to the self-limiting nature of ICT at the metal-organic interface, which become evident when the driving force (ΔI_{Au}) for charging an *isolated* molecule is small enough that the interplay of charging and assembly allows for a richer behaviour repertoire. Namely, charged molecules could reverse back to neutrality upon assembly if the local molecular arrangement made this energetically favourable.

An explanation may be attempted in terms of the general ICT picture, where the surface (positive) dipoles created by TBP ions generate an electric field which is expected to downshift the molecular energy levels – together with the vacuum level – towards the Fermi energy of the substrate [26]. In other words, the surface work function is lowered by gradually increasing the coverage, until no driving force is left for molecules to oxidise (*i.e.*, $\Delta I_{\mathrm{Au}} = 0$) and any further deposited molecule will adsorb in its neutral state [26,42,45,94].

This simplified mean field picture captures the self-limiting character of ICT and can be readily transferred to the local scale, where the driving force for ionising a single molecule depends on both the energy difference ΔI (between the HOMO level and the Fermi energy of the metal) and the electrostatic repulsion with its neighbours. Therefore, when a neutral molecule is located in the proximity of several already charged ones, its further electron donation might be inhibited. In a similar manner, a charged molecule might return to the neutral state, whenever the change results energetically convenient within the local environment. *Reversible* ICT can be used to rationalise the observed molecular assembly behaviour once molecular charging is allowed to depend *locally* on the electrostatic interaction between neighbouring molecules, and identifies the observed phase diagram as the growth pattern most likely to emerge in this complex situation.

3.8.1 *Monte Carlo model for the anomalous coarsening*

In order to shed light on the assembly behaviour observed on both Cu(111) and Au(111), we implemented a simple *Monte Carlo* (MC) model where TBP molecule were treated as structure-less particles, accommodated in a two-dimensional hexagonal lattice gas (Fig. 3.14). The short-range van der Waals attraction was described as a nearest neighbour coupling, while the electrostatic interactions – for the image charge effect due to surface screening – were modelled with a $1/R^3$ term, to take into account the repulsion between standing dipoles, positively oriented along the direction normal to the substrate. In this version of the dipolar Ising model [125], the dipole hosted by a particle could assume two possible values in relation to the state of charge of the particle itself: a small positive dipole was associated to the pillow and the intrinsic “conformational” dipole accompanying an adsorbed neutral molecule, while a much larger one was related to the molecular ion obtained after ICT.

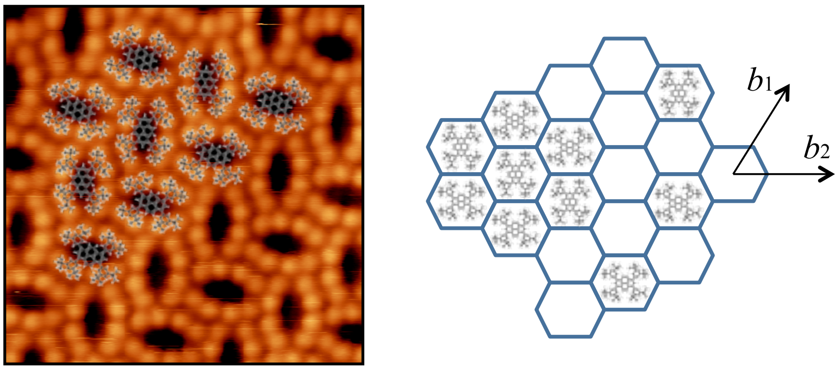

Figure 3.14 Molecular dynamics model (superimposed on a STM topography) highlights the hexagonal close packed self-assembly of a TBP island (left), which is described by a two-dimensional lattice gas in our Monte Carlo model (right).

The state of charge of each particle was permitted to swap between the two available conditions (*i.e.*, between charged or neutral), the selection being controlled by standard MC acceptance rate depending on total energy fluctuations. To allow for this non-trivial charge sampling, every particle was assumed to add an energy term equivalent to the difference between the HOMO level and the Fermi energy of the substrate for both Au(111) and Cu(111) (*i.e.*, the ionisation energy gain, which can be either negative or positive). All the above was summarised in the following Hamiltonian:

$$H = -J\sum_{\langle i,j\rangle}\sigma_i\sigma_j + \frac{1}{2}\sum_{\substack{i,j\\ i\neq j}}\frac{p(\delta_i)\,p(\delta_j)}{\left|\mathbf{r}_i - \mathbf{r}_j\right|^3} + N_c\Delta I \qquad [3.1]$$

Where: i, j are lattice site indexes; σ defines the state occupation ($\sigma = 1$ for an occupied site, 0 if vacant); J is the vdW coupling constant; $\langle i, j\rangle$ are nearest neighbour site pairs; $p(\delta_i)$ is the molecular dipole value at an occupied site i, and δ is a dipole-type flag, set to 1 for molecular ions and 2 for neutral molecules; $\mathbf{r}$ being the site position vector. The last term in the Hamiltonian in Eq. 3.1 accounts for the global ”ionisation gain”, where N_c is the number of charged molecules and ΔI is the energy gain/cost associated with the formation of a molecular ion from an adsorbed neutral molecule. It was proven that the chosen model potential, taken without the grand canonical $N_c\Delta I$ term, could result in the formation of bubble/island, striped or generally elongated phases, which are well known to occur in physical systems with competing interactions [92,125]. The presence of long-range dipolar energy contributions increases the computational cost (which scales as the square of the number of particles) and requires the employment of periodic boundary conditions (PBC) to avoid finite size effects. PBC were implemented by direct summation [126], which is much more accessible and at least as efficient as Ewald summation techniques in the two-dimensional case. For instance, the original system can be repeated in space to simulate the continuum, provided that its chosen geometry respects the periodicity and symmetry of the hexagonal lattice. The Hamiltonian in Eq. 3.1 can be rewritten to explicitly account for PBC:

$$H=\sum_{i,j}\sum_{\mathbf{R}}\left\{-\left[\Pi\left(\mathbf{r}_i,\mathbf{R}+\mathbf{r}_j\right)\sigma_i\sigma_j\right]+\frac{1}{2}\left[\Delta\left(\mathbf{r}_i,\mathbf{R}+\mathbf{r}_j\right)p\left(\delta_i\right)p\left(\delta_j\right)\right]\right\} \ , \qquad [3.2]$$

where **R** is a translation vector, which transforms the original system in any of its images and the functions Π (Eq. 3.3) and Δ (Eq. 3.4) account for the van der Waals nearest neighbours (NN) coupling and the repulsion terms, respectively:

$$\Pi\left(\mathbf{r}_i,\mathbf{R}+\mathbf{r}_j\right)=\begin{cases} J & \text{if } \mathbf{r}_i \text{ and } \mathbf{R}+\mathbf{r}_j \text{ are NN,} \\ 0 & \text{otherwise.}\end{cases} \qquad [3.3]$$

$$\Delta\left(\mathbf{r}_i,\mathbf{R}+\mathbf{r}_j\right)=\begin{cases} 0 & \text{if } \mathbf{r}_i=\mathbf{R}+\mathbf{r}_j, \\ \dfrac{1}{\left|\mathbf{r}_i-\mathbf{R}-\mathbf{r}_j\right|^3} & \text{otherwise.}\end{cases} \qquad [3.4]$$

The double sum in Eq. 3.2 can be calculated in advance, since it is dependent on the positions *i* and *j* only, making the Hamiltonian computationally equivalent to the case without long-range interactions (Eq. 3.5):

$$H=-\sum_{i,j}\Pi_{ij}\sigma_i\sigma_j+\frac{1}{2}\sum_{i,j}\Delta_{ij}p\left(\delta_i\right)p\left(\delta_j\right) \ , \qquad [3.5]$$

where

$$\Pi_{ij}=\sum_{\mathbf{R}}\Pi\left(\mathbf{r}_i,\mathbf{R}+\mathbf{r}_j\right), \qquad \Delta_{ij}=\sum_{\mathbf{R}}\Delta\left(\mathbf{r}_i,\mathbf{R}+\mathbf{r}_j\right) \ . \qquad [3.6, 3.7]$$

The effective interaction parameters (Eq. 3.6 and 3.7) include the van der Waals nearest neighbour energy as well as the dipole-dipole repulsion between two occupied positions and replicas and need to be calculated only once at the beginning of a MC simulation, which then scales linearly with the number of molecules. This allowed the search of the equilibrium configuration for large unit systems (10^5 adsorption sites, corresponding to a 200×200 nm^2 surface), which was useful to approach the real system size. This was useful for immediate qualitative/quantitative comparison with experiments and also positive in terms of improved accuracy (in fact, the underestimation of the dipolar contribution due to finite system size is minimal in this way).

The numeric values of the parameters included in the Hamiltonian are listed in Table 3.1 below. The van der Waals coupling constant J was calculated at the DFT level (vdW-DF functional [74]), while the charge transfer dipole was estimated from standard electrostatics within the image charge approximation and in the ICT limit (*i.e.*, $p\ (\delta = 1) = e\ (2\ l_\mathrm{D}) + D_{mol}$, where l_D is the calculated adsorption distance corrected to account for the image plane distance [26,116]). Finally, the dipole associated to a neutral molecule ($p\ (\delta = 2)$) was set to be equal to the intrinsic molecular dipole D_{mol}.

J	0.12 eV
$p\ (\delta = 1)$	13.06 ea_0
$p\ (\delta = 2)$	1.99 ea_0
ΔI_Au	–0.18 eV
ΔI_Cu	0.19 eV

Table 3.1 Parameters used in the model Hamiltonian. Note that any positive value of ΔI_Cu will effectively remove any driving force for molecular charging. We note that the molecule-molecule distance is set to the experimental value (18 Å).

MC trial moves included the exchange between occupied and empty sites and – as previously introduced – the switching of the state of charge of an occupied site along the Metropolis annealing simulations. This means that, besides diffusion steps, the allowed MC trial moves included swapping the dipole of each molecule between the lower value, corresponding to the net dipole of the neutral molecule, and the higher one calculated for the positive molecular ion. Again, the driving force for this process was provided by adding to the model Hamiltonian a ΔI contribution for each charged molecule. This quantity was set to our calculated values $\Delta I_{\mathrm{Au}} = -0.18$ eV and $\Delta I_{\mathrm{Cu}} = 0.19$ eV for TBP adsorbed on Au(111) and Cu(111), respectively. In a typical simulated annealing run, the temperature was decreased linearly from 300 to 77 K over 10^8 MC steps and then kept at 77 K for further 10^7 steps for data gathering.

Any positive value assigned to the ionisation gain (*i.e.*, $\Delta I > 0$) always resulted in disabling the charged state option, since a positive contribution adds a further energy cost to the constant/increased electrostatic repulsion after the retention/addition of an ICT dipole, causing to always accept the neutral state. Therefore, by setting $\Delta I > 0$, the simulated annealing runs invariably identified the global coalescence of particles to be the equilibrium configuration, as appropriate for the Cu(111) case and consistently with our observations (Fig. 3.15 left).

On the other hand, setting ΔI to a negative value revealed a more complex situation, since the net energy gain introduced can favour the charged state over the neutral one, provided that the repulsion maintained/added from the retention/addition of a molecular ion is compensated (*e.g.*, the $\Delta I = -\infty$ limit would always allow for the retain/creation of charge transfer dipoles). By setting the value of the ionisation gain to $\Delta I_{\mathrm{Au}} = -0.18$ eV in MC simulations at low molecular coverage (0.15–0.30 ML, Fig. 3.15 top right), particles were found to aggregate in several small islands, qualitatively matching our low coverage experimental observations (cf. Fig. 3.3 and Fig. 3.15).

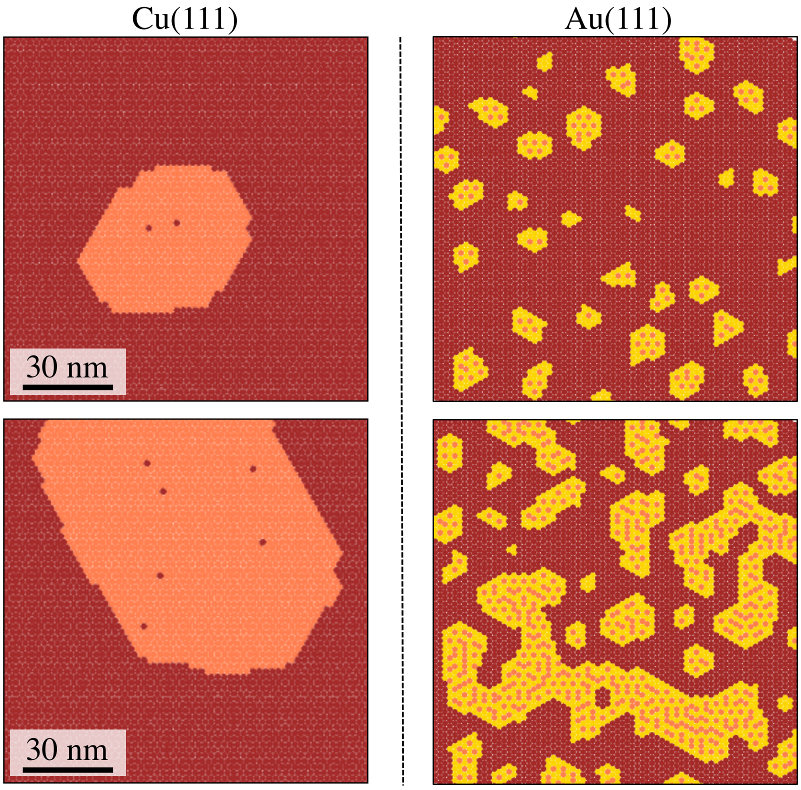

Figure 3.15 Monte Carlo simulations snapshots of the TBP molecules self-assembly on Cu(111) and Au(111), obtained allowing only neutral molecules (left), or both charged and neutral species (right). Neutral and charged molecules are represented in yellow and pink colours, top and bottom panels correspond to low (~0.2 ML) and high coverage (~0.5 ML), respectively.

Moreover, the good quantitative agreement between the experimental cluster size distribution and the one predicted from our simulations (Fig. 3.16) ultimately suggests that the inclusion of dipolar repulsion is both necessary and sufficient to reproduce the experimental observations, supporting our hypothesis that TBP molecules undergo ICT on the Au(111) surface.

For coverage exceeding 0.4 ML, simulations carried out in the $\Delta I = -\infty$ limit (*i.e.*, all particles are forced to the charged state) would always produce *striped* equilibrium configurations (Fig. 3.17 left). This morphology was never observed in our experiments in the same coverage conditions, which had shown instead the formation of larger aggregates, compatible with the average reduction of electrostatic repulsion at higher coverage (Fig. 3.17 right). As explained before, this is the expected outcome of the self-limiting nature of

ICT, since the state of charge, number and displacement of neighbours cause the variation of the net energy gained in "charging" a molecule.

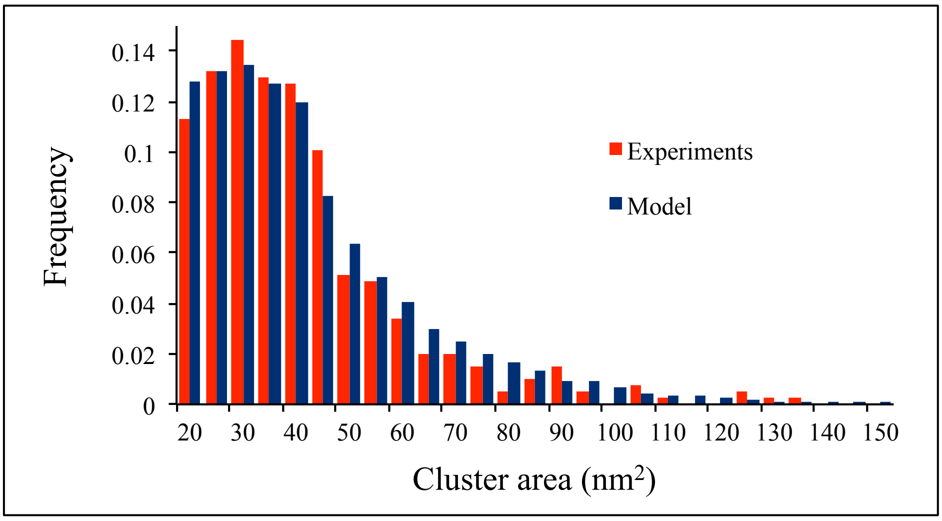

Figure 3.16 Cluster size population from MC simulations (blue) and experiments (red) for molecular coverage in the range 0.15–0.30 ML.

This relation was implemented in our model by setting the value of the energy associated with the formation of a molecular ion to the one calculated for an isolated TBP molecule adsorbed on Au(111). As a consequence, a MC move changing the state of a particle from neutral to charged (and *vice versa*) is accepted depending on the total energy variation in the system. For instance, let us suppose that a MC diffusion trial moves a charged molecule in the proximity of an area with high density of already charged ones. This would further increase the total repulsion energy, but instead of simply rejecting the move (which would be the case if the charging was irreversible, $\Delta I = -\infty$), the MC simulations might also accept the move (thereby gaining the attractive van der Waals interactions due to the increased number of nearest neighbours) by reverting the molecule to its neutral state. This method allows us to constrain the total number of charged molecules in the systems, which remains determined by the chosen value of ΔI, between the neutral and the totally charged limits (corresponding to a choice of $\Delta I > 0$ and $\Delta I = -\infty$, respectively). On the macroscopic scale, setting a threshold to the number of charged molecules can be considered equivalent to the condition of Fermi level pinning in charge transfer systems [42,94].

In this regard, our simulations showed that – by allowing the choice between a neutral and a charged state – the local crowding of molecular ions is permitted in small islands only, while it has to be limited in larger aggregates. The distribution of the molecular ions locally optimises the balance between the ICT energy gain and electrostatic repulsion, leading to the coexistence of small and large islands similarly to the experimental observations.

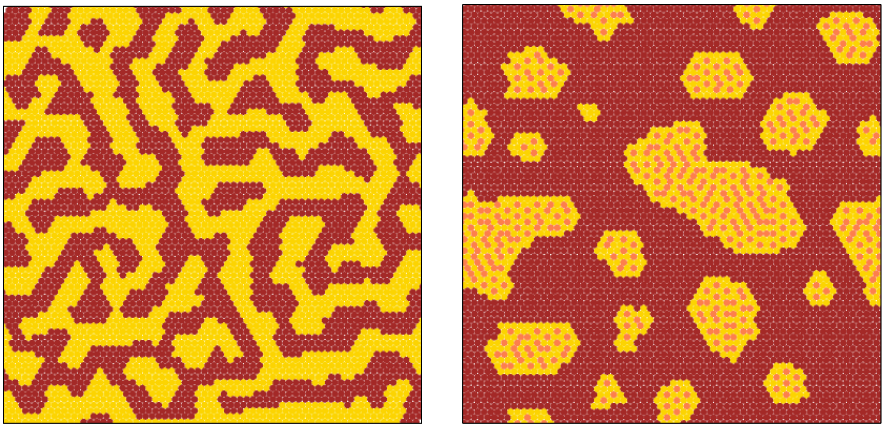

Figure 3.17 High coverage (0.4 ML) equilibrium configurations obtained from the MC simulation of the TBP/Au(111) system. *Left*: $\Delta I = -\infty$, corresponding to all molecules being ionised. *Right*: $\Delta I_{Au} = -0.18$eV, corresponding to the ICT situation. Charged molecules and neutral molecules are shown in yellow and pink colours, respectively (the substrate in brown).

The results obtained with our MC model have to be considered at best qualitative due the approximations included in the chosen model Hamiltonian, which were necessary in order to limit the number of parameters and guarantee their "availability". However, the very good agreement found between the experimental topographies and the calculated equilibrium structures strongly suggests that the self-assembly of TBP on the Au(111) is the result of the coexistence of neutral and charged molecules due to "reversible charge transfer" [26].

We finally note that our local work function measurements reveal charge transfer on Au(111) but no significant variations between different molecules of a given island. This is not surprising, since during the measurement of local work function at negative bias, the STM tip acts as a hole injector (locally changing the dI/dV spectrum [127]) on any neutral molecule capable of (or indeed selected for) hole accepting, such as TBP.

3.9 Conclusions

In this Chapter we investigated the effect of *reversible* charge transfer on the supramolecular self-assembly of TBP at the Au(111) surface. Theoretical modelling and STS experiments provided a comprehensive analysis of the energy level alignment at the metal-organic interface, which strongly suggests that charge donation can happen for TBP adsorbed on Au(111) but not on Cu(111). In this regard, we showed that ICT can be controlled with the *ad hoc* synthesis of molecular units designed to weakly adsorb on metal surfaces and with effective ionisation potential smaller (but still close) to the substrate work function. In fact, the presence of electrostatic repulsion between charged ICT cations was found to be both necessary and sufficient to explain the anomalous Ostwald ripening observed on Au(111). On the other hand, ICT related effects were not observed on a substrate with significantly lower work function such as Cu(111), where a different, purely attractive assembly behaviour was expected and indeed observed.

We suggest that our analysis can be extended to similar systems, where anomalous coarsening was observed but not directly addressed or explained [128-130], provided that a set of conditions is met at the metal-organic interface. First of all, the selected molecule must undergo charge transfer as an isolated adsorbate. Secondly, the monomer’s lateral size, dipole, and intermolecular van der Waals attraction must balance in such a way that the assembly driven by attractive short-ranged forces is moderated, while not forbidden, by the energy cost associated with long-range electrostatic repulsion. This can be achieved via appropriate selection of the adsorbate height (h) on the surface, to balance the ionisation energy gain ΔI (which is proportional to $-1/h$) and the dipole-dipole repulsion (proportional to h^2) at low coverage. Under these conditions, anomalous coarsening can occur only if *reversible* ICT is possible (not charge transfer due, *e.g.*, to irreversible deprotonation [27]). At low coverage, the equilibrium structure will eventually be achieved by limiting the assembly to small islands, while at higher coverage, much larger aggregates will be allowed to form, with some of the molecular ions reverting to the neutral state. These two island populations may be viewed as two phases characterised by a different fraction of charged molecules (a higher fraction can be accommodated in smaller islands for the same repulsion energy), which can coexist during the assembly. This mechanism evidences the self-limiting nature of charge transfer (*i.e.*, its reversibility), since the energy cost associated to the formation of an electron hole is expected to increase with the number of molecular cations.

Chapter 4

Codeposition of donor and acceptor molecules: TBP and TCNQ on Au(111)

Blending electron-acceptor and electron-donor molecules has come to prominence as a viable way to produce organic heterostructures, with unique electronic and optical properties [131]. For instance, such materials were found to have high electroluminescence (required for the production of OFETs or OLEDs), good photovoltaic response (bilayer organic solar cells are based on donor-acceptor coupling) and one-dimensional conductivity (for conductive coatings) [132]. These applications require the molecular blend to be deposited onto metal electrodes. The device performances will then rely on both electronic (energy level alignment [42,47], metal-organic hybridisation) and structural regularity aspects [11].

In this Chapter we will show that the donation of electrons from TBP molecules to the surface has the result of locally modifying the electronic properties at the interface, with the consequent activation of charge transfer for a second molecular species. This behaviour was observed after the codeposition of TBP and a prototypical strong electron acceptor molecule (7,7,8,8-tetracyanoquinodimethane (TCNQ)) on Au(111).

The molecular structure of TCNQ (shown in Fig. 4.1 (*a*)) is planar and rather rigid, due to the unsaturated B_3 bond. The core of the molecule is a hexagonal non-aromatic carbon ring linked to four cyano groups, which are responsible for its high gas phase electron affinity. Upon intake of one electron, which saturates the B_3 bond, the molecular stiffness is significantly reduced and the molecule is able to bend upon adsorption, with the cyano groups interacting more directly with the surface [133,134].

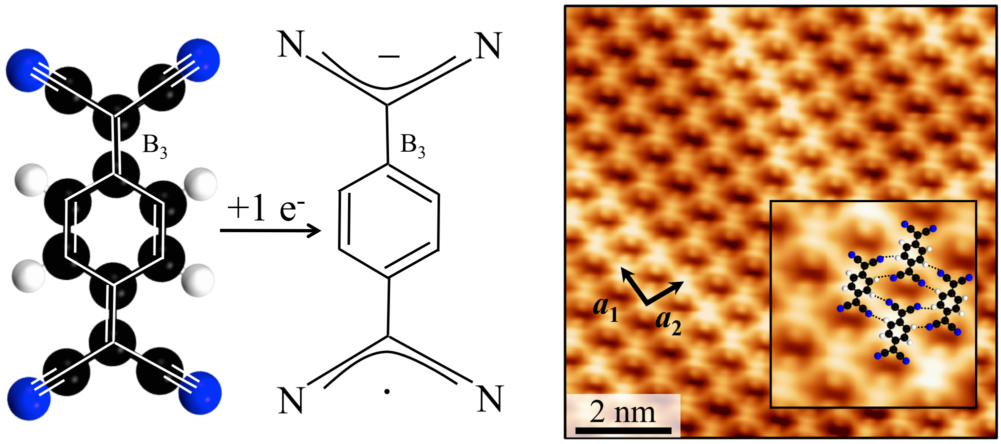

(*a*) (*b*)

Figure 4.1 *a*) Ball-and-stick and chemical structure of a TCNQ molecule. The addition of one electron aromatise the carbon ring and saturate the B_3 bond, increasing the flexibility of the molecule. *b*) Molecular layer on Au(111): the unit cell vectors are reported, together with the atomistic model of the H-bonded assembly. The herringbone reconstruction features are still visible.

The mentioned high electronic affinity of TCNQ was found sufficient to allow charge transfer with a range of alkali and transition metals [133,135-141] and upon deposition on several metal substrates [133,137,141-143], but not on the noble Au(111) surface. However, we will show that the codeposition of TBP and TCNQ on Au(111) produced a complex self-assembly phase diagram, where TCNQ was found to organise in structures that are associated to its $-e$ charge state. Therefore, we will conclude that TBP has to donate charge to effectively produce a local reduction of the surface work function, which is in turn required to activate the otherwise forbidden charge transfer from the Au(111) surface to the TCNQ molecules.

The work presented here is the result of a close collaboration with Daphne Stassen, Prof Davide Bonifazi (chemical synthesis, Université de Namur), Ada Della Pia and Prof Giovanni Costantini (STM/STS experiments, University of Warwick).

4.1 Introduction: TCNQ and TBP on the Au(111) surface

Before addressing the study of the codeposition (TBP/TCNQ)@Au(111), we aim to give a short description of the two separate sub-systems.

The strong acceptor character of TCNQ was observed to favour charge transfer upon deposition on several surfaces, including Ag(100) [141], Ag(111) [137], Cu(100) [133] and Cu(111) [142,143]. On the contrary, the molecular electronic affinity is not sufficient to oxidise the nobler Au(111) [137,144], which is more reluctant to lose electrons because of its higher work function. The neutral adsorption of TCNQ on Au(111) was confirmed by recent DFT calculations [145] and XPS experiments [137], where the observed spectrum was compatible with the one of uncharged TCNQ. Moreover, the substrate work function was reduced by 0.3 eV, instead of being increased as expected in case of electron transfer from the substrate to the molecules [137]. Similar results were obtained from STM and STS experiments. In particular, the STS spectra displayed features associated with empty LUMO levels, while the Au(111) herringbone reconstruction under organic layers showed no variation, indicating weak molecule-substrate interactions [144]. The weak coordination of TCNQ with the surface indicates neutral adsorption, since the rigid structure of the neutral molecule does not allow the molecule to bend the cyano terminals and to achieve a strong interaction with the metal [145].

The deposition of TCNQ on the Au(111) surface was characterised by means of low temperature STM, which revealed the assembly shown in Fig. 4.1 (*b*), consistently with previous observations [144]. The molecular self-assembly produced extended, faultless layers stabilised by a network of H-bonds, where the four hydrogen atoms of TCNQ interact with the electronegative cyano groups of four neighbouring molecules, leading to a rhombic unit cell ($a_1 = a_2 \approx 1$ nm).

This behaviour is very different to what we have observed for the self-assembly of TBP molecules on the same Au(111) surface. Indeed, in Chapter 3 we have shown and discussed the *anomalous phase coarsening* leading to the formation of distributed small supramolecular islands, whose origin was identified in the donation of electrons from TBP to the metal. Consistently, we found that the formation of charge transfer dipoles reduced the work function of Au(111) by few tenths of an eV. Here, we will show that the latter effect can radically change the self-assembly and electronic properties of TCNQ coadsorbed on Au(111). Our results will be compared to the case of pure TCNQ deposition, and characterised by means of local spectroscopy, DFT and Monte Carlo models.

4.2 Methods

DFT calculations and data processing were carried out with the Quantum-ESPRESSO package [99], using ultrasoft pseudopotentials [79] and the PBE-GGA exchange-correlation functional [100] within the non-local vdW-DF [74] formalism. Gas phase and on the substrate calculations were performed with a wavefunction energy cutoff of ~408 eV. The Brillouin zone sampling was expanded on a 4×6×1 Monkhorst-Pack grid, while a counter dipole correction was used for all “on metal” calculations [102,103]. The non-reconstructed Au(111) surface was modelled as a four-layer slab, allowing ~12.5 Å vacuum between periodic replicas. Forces acting on the metal and molecular atoms were relaxed up to 0.05 eV/Å (the bottom layer of the slab being constrained to the bulk positions).

STM experiments were performed with a commercial STM apparatus (Createc) operated in ultrahigh vacuum. The Au(111) crystal surface was cleaved and cleaned via repeated cycles of Ar^+ sputtering and annealed up to 800 K. Degassed TCNQ (commercially available) and TBP crystal powder were sublimated and codeposited by *organic molecular beam epitaxy* (OMBE) onto the metal crystal held at room temperature. STM images were acquired after quenching at 77 K and 5 K, using chemically etched tungsten tips in the constant current mode (typical voltage and tunneling current were V = -2 V and I = 20 pA). dI/dV spectra were acquired at 5 K.

4.3 Codeposition of TCNQ-TBP on Au(111): STM analysis

TBP and TCNQ molecules were sublimated and deposited on Au(111) at room temperature, spanning a range of relative coverage ratio (Ada Della Pia is acknowledged for the experimental characterisation).

For codeposition in the TBP:TCNQ = 3:1 ratio, our STM topographies showed the formation of rather small TCNQ islands decorated with a one-molecule-thick TBP frame (Fig. 4.2 left), with all the available TCNQ adopting this assembly (which we identify as "β"). On the other hand, the excess of TBP molecules was found to form homomolecular aggregates, with shape and size distribution similar to those observed for the deposition on Au(111) of TBP alone (see Chapter 3).

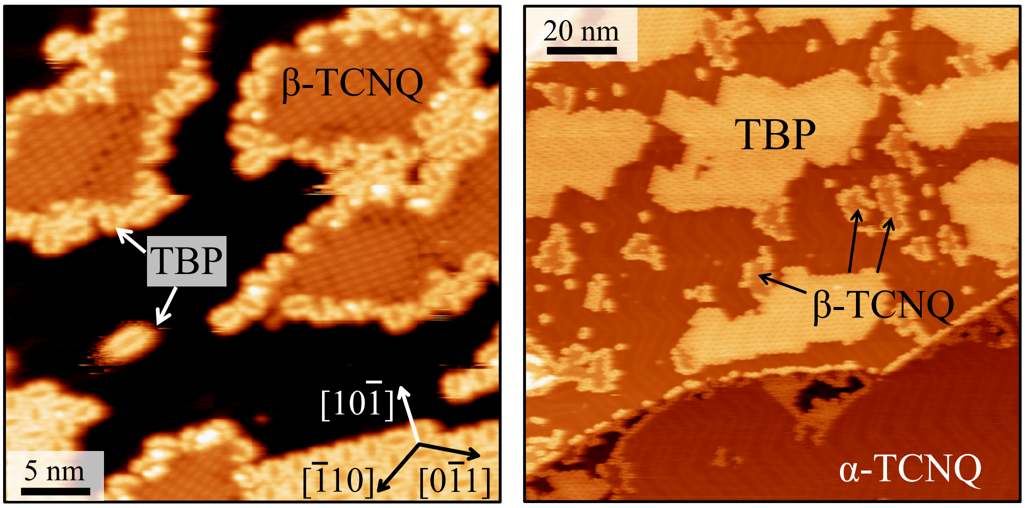

Figure 4.2 STM topographies showing the self-assembly of TBP and TCNQ codeposited on Au(111). *Left*) Close up view of β-TCNQ aggregates framed by TBP molecules. *Right*) For low TBP:TCNQ ratios the assembly is characterised by the coexistence of α- and β-TCNQ structures together with homomolecular TBP and TCNQ islands (−2 V bias voltage).

Reducing the TBP:TCNQ ratio, the codeposition led to a more complex situation, where TCNQ assembled again to form β assemblies, but was also observed to form extended H-bonded layers (Fig. 4.2 right). The latter structure is equivalent to what observed in [144] for TCNQ adsorbed on Au(111) (which we identify as "α-TCNQ"), whereas TBP molecules not constrained at the rims of β-TCNQ islands were still assembled as shown in Chapter 3.

The assembly of β-TCNQ is such that all molecules are aligned and almost perfectly parallel one with respect to the other (Fig. 4.4 (*c*) and (*d*)). The resulting molecular packing is denser than that of α-TCNQ, as revealed by the smaller dimensions of the unit cell (b_1 = (7.3±0.4) Å, b_2 = (11.1±0.4) Å, θ = (103±3)°). A simple analysis shows that this configuration cannot represent the energy minimum for neutral TCNQ, due to the electrostatic repulsion arising from the eclipsed displacement of the neighbouring electron rich nitrile moieties. Indeed, DFT gas phase calculations showed that the total energy of a TCNQ monolayer significantly decreases when shifting the relative position of neighbour molecules away from the experimental β unit cell, to avoid the local crowding of cyano groups (Fig. 4.3 left).

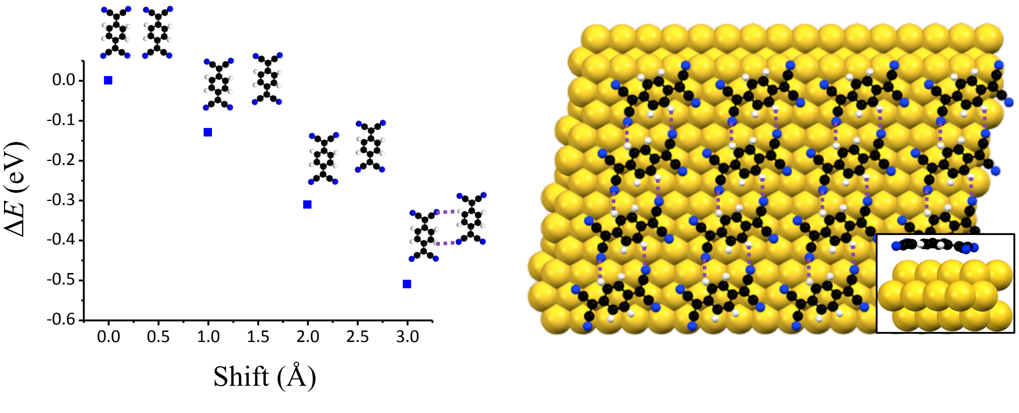

Figure 4.3 *Left*: total energy decreases when moving molecules away from parallel displacement (gas phase DFT calculations), *Right*: vdW-DF geometry optimisation showing how molecules initially positioned according to the experimental b-TCNQ unit cell tend to rotate to form H-bonds (dotted lines).

In a similar manner, DFT geometry optimisation of neutral TCNQ adsorbed on Au(111) – initially arranged to match the experimental β unit cell – resulted in an equilibrium structure where the distance between adjacent cyano moieties was maximised by in-plane rotation of the molecules, with the formation of two H-bonds per neighbour (Fig. 4.3 right). These results are consistent with previous works indicating the α H-bonded structure as the expected self-assembly template for neutral TCNQ on Au(111) [145].

However, TCNQ was found to self-assemble into β-like structures in proximity of step-edges on Cu(111) [142,143], on Cu(100) [133] and on Ag(111) [137]. Moreover, similar observations were reported for the deposition of the more electronegative fluorinated TCNQ (tetrafluoro-tetracyanoquinodimethane (F_4-TCNQ)) on Au(111) and Cu(100) [135,146]. All these reports associate the observed supramolecular structures to charge transfer effects, suggesting that β-TCNQs could as well accept electrons from the substrate. Since TCNQ by itself is expected to remain neutral on Au(111) and to form only α-structures, we attribute the occurrence of β phases – thus, of charge transfer – to the codeposition with TBP.

The first evidence supporting this statement was provided by the analysis of STM images of α- and β-TCNQ, taken at negative and positive bias voltage. Imaging of α-TCNQ showed that single molecules appear as elliptic bulges at negative voltage, while, switching to positive bias, they closely resemble the shape of the gas phase molecular LUMO. This indicates that no charge transfer occurs and that the interaction with the surface is weak [144] (Fig. 4.4 (*a*) and (*b*)).

Conversely, the imaging of single β-TCNQ molecules at negative voltage strikingly resembles the LUMO shape (Fig. 4.4 (*c*) and (*d*)), an effect that is usually observed in correspondence of partial occupation of the LUMO itself. The simultaneous presence of both α- and β-TCNQ in the same topography consented to exclude spurious effects related to the experimental setup, which safely allows us to conclude that the different molecular renderings mirror significant differences in the electronic structures, *i.e.*, that β-TCNQ is negatively charged.

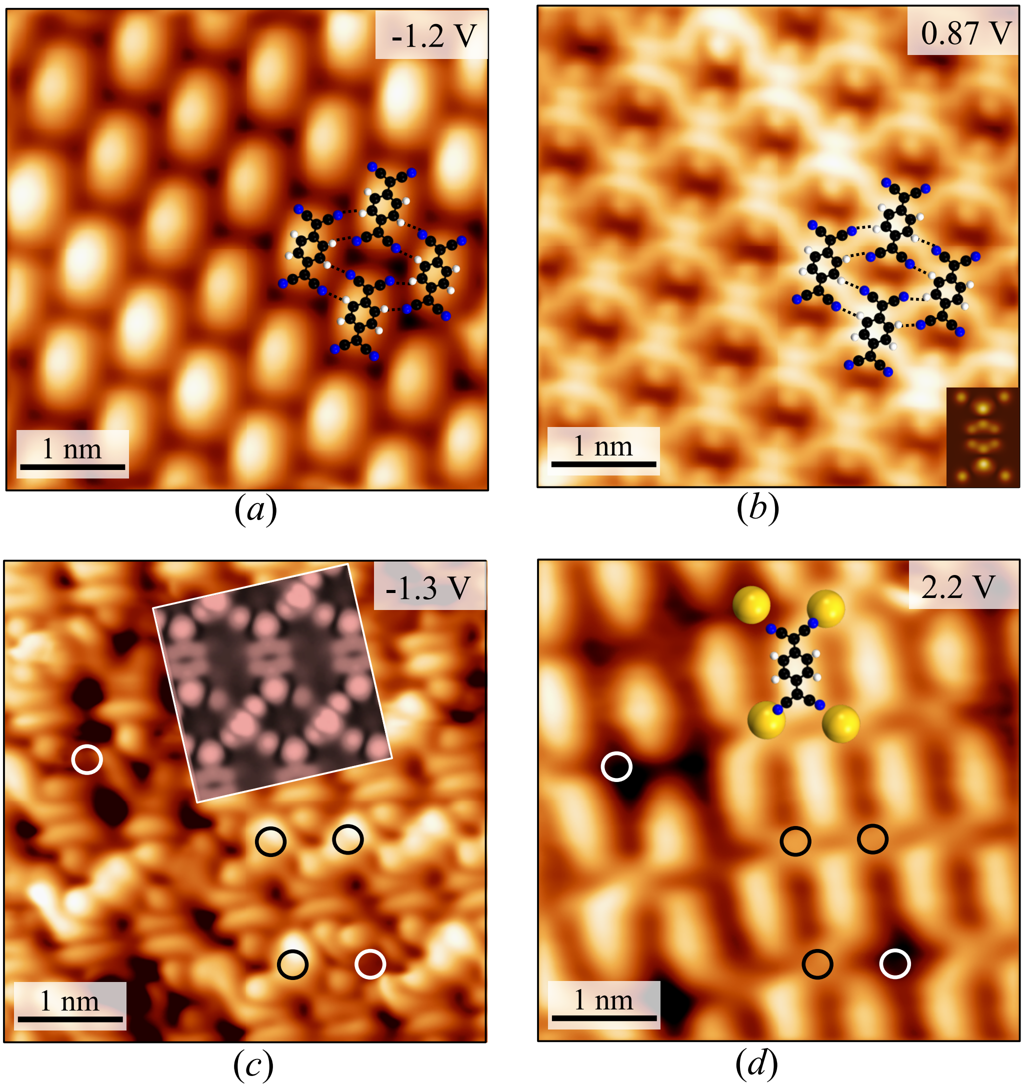

Figure 4.4 STM images of α- (*a* and *b*) and β-TCNQ molecules (*c* and *d*) at negative and positive tunneling voltage. The calculated LUMO isosurface is shown in the inset in (*b*). The H-bond network of α-TCNQ is highlighted in the ball-and-stick models superimposed in (*a*) and (*b*). A simulated STM image and DFT structures are reported in (*c*) and (*d*) for β-TCNQ. Adatoms and adatom vacancies are indicated by black and white circles, respectively.

The round features observed in the interstitial regions included around four cyano moieties (Fig. 4.4 (*c*) and (*d*)) were interpreted as Au atoms incorporated in the molecular network. In fact, the higher density packing of β-TCNQ is not energetically compatible with the occurrence of charging effects, while the formation of an "organic salt" could explain the stabilisation of such a dense, charged structure. Moreover, the presence of defects in the metal-organic assembly allowed us to exclude that the features associated to adatoms were to be rather attributed to electronic effects. The charge transfer to adsorbed molecules was previously reported to produce surface reconstruction, due to lifting or segregation of metal atoms [133]. In particular, F_4-TCNQ deposited on Au(111) was found to accept one electron from the metal and to segregate surface atoms from the herringbone reconstruction [135,137]. These low-coordinated atoms were then included in the molecular self-assembly, whose structure is remarkably similar to the one we observe (Fig. 4.4 (*c*)). In analogy with the cited relevant literature, our results suggest that the formation of the metal-organic β-structures is promoted by the presence of TBP molecules, which allow the donation of electrons from gold to TCNQ.

To further check the consistency of our model, TCNQ alone was deposited on Au(111). The STM experiments gave evidence of the formation of the expected H-bonded α-structures, while, surprisingly, small domains of β-TCNQ were found in proximity of step-edges (Fig. 4.5), contrasting with our picture (*i.e.*, that the presence of donor molecules is necessary to form metal-organic assemblies). Even though β-phases were not reported before in TCNQ/Au(111) systems, the Smoluchowski effect [147,148] could explain their formation, since step-edges are electron-richer than the terrace surface. Therefore, charge transfer from the substrate to TCNQ is favoured and hence occurs in vicinity of step-edges – where the local work function is reduced.

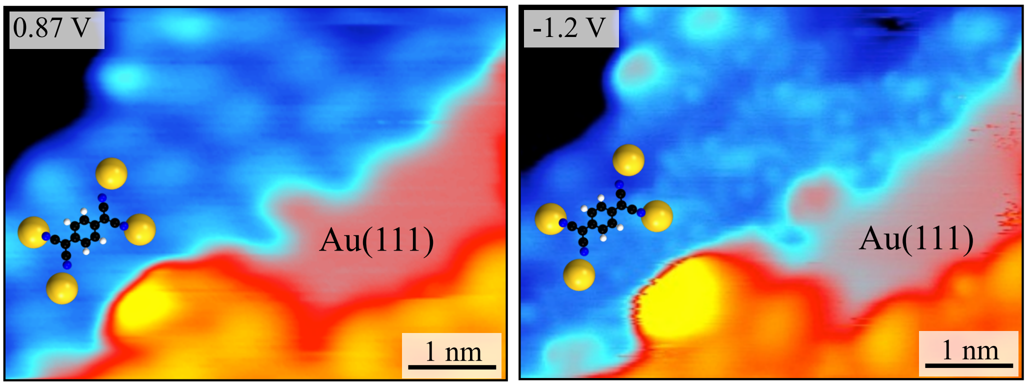

Figure 4.5 Tunneling voltage dependence for β-TCNQ observed near a step-edge at positive and negative bias (left and right), respectively. DFT models are reported as a guide for the eye.

In conclusion, the formation of β-TCNQ metal-organic structures on Au(111) terraces was observed only after codeposition with TBP. Thus, the presence of a donor molecule seems necessary to locally decrease the surface work function and consequently promote the transfer of electrons to TCNQ molecules, which would not be otherwise possible. The formation of β-phases close to step-edges upon deposition of pure TCNQ on Au(111) is related to the Smoluchowski effect, further supporting that the work function reduction on the terraces has to be ascribed to donor TBP molecules.

4.4 Theoretical modelling

This Section is dedicated to the DFT modelling we have performed to rationalise the β-TCNQ assembly. Our aims were to obtain the atomic resolution of the structure and a confirmation of the electronic effects devised from the experimental characterisation. Though we could not disclose the mechanism leading to the formation of the metal-organic complex, our results shed light on the nature of the metal-organic coordination.

4.4.1 *Au/TCNQ organic salt: a DFT model*

DFT geometry optimisation was carried out on the basis of the structural information extracted from the STM images. The unit cell used in our calculation consisted of a four-layered Au slab, with an overlayer comprising one TCNQ molecule plus one Au adatom.

The minimum energy structure for β-TCNQ, shown in Fig. 4.6, is in excellent agreement with our experimental observations. The adatom was found to accommodate in a three-fold hollow site on the Au(111) surface, which did not show any further reconstruction mediated by the adlayer.

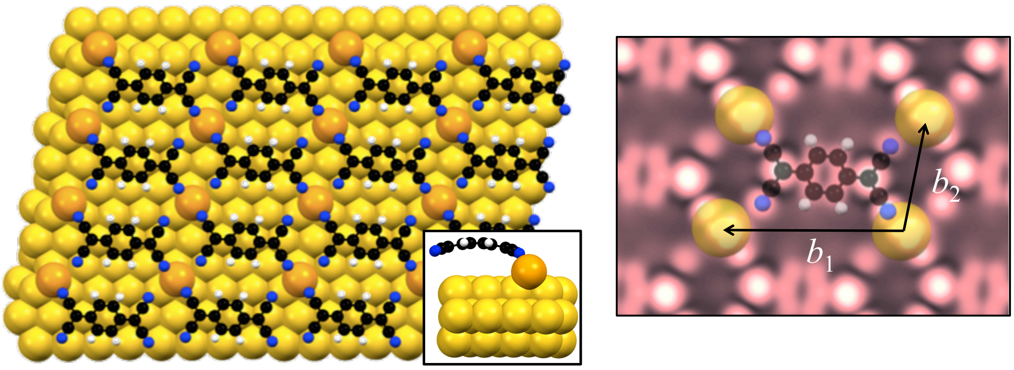

Figure 4.6 *Left*: top view of the DFT-relaxed metal-organic β-TCNQ phase on Au(111). Au adatoms are displayed in orange to easily distinguish them from the surface atoms. The side view of the unit cell is shown in the inset. *Right*: Tersoff-Hamann STM simulation at negative bias (–1.3 V) for the same structure (unit cell vectors are reported for reference).

The dimension of the unit cell are b_1 = 11.97 Å, b_2 = 7.82 Å, θ = 100.9°, to be compared with the experimental measures b_1 = (11.1±0.4) Å, b_2 = (7.3±0.4) Å, θ = (103±3)°. Once more, we note that the calculated structure closely resembles the self-assembly obtained after codeposition of TCNQ and Ni/Mn on Au(111) and Ag(100) or of pure F_4-TCNQ on Au(111) [135,140,141]. Because of the lattice mismatch between the six-fold Au(111) surface and the two-fold rhombic β-adlayer, each TCNQ molecule is directly bound to two diagonal adatoms only, setting the stoichiometry of the organic salt to Au:TCNQ = 1:1. The presence of adatoms is essential for the stabilisation of this structure, which would be otherwise forbidden (see Fig. 4.3 (*b*)) due to electrostatic repulsion between proximal cyano moieties. Adatoms are thus screening the electron-rich cyano residues, by establishing chemical coordination with the two closer nitrogen atoms (Au–N bond length ~2.2 Å, Au–N maximum distance ~3.5 Å). The molecular adsorption conformation is rather bent, with the nitrogen atoms laying about 0.7 Å below the core plane (Fig. 4.6 left). This indicates a strong interaction of the cyano moieties with the Au adatoms, but also the increased flexibility of the molecular backbone, which is associated to charge rearrangement at the metal-organic interface and to the consequent re-aromatisation of the hexagonal carbon core (as reported for TCNQ and other organic molecules [133,134]).

Charge transfer is confirmed from the calculated pDOS of β-TCNQ, shown in Fig. 4.7 together with the gas phase molecular DOS, where the LUMO peak is aligned to the Fermi level – indicating its partial occupation – and the HOMO feature is shifted ~1.1 eV below.

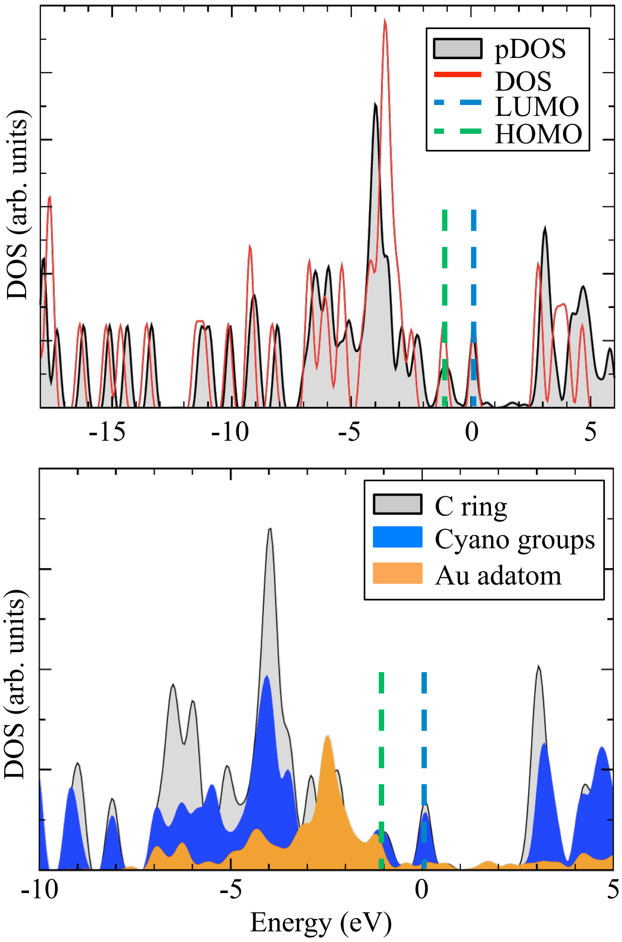

Figure 4.7 *Top*: comparison of the pDOS of β-TCNQ on Au(111) with the DOS of gas phase molecule. *Bottom*: pDOS projected on cyano moieties (blue), core (grey) and Au adatoms (orange). The Fermi level of the metal-organic system is set to zero.

The charge rearrangement at the interface was resolved by plotting the charge density difference $\Delta\rho(\mathbf{r}) = \rho_{tot}(\mathbf{r}) - \rho_{sur}(\mathbf{r}) - \rho_{mol}(\mathbf{r})$, where $\rho_{tot}(\mathbf{r})$, $\rho_{sur}(\mathbf{r})$ and $\rho_{mol}(\mathbf{r})$ are the densities of the full interacting system, the bare metal surface and the gas phase molecule, respectively. The surface plot of $\Delta\rho$ presented in Fig. 4.8 (*a*) shows defined charge depletion from the adatom and correspondent charge accumulation on a molecular region resembling the LUMO of TCNQ.

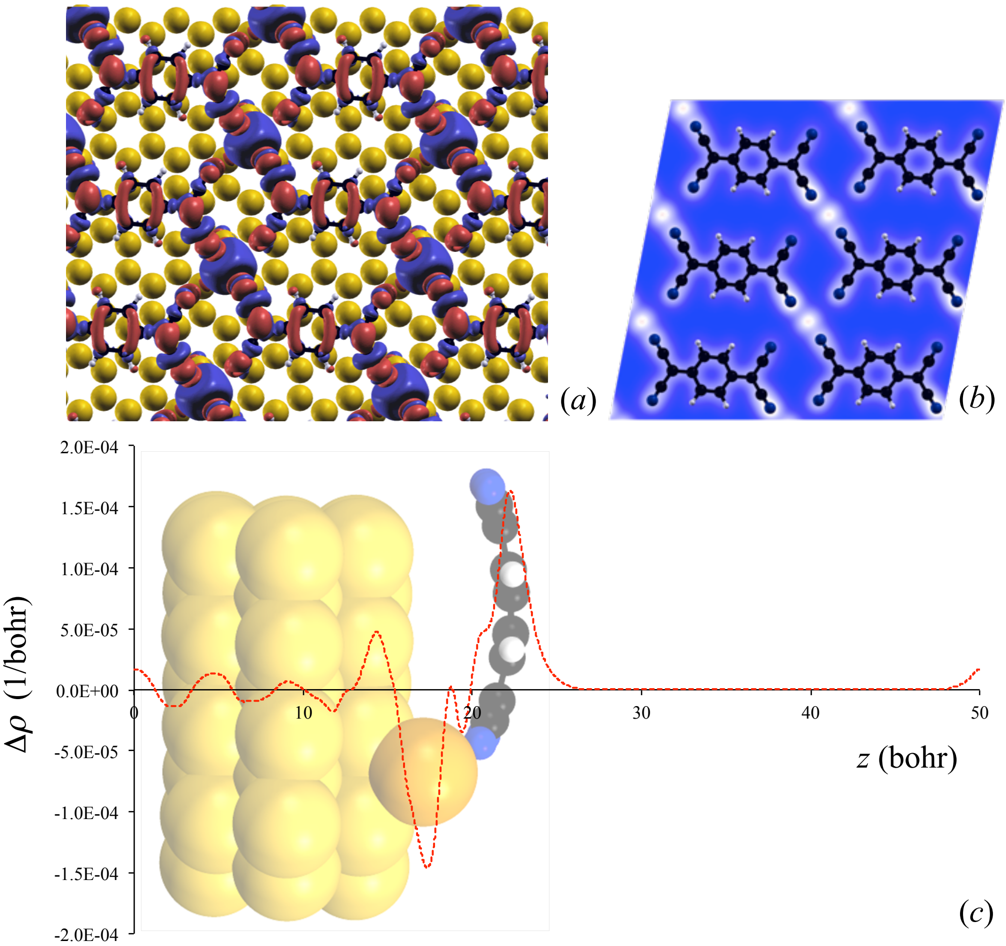

Figure 4.8 *a*) $\Delta\rho(\mathbf{r})$ isosurface (±0.004 bohr^{-1}) for the metal-organic complex. Red and blue regions indicate charge enrichment and depletion respectively. *b*) Total charge density in a plane crossing the Au–N bonds. *c*) $\Delta\rho$ integrated on x-y planes versus the direction normal to the surface (z). Positive values indicate charge accumulation.

A more detailed depiction of the charge migration was obtained by plotting the differential electron energy $\Delta\rho$ integrated over the x-y plane, along the z coordinate of the unit cell (Fig. 4.8 (*c*)). Consistently with what observed in Fig. 4.8 (*a*), the Au adatom shows a clear loss of electron density, which appears to be totally transferred to the molecule. The only effect evidenced in the metal is a minor charge accumulation directly under the adatom – most likely due to a screening rearrangement in the slab, with the three bottom layers not being perturbed by the charge transfer process. The amount of charge transferred to TCNQ molecules was estimated on the basis of a Bader topological analysis of the system's charge density $\rho_{tot}(\mathbf{r})$ [149], from which we calculated a net transfer of 0.54 *e*/molecule (0.46 *e* are directly ascribed to the Au adatom).

The DOS projected on the nitrile moieties and the molecular core separately, together with the pDOS of the Au adatom, are reported in Fig. 4.7 (bottom) for a better understanding of the chemical nature of the metal-organic interaction. In particular, the pDOS of the Au adatom shows some spectral weight at −1.2 eV, corresponding to the molecular peaks associated to HOMO for both the pDOS of the cyano and TCNQ core. These observations suggest a covalent character of the Au–TCNQ bonds (as expected in case of coordination with a transition metal [139]), which is further evidenced by the presence of charge density in the Au–N space gap (Fig. 4.8 (*b*)). Moreover, the STM simulations calculated at a bias voltage of −1.3 V (accordingly to the Tersoff-Hamman approach [86], Fig. 4.6 right) resembles well the experimental images obtained at the same voltage. In fact, the bright features appearing in correspondence to the molecules closely match their LUMO shape, with the signal being stronger on the cyano residues. The cyano groups bound to the adatoms have a brighter rendering than the other two, which reflects the diagonal coordination and also well matches the experimental observations. Finally, Au adatoms appears as additional protrusions included between four neighbouring cyano residues, confirming the attribution given to the corresponding features observed in the STM images.

4.5 *I*(*V*) spectroscopy

The local electronic structure of α- and β-TCNQ phases was probed by means of STS spectroscopy to experimentally investigate charge transfer effects. The *I*(*V*) spectra recorded on α molecules displays the typical features associated to neutral TCNQ (Fig. 4.9 (*a*)) [144]. In particular, the broad peak in the positive energy region (~0.7 eV) is associated to the LUMO level, while the slight shift of the Au(111) surface state can be attributed to the pillow effect and is consistent with weak metal-molecule interactions. The HOMO peak was not observed in the investigated bias voltage range, which is ascribed to the rather large HOMO-LUMO gap (~3.1 eV for TCNQ on Au(111) [145]).

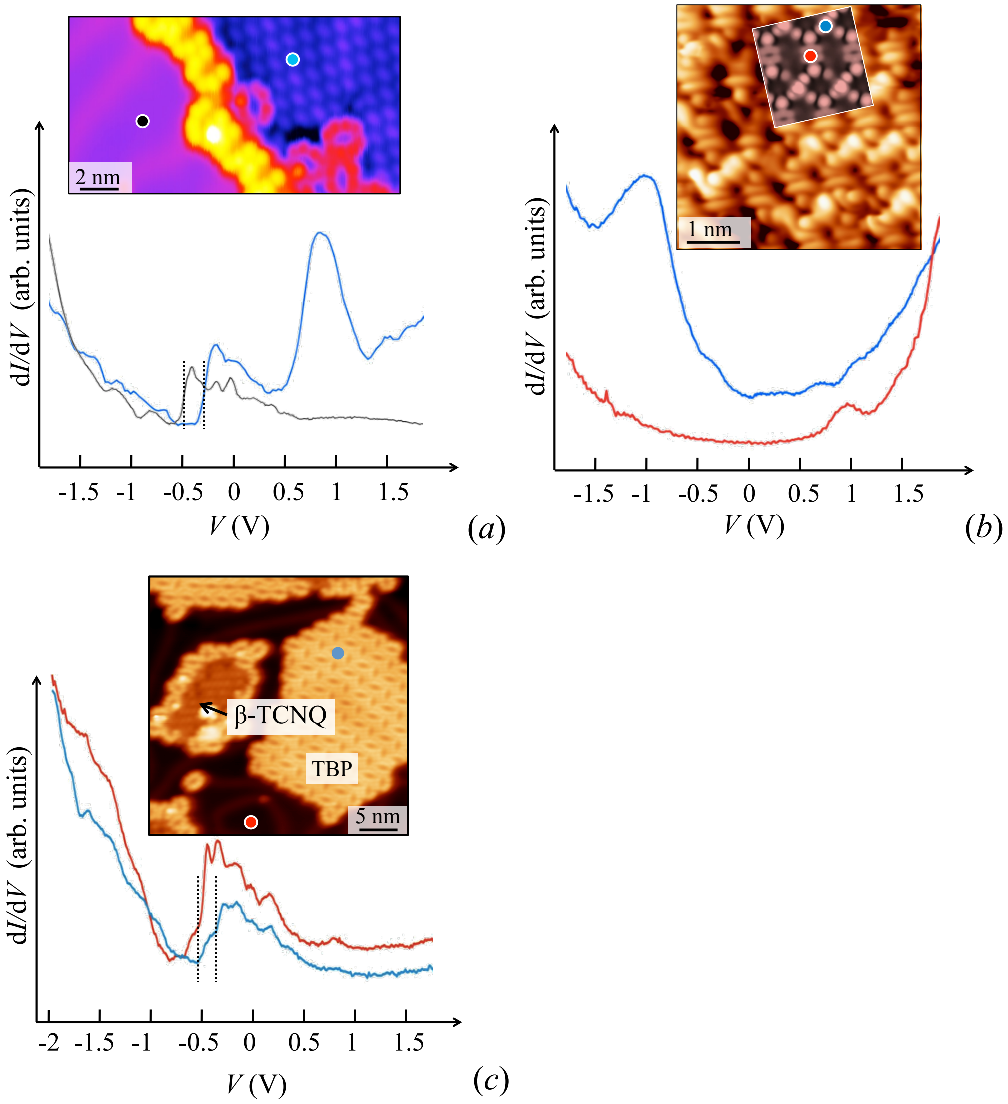

Figure 4.9 *I*(*V*) spectra measured on α- (*a*), β-TCNQ (*b*) and TBP molecules (*c*). In the insets, filled circles indicate the point where the spectrum was acquired (the same colour code applies in the graphs). The Au(111) spectra are shown in (*a*) and (*c*) for reference (black and red colour, respectively).

On the other hand, a substantially different d*I*/d*V* spectrum was measured on top of β-TCNQ molecules (Fig. 4.9 (*b*)). In fact, the Au(111) surface state disappeared, suggesting a significant charge rearrangement at the metal-organic interface, while the spectral features recorded on different molecular positions showed different characteristics. For instance, the d*I*/d*V* profile measured in correspondence of the cyano moieties shows a broad peak at ~ −1.1 eV (Fig. 4.9 (*b*), blue curve), which we associate to the formation of a metal-organic state from the hybridisation between the molecular LUMO and Au adatom states. This picture allows to rationalise the position of the −1.1 eV peak on the cyano-Au adatom sites and is further supported by the fact that both the experimental and simulated STM images at negative bias (*i.e.*, the occupied states region) resemble the LUMO orbital of TCNQ plus some contribution from adatoms (cf. Fig. 4.4 (*c*) and 4.6). The d*I*/d*V* spectrum measured on the TCNQ core only shows a small peak at ~0.8 eV, which we associate to the LUMO+1 resonance (Fig. 4.9 (*b*), red curve).

For completeness, STS experiments were performed also for codeposited TBP molecules (Fig. 4.9 (*c*)). While the collection of d*I*/d*V* spectra was not possible for TBP molecules located at the border of β-TCNQ (because of tip-induced rotations), the measurements were carried out on homomolecular TBP islands close to β-TCNQ formations. No molecular features were observed in the chosen bias voltage range, where only the Au(111) surface state is present with a slight shift ((140±10) meV) induced by the pillow effect [136,137,144].

4.6 Two dipoles in action: Monte Carlo simulations

Our combined experimental and theoretical analysis allowed us to demonstrate that TCNQ undergoes charge transfer on Au(111) in the presence of a donor molecule (TBP), with the formation of an organic salt arranged in β-islands decorated by rims of TBP. However, the codeposition of donor and acceptor molecules was reported to promote the formation of ordered self-assemblies, *e.g.*, by alternating the two species in homomolecular rows [150].

To rationalise the peculiar self-assembly associated to the presence of β-TCNQ phases, we implemented a Monte Carlo model very similar to the one introduced in Chapter 3. The main difference here is that we are dealing with a bicomponent system, which we reproduced by fixing the concentration of TCNQ and then “fluxing” some TBP-like particles in the system (by setting the system in chemical equilibrium with an infinite reservoir, in agreement with the grand canonical description). The model Hamiltonian was formulated in analogy with the one used in Chapter 3, *i.e.*, considering nearest neighbours van der Waals attraction and a long-range dipolar field to account for electrostatic repulsion. Since the system is now bicomponent, parameterisation was necessary not only for mono-species interactions (already defined for TBP-TBP pairs), but also for cross-species interactions. The "strong" TCNQ-TCNQ short-range attraction was tentatively set to twice the value used for TBP-TBP (owing to the stronger interactions deriving from H-bonds or salt-induced stabilisation), while the "weak" TBP-TCNQ cross attraction was fixed to the half of TBP-TBP van der Waals coupling (due to the very different chemical nature and adsorption configuration of the two molecules). Ultimately, TBP/TCNQ molecules were associated to positive/negative charge transfer dipoles perpendicular to the surface plane (consistent with charge donation/injection). The magnitude of the anionic TCNQ dipole was set to half of the cationic TBP one, due to the reduced dipole length (vertical distance) for the TCNQ-Au adatom couple.

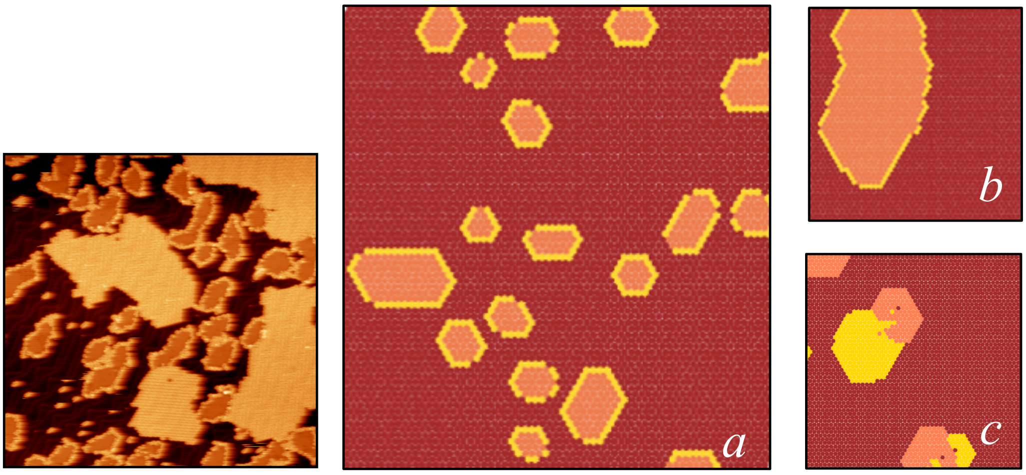

Figure 4.10 Snapshots of Monte Carlo simulations modelling the codeposition of TBP (yellow) and TCNQ (pink). Phase segregation is always observed but different equilibrium distributions are obtained depending on the state of charge of the components (in *a* both TBP and TCNQ are charged, in *b* only TBP, while in *c* both molecules are neutral).

Remarkably, the equilibrium structures produced by our Monte Carlo model showed good qualitative agreement with the experimental observations in the relevant TCNQ:TBP = 3:1 stoichiometry (Fig. 4.10 (*a*)). A very different situation was instead obtained when simulating neutral TCNQ. In this case, the predicted equilibrium structure was a single TCNQ island framed by the still charged TBP molecules (Fig. 4.10 (*b*)), which suggests that the distribution of small β-TCNQ aggregates is driven by electrostatic repulsion. Finally, our model invariably predicts the formation of homomolecular aggregates when both species are neutral (Fig. 4.10 (*c*)). Phase segregation was the expected outcome due to the unfavourable van der Waals TBP-TCNQ mixing; however, the opposite dipoles carried by the two species make the formation of a one-molecule-thick TBP frame around TCNQ islands energetically convenient. In our Monte Carlo simulations, this assembly allows to maximise the high "β-TCNQ cohesive energy", while the TBP-TBP repulsion results screened by the proximity of an opposite dipole.

Although very simplified, we believe that this model captures the behaviour of binary systems, where the components are carriers of opposite charges. Our aim was not to reach a detailed explanation of the complex process leading to mutually induced charge transfer and the consequent formation of an organic salt, but rather to give a qualitative description of the observed assembly. Indeed, our model further confirms that the formation of β-TCNQ islands decorated by a rim of TBP molecules requires both molecules to carry a dipole, whose sign is the result of the charge transfer direction with respect to the metal substrate.

4.7 Conclusions

In this Chapter the supramolecular self-assembly of codeposited TBP and TCNQ molecules on Au(111) was characterised by means of STM techniques and theoretical modelling.

The self-assembly showed a well-defined phase segregation behaviour, where both species have the tendency to form homomolecular domains. However, TCNQ was found to follow two different organisation patterns: the first producing an extended H-bond coordinated network (α-phase, already observed after deposition of TCNQ alone), the second being characterised by the formation of islands decorated by a rim of TBP molecules (β-phase).

We demonstrated how the formation of the latter structure could only be explained if both TBP and TCNQ are subjected to charge transfer from and to the surface, respectively. In other words, the presence of TBP molecules was found necessary to enable the otherwise forbidden charge transfer from Au(111) to TCNQ, which constitutes an indirect (and further) confirmation of the donor nature of TBP. Here, uncommonly enough, the source of charge migration was not related to intermolecular charge transfer occurring between donor/acceptor couples [150,151], but was rather originated from a surface-mediated charge transfer. This means that the charge transfer from TBP donor molecules locally decreases the surface work function, allowing TCNQ to oxidise the Au(111) surface. In addition, we also demonstrated the formation of TCNQ-Au organic salt upon segregation of Au adatom in the molecular assembly, as confirmed by STM experiments and DFT calculations and consistently with previous findings. We note that the observation of unexpected self-assembly patterns can be actually interpreted as a first indication of charge transfer at the metal-organic interface, as for the anomalous coarsening of TBP discussed in Chapter 3.

Chapter 5

Organic substituted borazines: “Magic” clustering after surface mediated deprotonation

The design of novel molecular building blocks is the baseline for the fabrication – via self-assembly – of nanostructured materials with selected properties and functionalities. This evolutionary approach has emerged only in the last couple of decades, when the introduction of STM microscopy allowed to atomically resolving the organisational behaviour of molecules adsorbed on various substrates. However, this hardly represents a novelty, since the design and production of “self-assembling bricks” is routinely performed in many biological processes [2], where the levels of complexity reached are still hardly understood. Learning from nature, the variety of covalent bonds that carbon atoms can shape allows for the realization of molecular structures with very different chemical and physical properties. In particular, the addition of heteroatoms or heterogroups to hydrocarbon-based architectures is the most effective way to add specific functionalities to a single molecule and – subsequently – to promote the formation of well defined supramolecular structures, driven by highly directional intermolecular interactions.

In this Chapter we will present for the first time the bottom up fabrication of borazine-doped nanostructures on metallic surfaces and their joint theoretical and experimental characterization. Here, the molecular building blocks are organic-substituted borazine molecules, in which the addition of a hydroxyl moiety allows for deprotonation on the reactive Cu(111) substrate. The electrostatic repulsive interactions following deprotonation are responsible for the self-assembly into small “magic” clusters of 7, 10, 11, 12, and 13 monomers, in contrast with the large close-packed islands we observe for not-acidic borazine molecules.

The experimental picture has been rationalised by our *ad hoc* kinetic Monte Carlo model, which shows that the observed supramolecular organization can be explained only in terms of a fine balance between van der Waals and electrostatic interactions. This delicate, yet robust equilibrium of forces pushes the extent of the self-organisation beyond the nearest neighbour length scale.

The study presented here is the result of the collaboration with Dr Simon Kervyn, Jonathan Tasseroul, Prof Davide Bonifazi (who prepared and applied the protocols for the chemical synthesis of the molecules, Université de Namur), Dr Nataliya Kalashnyk, Ben Moreton and Prof Giovanni Costantini (acknowledged for the STM characterization of the metal-organic system, University of Warwick) and has been partly presented in a recently published paper [152].

5.1 Borazine and boron nitride as heterogroups in hydrocarbons

Carbon chemistry constitutes the natural playground for the development of novel chemicals, which can be tailored – with virtually no limits – to display selected structural, electronic or other physical properties. Among the many carbon-based allotropes and compounds, polyaromatic hydrocarbons are of particular importance because of their excellent conductivity and interesting optical properties. These characteristics are particularly valuable in the field of organic optoelectronics, where the availability of new π-electronic materials is fundamental for the efficient realisation of devices like organic light emitting diodes (OLEDs) and organic field effect transistors (OFETs) [8,41,131,132]. To this aim, polyaromatic hydrocarbons have been functionalised with hydrophilic or electron donor/acceptor groups in order to adjust their solubility, solid-state packing and electronic properties.

Recently, the substitution of carbon-carbon sp^2 couples (C=C) with isoelectronic heteroatom pairs has emerged as an effective doping strategy, opening up the possibility of tuning both electronic and mechanical properties of polycyclic hydrocarbons. For instance, C=C units can be replaced with boron nitride (BN) pairs to give isostructural and isoelectronic molecules bearing strong intrinsic dipoles and displaying larger HOMO-LUMO gaps, with consequently different photophysical properties [153,154].

Boron nitride is found to form all of carbon polymorphs in the solid state (*e.g.*, graphite-like α-BN, tetrahedral diamond-like β-BN and wurtzite, BN-nanotubes) and it has also very similar mechanical properties. On the other hand, the large electronegativity difference between boron and nitrogen reduces the covalent character of their bond, which translates into a dramatic reduction of α-BN conductivity, as revealed by its large band gap energy located in the UV region. For this reason, the BN benzene counterpart, known as borazine ($B_3N_3H_6$, Fig. 5.1) [155], is being considered with its oligomers as a suitable building block for BN-ceramics, thin-film insulators, LEDs and lasing mediums for UV-lasers [156,154,157,158].

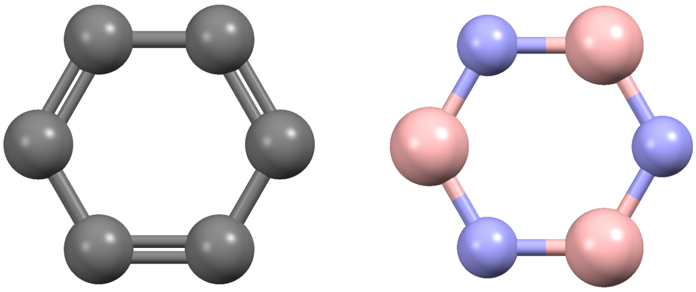

Figure 5.1 Benzene (right) and its isostructural/isoelectronic inorganic equivalent borazine (left).

However, the high susceptibility of the B–N bond to hydrolysis has considerably hampered the development of borazine-based devices. In order to overcome this issue, we have designed hydrolysis-resistant borazines which are promising UV-emitting materials for application in optically active layers [159]. The unprecedented stability of this novel class of hybrid BN compounds is ascribed to their functionalisation with bulky aromatic moieties, which are able to screen the B–N bonds from incoming water molecules. Moreover, the organic substitution leads to unique crystallisation patterns, owing to spatial proximity and intermolecular interactions between the π conjugated moieties in the molecular solid [160]. Similar effects, *i.e.* molecular recognition driven by π stacking, are expected to occur also in the two-dimensional self-assembly of hybrid BN-organic molecules on metal surfaces, which is the object of the study presented here. Although mostly unexplored, the analysis of the self-organisation of borazine layers could help understand and engineer new functional materials.

5.2 Synthesis of hybrid BN-organic molecules

While showing desirable optical properties, borazine was also proven to act as a flexible molecular hub, since two different moieties could be selectively attached to boron or nitrogen atoms [160].

We present here a brief description of the synthetic protocols developed by Dr Simon Kervyn and Jonathan Tasseroul (Université de Namur) for the production of the borazine derivatives used in this work, which is functional to introducing their structure and nomenclature. The synthesis is conducted following a simple one-pot procedure, where the reaction of boron chloride (BCl_3) with aminobenzene (aniline) yields B-trichloro-N-triphenylborazine. The product can be treated afterwards with alkaline-derivative of mesitylene (1,3,5-trimethylbenzene) to give B-trimesityl-N-triphenylborazine, here identified for simplicity with the index **1** (cf. Scheme 1 below; we will refer to this molecule throughout the discussion either as molecule **1** or borazine **1**).

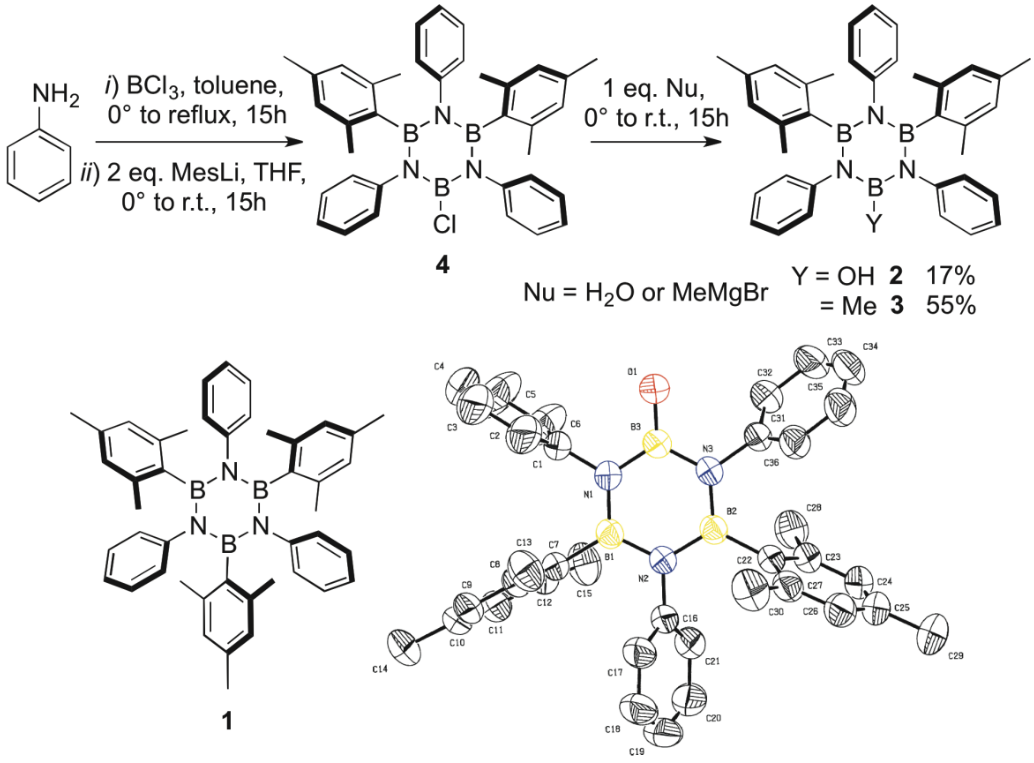

Scheme 1 *Top*: protocol for the synthesis of hydroxyl- and methyl- borazines **2** and **3**. *Bottom*: chemical structure of trimesityl-borazine **1** (left) and X-ray diffraction molecular configuration of **2** (right) (colour code: blue N, red O, yellow B, grey C). Courtesy of Dr S. Kervyn.

Molecule **1** has shown exceptional stability to hydrolysis in water solution, due to sterical screening of the mesityl (Mes) groups. In fact, X-ray structure analysis revealed a quasi-perpendicular arrangement of the aryl moieties that constrains the *ortho*-methyl groups on top of the boron atoms, effectively preventing possible nucleophilic reactions with water (Fig. 2). Furthermore, borazine **1** was found to display radiative emission with spectral features below 300 nm (*i.e.*, conserving the UV-emitting properties of pure hexagonal BN), which makes this molecule a candidate active material for the fabrication of electroluminescent layers [159].

Asymmetric borazine derivatives, bearing single hydroxyl (–OH) moieties, were synthesised to investigate the effect of an added acidic character upon deposition on a relatively reactive metal surfaces. In a similar manner to the experimental protocol for the synthesis of molecule **1**, the hydroxyl borazine **2** derivative was obtained upon reaction of boron chloride with aniline and successive addition of two molar equivalents of alkaline-Mes and water (MesLi, see Scheme 1). An asymmetric non-acidic borazine (identified by the index **3**) was also synthesised to serve as a test molecule in comparative metal deposition experiments, where the B–OH terminal of **2** was replaced by a methyl (B–CH_3).

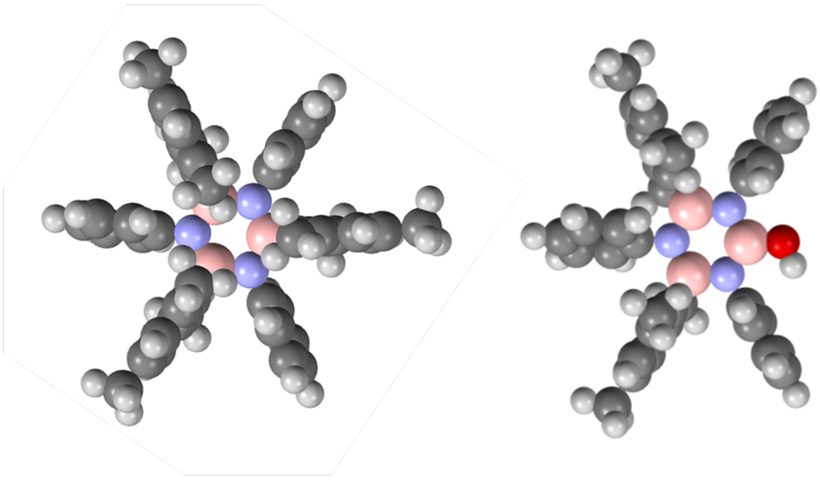

Figure 5.2 Spacefill atomic models of borazine **1** (left) and **2** (right) with colour code: light grey H, grey C, pink B, light blue N, red O.

5.3 STM analysis of borazine 1 deposited on Cu(111)

We show here the results of the STM characterization of the system borazine **1**/Cu(111) conducted by Dr Nataliya Kalashnyk (University of Warwick). The nanostructures obtained upon room temperature deposition will be further studied by means of classical molecular dynamics. A detailed description of the experimental procedure and of the theoretical modelling will be provided before the respective discussions.

The experiments were carried out using a commercial low temperature STM equipment (Createc) under ultra high vacuum conditions (typical base pressure of the STM chamber of 4×10^{-11} mbar). The clean Cu(111) surface was prepared via repeated Ar^+ sputtering cycles and successive annealing at 870 K. Before deposition, the molecules (in the form of crystal powder) where fully degassed under high vacuum. The deposition on the Cu(111) crystal was obtained from thermal sublimation by molecular beam epitaxy (using a Knudesen cell evaporator). The metal substrate was maintained at 300 K during the deposition and then quenched to 77 K for the imaging process. All the measurements were obtained with chemically etched tungsten tip in the constant current mode (typical values for the tip/sample bias $V = 1.8$ V and for the tunneling current $I = 4\times10^{-11}$ A).

The deposition of borazine **1** reveals the formation of highly ordered islands for any sub-monolayer coverage (Fig. 5.3). Each single monomer appears like a group of three bright bulges arranged in a slightly distorted triangular shape, where each blob is attributed to a Mes group [161,162], which are bulkier and richer in electrons. The collective tiling pattern of the triangular features generates rows in which each unit is flipped upwards or downwards with respect to the neighbouring one (cf. Fig. 5.3 right) and adjacent rows are related by a C_2 rotation.

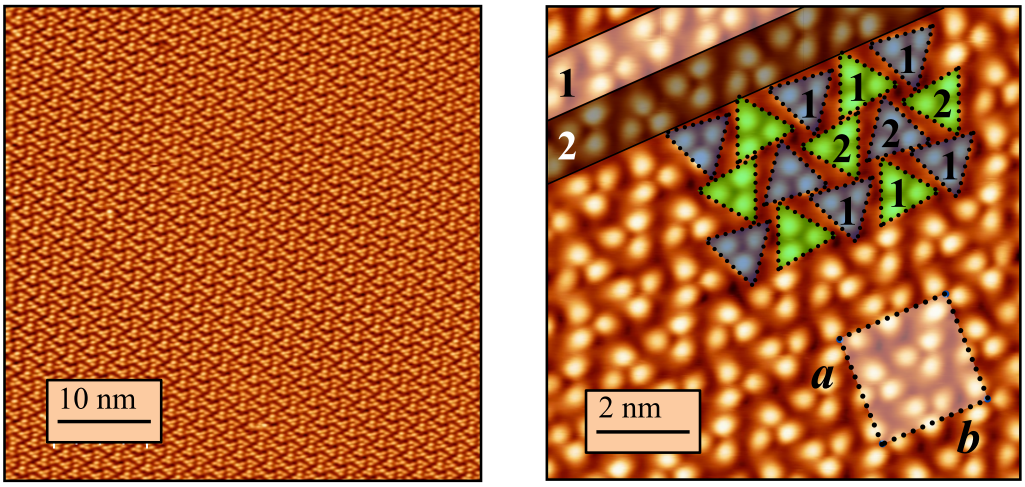

Figure 5.3 *Left panel*: high resolution STM topography of borazine **1** deposited on Cu(111) reveals its highly ordered self-assembly. *Right panel*: close-up view of the layer structure where the single molecules are indicated by up- (green) or down-flipped (grey) triangles arranged in rows. The unit cell of the assembly is shown in the bottom-right corner.

The resulting unit cell contains four molecules arranged in a quasi-square geometry (a = 23.8 Å, b = 24.3 Å), which bears no registry with the three-fold symmetric (111) transition metal surface. This suggests a supramolecular organisation primarily driven by intermolecular interactions.

5.4 Molecular dynamics model for adsorbed borazine 1

The inherent complexity of metal-organic systems requires a detailed description at the atomistic level in order to understand the processes involved in the self-assembly mechanisms. The necessary information can only be obtained by combining experimental and theoretical tools.

To this aim, molecular dynamics calculations were carried out to achieve a better resolution of the self-assembling motif of borazine **1**, primarily by determining the adsorption conformation and by atomically resolving the intermolecular interactions network. Experiments and theory will be integrated to obtain a comprehensive description of the system.

5.4.1 *Technical details*

Classical molecular dynamics simulations were carried out with the LAMMPS package [105], using the Universal Force-Field (UFF) to model the geometry and the intermolecular interactions of organic-substituted borazine **1** [163].

Interactions at the metal-organic interface were modelled accordingly to a semiempirical force-field fitted from desorption experiments and MP2 calculations of simple hydrocarbons adsorbed on Au(111) [69]. This force-field parameterisation was assumed to remain valid also for the Cu(111) surface, since adsorption energies of π-conjugated hydrocarbons – *e.g.*, ethylene and benzene – on Cu(111) [107] and Au(111) surfaces [18] are nearly equivalent. Structural relaxation of the metal substrate was assumed to have negligible effect on the molecular self-assembly [109], hence, the position of the metal atoms was kept frozen by setting all their force components to zero.

B-metal and N-metal interactions were accounted for by a single set of Lennard-Jones parameters, which was enough to reach excellent agreement between the simulated structures and the experimental ones (cf. *e.g.*, Fig. 5.4 and 5.5). All calculations were carried out in the canonical ensemble, the temperature control being set with a Langevin thermostat. Particle mesh Ewald was used to compute long-range electrostatic interactions based on a 1 Å mesh, and the cutoff for non-bonded terms was set to 10 Å. The Newton equation of motion was integrated with the Verlet algorithm [64].

5.4.2 *Modelling a borazine **1** layer*

The steric hindrance between the lateral substituents of molecule **1** turns out not only to prevent hydrolysis of the B–N bonds (by screening incoming water molecules), but also to decouple the borazine ring from the substrate. In fact, the spatial congestion prevents any rotation of the aryl and mesityl groups, which are constrained to lay perpendicular to the surface.

The configuration of the adsorbate was determined by molecular dynamics simulation of a single adsorbed molecule. This has shown that the mesityl groups are operating as a "tripod" lifting the borazine core ~5 Å above (and parallel) to the Cu(111) surface. Moreover, the calculated distance of 6 Å between the benzene rings of the mesityl groups well matches the one measured between the centres of the three bright bulges associated to a monomer in the STM images (Fig. 5.4).

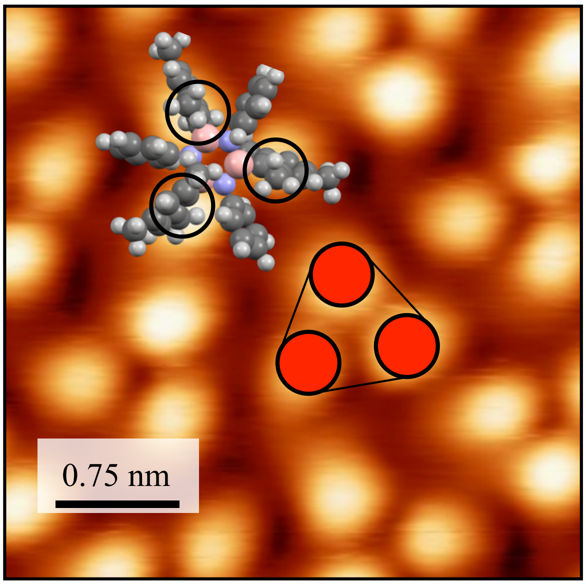

Figure 5.4 Atomistic and schematic models for molecule **1** superimposed on a STM close-up image. The three bright spots constituting a molecule are clearly assigned to the mesityl groups (black circles) in the spacefill all-atom model.

It is worth noting that the absence of reactive heterogroups (*e.g.*, carboxyl [164], nitrile [165]) that would be able to strongly interact with the metal, together with the smoothness of the potential energy surface of Cu(111) [96] allow for the high mobility of the adsorbates even at low temperature (~10^{-9} m^2/s at 77 K, as estimated by our classical model). This result is supported by our STM experiments, where isolated monomers are never observed, indicating that the hopping between degenerate adsorption sites is highly activated even at the liquid nitrogen temperature. Following these observations, we can conclude that the substrate is playing a negligible role on the self-assembly of borazine **1**, which instead arises most likely from van der Waals attractive forces.

In order to investigate the morphology of the observed close-packed self-assembled layer, a molecular island composed of 36 borazine **1** units was positioned on top of a four layer metal slab yielding a (28.8×28.8 nm^2) surface unit cell, periodically repeated. The initial configuration of this larger structure was obtained by observing the coordination mechanisms of smaller clusters (from dimers to hexamers) and by extending their basic principles to larger aggregates. The system dynamics was computed for 2 ns at 250 K (to allow for structural relaxation), followed by slow cooling and equilibration at 77 K (8 ns), resulting in an equilibrium configuration that nicely reproduces the features observed in our STM topographies (Fig. 5.5, right).

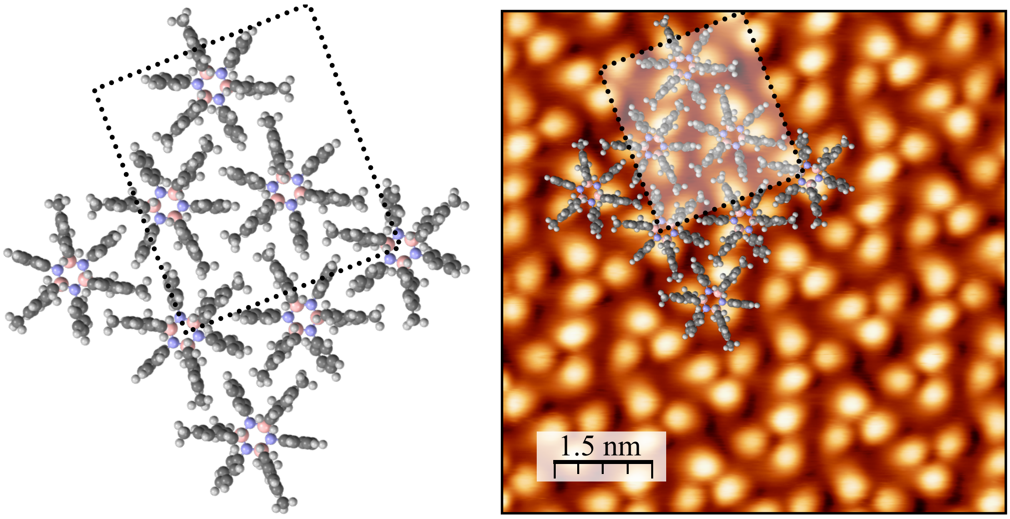

Figure 5.5 Calculated structure (left) and its superimposition on the experimental borazine **1** monolayer (right, the shaded rectangle corresponding to the experimental unit cell). The molecules are strongly interdigitated owing to π-π stacking interactions.

Having a closer look at Fig. 5.5, it is clearly visible that mesityl and phenyl groups of neighbouring molecules are strongly interdigitated, producing a gear bearing-like structure. This distinctive self-assembly is the result of molecular structure-directed growth (*i.e.*, driven by molecular recognition) resulting in a regular network of offset-parallel π stacking interactions [160], with an average π-π distance of 3.50 Å. The observed self-organization is a direct consequence of the C_3 symmetry of molecule **1** and gives an estimated energy gain of roughly 0.10 eV for each intermolecular contact.

5.5 Borazine 2 on Cu(111)

In a second set of experiments, borazine **2** was deposited on the Cu(111) surface under the same operative conditions adopted for molecule **1**.

At variance with the faultless two-dimensional crystals obtained from the deposition of molecule **1**, hydroxyl-borazine **2** self-organises into a variety of small clusters, in which the single molecule appears like two aligned bright bulges. These aggregates are imaged in the STM topographies as recurrent and well-defined structures, even though they do not always show regular geometries and can thus be considered as different isomers.

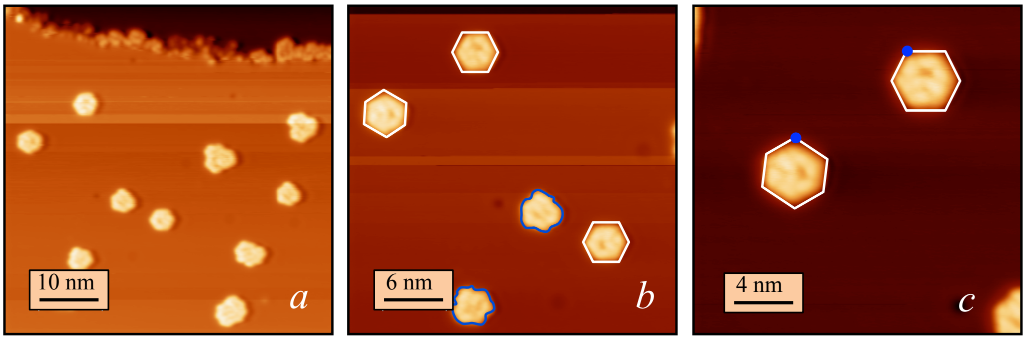

Figure 5.6 Isolated clusters of borazine **2** observed at low molecular coverage. The perfect hexagonal geometry of regular heptamers is highlighted in panels *b* and *c*.

The only exception to the above is observed in the smallest and most frequently observed cluster, which is always composed by a central monomer surrounded by six neighbours (heptamer or 7-mer) arranged in a tight hexagonal structure. The dark spot appearing slightly off the centre of the regular 7-mer shows that the cluster fine structure is preserved upon rotation, thus, all the observed hexagonal clusters are not different isomers but the same kind of aggregate (cf. Fig. 5.6 (*c*)).

The observed clusters sizes range from a minimum of 7 to a maximum of 25 molecular units and they are substantially unaffected by an increase in the coverage up to 0.3 ML, indicating that the usual Ostwald ripening [112] does not occur for borazine **2** (*i.e.*, small structures are not succumbing in favour of larger ones, Fig. 5.7).

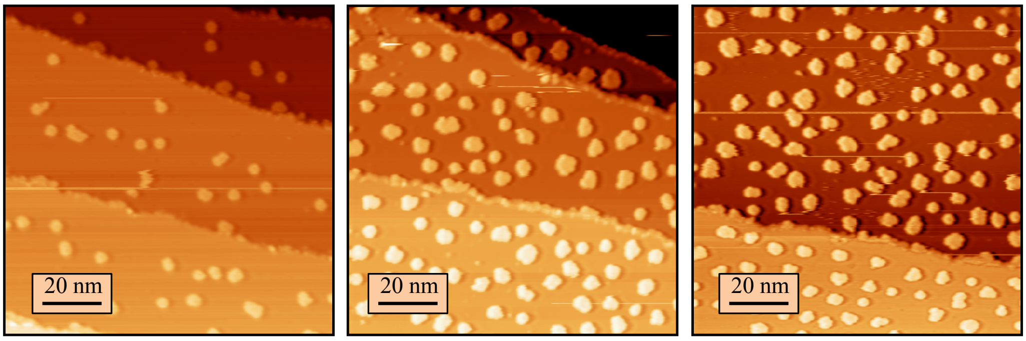

Figure 5.7 Series of STM images for increasing molecular coverage (from left to right) showing no coarsening of borazine **2** clusters.

5.5.1 *Atomistic model*

Since individual molecules are never observed, the self-assembly of molecule **2** in sparse aggregates is not expected to arise from limited mobility caused by chemisorption (*i.e.*, kinetically hindered growth). Nevertheless, copper is known to establish coordination bonds with carboxyl moieties and one might expect to observe similar interactions with hydroxyl groups [164,166]. In order to exclude that chemisorption could be at the origin of the molecular clusters, we studied the adsorption of borazine **2** by means of DFT with the aim of resolving the metal/molecule binding mode.

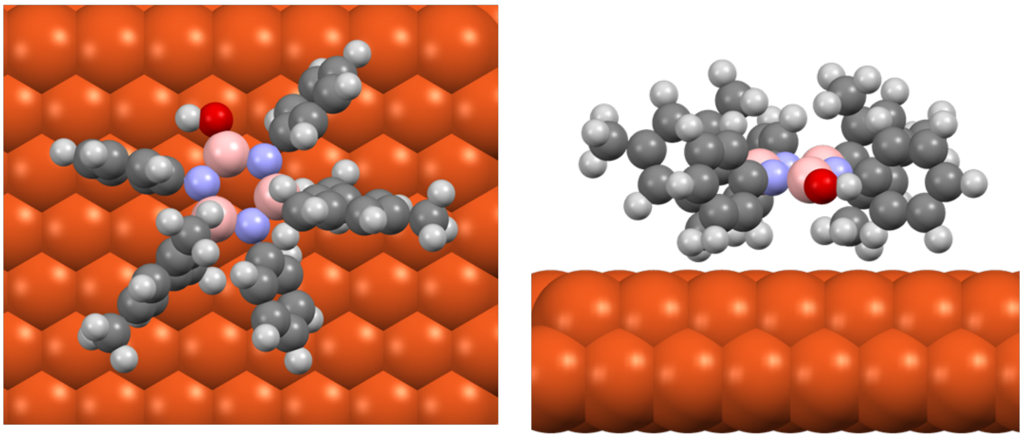

Figure 5.8 VdW-DF equilibrium energy structure of a single adsorbed hydroxyl-borazine **2** (*left*: top view, *right*: side). The bulky aryl moieties are effectively confining the borazine core and the OH group well above the Cu(111) surface.

The quantum mechanical modelling was implemented at the DFT level with the plane-wave package Quantum ESPRESSO [99]. The calculations were performed using ultrasoft pseudopotentials [79] and the PBE-GGA exchange-correlation [100] within the non-local vdW-DF formalism [74]. The kinetic energy cutoff for the wavefunctions and the electron density was set to 0.41 and 4.1 keV, respectively. The structure of the metal-organic system was relaxed until all the atomic forces components were less than 0.10 eV/Å, with the copper surface being modelled by a three-layer slab (equivalent to a 12×12 supercell). The Brillouin zone was integrated over a 3×3×1 Monkhorst-Pack grid. The size of the orthorhombic unit cell was sufficient to allow 10 Å vacuum between periodic replicas and the Bengtsson dipole correction was applied [102,103] to correct for the non-periodicity of the slab geometry.

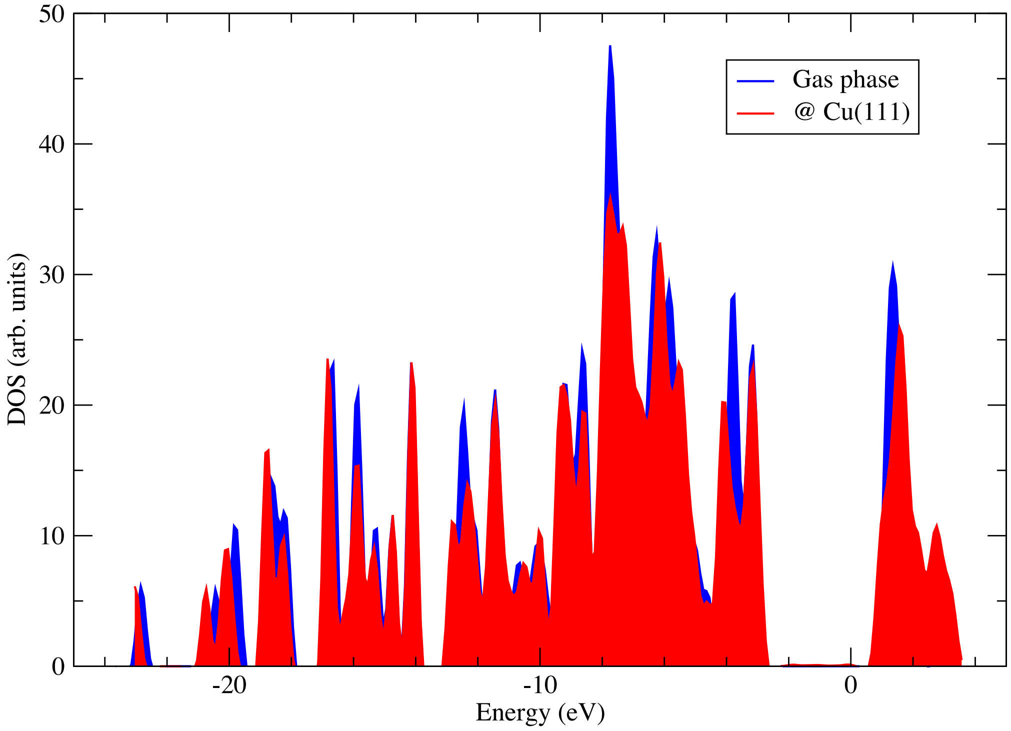

Figure 5.9 pDOS of the isolated adsorbed borazine **2** (red fill) compared to the total DOS of the molecule in gas phase (blue), where the Fermi energy of the metal-organic system was set as the origin. The frontier molecular orbitals show no significantly modifications upon adsorption.

The calculated adsorption equilibrium configuration of molecule **2** reveals that the bulky mesityl groups are effectively decoupling the borazine core from the

Cu(111) top-layer even after the addition of a more reactive hydroxyl moiety. Similar to the borazine **1** case, the distance between the molecule's centre of mass and the surface is ~5.4 Å (~3.0 Å vacuum space) with the borazine core slightly inclined towards the surface and tilted in the direction of the missing mesityl group (Fig. 5.8). This clear physisorption picture is further supported by the relatively small adsorption energy (~0.87 eV) and by the analysis of the pDOS of the adsorbate, where no hybridization or broadening of the frontier molecular orbitals is observed (Fig. 5.9).

Having established the weak character of the molecule-surface interactions, we next extended our analysis to the molecular clusters. Due to the large number of atoms required to model the structure of a whole aggregate, the use of classical molecular dynamics was necessary to contain the computational cost.

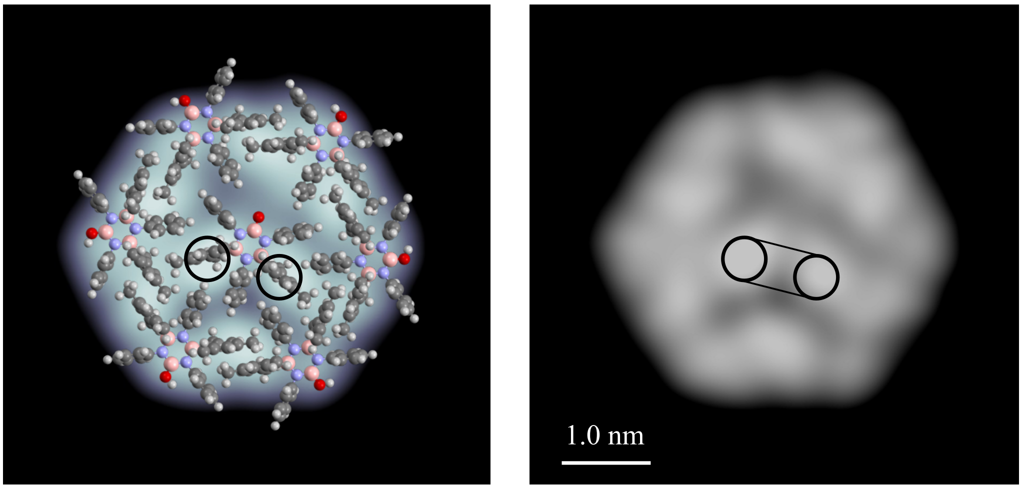

Figure 5.10 Comparison between the calculated minimum energy structure of the regular heptamer and its experimental appearance (left). The detailed features visible in the STM image are nicely reproduced by the ball-and-stick model (black circles correspond to Mes moieties).

By adopting the same protocol described in Section 5.4.1, we focused on the hexagonal 7-mer with the aim of studying the intermolecular interactions at the atomic level. The initial configuration of the 7-mer was inspired by the high-resolution STM images and then simulated by heating (250 K for 1 ns) and quenching (77 K for 5 ns) cycles to allow for structural rearrangement. The calculated minimum energy configuration perfectly corresponds to experiments

(Fig. 5.10). The mesityl groups in the atomistic model are located in correspondence of the bright spot in the STM images (confirming the two-bulge appearance of the molecule) and the hexagonal geometry of the aggregate is nicely preserved. Furthermore, the cluster structure reveals an interdigitation of the aromatic substituents similar to that observed for borazine **1**, indicating that the collective organisation is still driven by π-π stacking. However, attractive interactions alone are not sufficient to explain the sparse self-assembly of borazine **2**, particularly when no strong coordination with the metallic surface is expected to hinder the molecular planar diffusion [11].

On the basis of the indications reported above, it clearly appears that the presence of a competing interaction is required to achieve the formation of the observed bubble-phases [92,93]. This hypothesis will be substantiated during the rest of the Chapter, where deprotonation of the hydroxyl moiety of borazine **2** will be identified as the source of electrostatic repulsion. Our arguments will be based on the analysis of the observed cluster size population followed by its interpretation as a delicate interplay between repulsion and attraction, with an *ad hoc* Monte Carlo model.

5.5.2 *"Magic" clusters from competing interactions*

The interpretation of the distribution of cluster sizes can help the rationalisation of "condensation problems" – in terms of mechanisms of aggregation – by capturing their underlying physics [166]. For instance, a size population displaying sharp features or discontinuities may reveal either enhanced or reduced stability of the correspondent elements, in connection with the interactions regime of the system under study.

The borazine **2**-cluster size distribution was obtained by gathering statistics from an extensive sample of STM topographies, where the total number of analysed clusters exceeds the 300 units. Remarkably, the calculated population shows well-defined peaks for “magic” clusters counting 7, 10, 11, 12 and 13 molecules (Fig. 5.11).

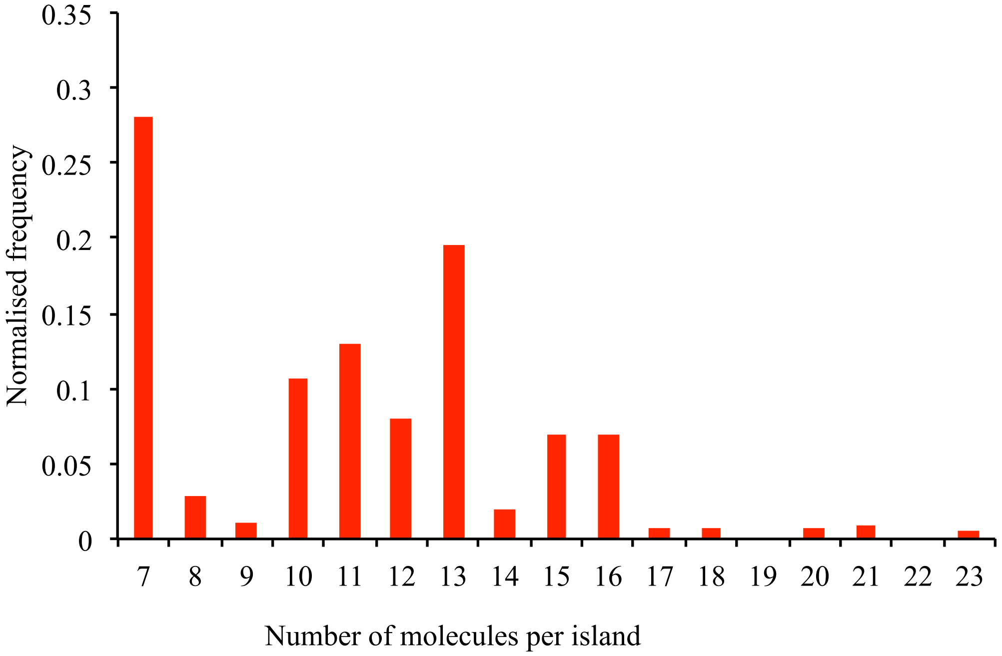

Figure 11 Normalised population of cluster sizes obtained from STM images.

The 7-mer is the most abundant group with a normalized frequency of 28%, followed by the 13-mer with 20% of the total counts. On the other hand, the population of clusters bigger than the 13-mer is very small, showing a first minimum for the 14-mer and eventually fading for sizes beyond the 17-mer. The picture emerging from the above considerations is rather different from the well-known phase coarsening process driven by van der Waals interactions, further suggesting that repulsive forces have to play a role in the evolution of the observed statistics. In this regard, we have already shown in the previous Chapter that simple Monte Carlo simulations on a discrete hexagonal lattice lead to large, single molecular islands for any appropriate van der Waals bonding force in the experimental coverage/temperature range (*i.e.*, the self-assembling behaviour observed for molecule **1** can be explained in these terms), whereas sparse phases are the expected product of systems where competing interactions are acting on different length-scales.

We note that the hydroxyl moiety confers an acidic character to molecule **2**, which leads us to hypothesize that surface-mediated deprotonation might be the origin of repulsive interactions. Deprotonation reactions have been observed (directly or indirectly) several times [164,167] on the relatively reactive copper terraces (possibly mediated by Cu adatoms [168,169]), leading to the formation of adsorbed molecular anions when no coordination with the metal occur [27]. These charged adsorbates are then screened by the surface (*i.e.*, following the standard image charge description) and interact with each other as mutually repulsive negative electrostatic dipoles, supporting our tentative explanation (see Chapter 1, Section 1.3).

Further evidence for the presence of repulsive interaction terms is made available by STM experiments conducted at higher molecular coverage. For longer deposition times of hydroxyl-borazine **2**, the surface density of clusters increases, while the cluster size and shape distributions remain essentially unaffected (see Fig. 5.7). This is brought as a clear indication that the phase coarsening must be limited to the clusters sizes allowed by the ratio between repulsive and attractive interactions acting in the system. Beyond a "critical coverage" (about 0.3 ML), further exposure of the Cu(111) surface to the molecular beam at the same deposition rate (*i.e.*, same mass flux) does not lead to an increased molecular surface coverage. We interpret this phenomenon as the combined result of the relatively low molecular adsorption energy (due to the decoupling effect of the mesityl substituents already described for molecule **1**) and to the high density of molecular dipoles reached at the critical coverage. We find that the adsorbate density can be increased above the critical value (0.3 ML) only for higher molecular deposition rate. In this case, we observe coexistence of extended compact molecular islands with a distribution of isolated clusters similar to that described for lower coverage. We expect the molecules located within the extended islands to be mostly neutral (*i.e.*, still protonated), consistent with a lower degree of dipole-dipole repulsion relative to van der Waals attraction. The fact that this result can be obtained only at high molecular deposition rate points towards a possible kinetically determined origin of this phenomenon [11], which goes beyond the scope of our analysis. Finally, we note that the self-assembly of the non-acidic reference borazine **3** invariably produced large islands, similar to the ones obtained after deposition of molecule **1**. This evidence is brought as a strong indication that the formation of sparse clusters is driven by electrostatic repulsion after deprotonation of the B−OH moiety, which cannot happen for the B−CH_3 of molecule **3**. The discussion above lists just a first set of arguments presented to support our hypothesis and it is functional to introduce the detailed analysis of the system borazine **2**/Cu(111) that will be disclosed in the next Section.

5.6 A model for the “magic” clustering

Further employment of atomic-scale modelling tools to improve our comprehension of the borazine **2** self-assembly would be mostly ineffective, because of the inherent limits of the available theories and the huge size of the relevant systems (in terms of total number of atoms).

The argumentation developed up to this point can be readily translated into a larger scale model, which will still suffer from lack of precision, but which will enable us to test and validate our tentative description by appraising its final outcomes. The information gathered from the STM images and the results of our molecular dynamics simulations can be incorporated into a model where a single molecule is pictured as a generic particle allowed to bind with up to six neighbours, accordingly with the three-fold symmetry dictated by the hexagonal borazine core.

The first trivial consequence of this assumption is that the 7-mer is determined as the first energetically favourable “magic” cluster, in which all the molecules are bound to three neighbours, maximizing the negative van der Waals energy. The formation of an 8-mer and of a 9-mer would require the successive addition of one or two molecules allowed to bind with two others only, causing the new additions to be more "volatile" as demonstrated by the nearly null frequency count for these cluster sizes (cf. Fig. 5.11).

The 10-mer should be another "magic" cluster since it is the next aggregate in which all the molecules can bind with at least three neighbours. In fact, the increased frequency count for the 10-mer reflects the improved van der Waals stabilization whereas its low incidence relatively to the 7-mer (about one third) constitutes a further indication of the presence of competing interactions. Since the hydroxyl moiety shows a definite acidic character (pKa: ~9), molecule **2** can likely undergo deprotonation with the formation of standing negative electrostatic dipoles due to the metal screening. Deprotonation is predictably favoured by the induced polarisation of neighbouring molecules [56], which stabilise the resultant surface dipole by screening. Borazines embedded inside an aggregate are the ones expected to release a proton, hence the 10-mer is the first cluster allowed for multiple deprotonation given that it the first cluster counting two non-peripheral units (Fig. 5.12). We note that any pair of standing dipoles generated by a pair of charged molecules will be engaged in a repulsive long-range energy term (scaling as $1/R^3$, where R is the distance between dipoles) that can be readily implemented in our model. The great number of conformational isomers observed for the 10-mer is consistent with the presence of dipolar repulsion (*i.e.*, multiple deprotonation). The same effect, a sort of "electrostatic melting", has been revealed from STM images also for the 11-mer and 12-mer populations.

The high frequency count for the 13-mer can be explained by using similar arguments. This is the first "magic" cluster within which multiple deprotonation can occur for two molecules that are not nearest neighbours (Fig. 5.12), leading to a consistent reduction of the repulsive energy as revealed by the large experimental population.

The next in the series, namely the 14-mer, is the only cluster allowed to stoichiometrically split into two 7-mers. This decay mechanism might be enforced by the repulsion between the two dipoles included in the 14-mer and would be a viable explanation for its small population and in the same time for the very high incidence of 7-mers (Fig. 5.11).

We conclude the analysis of individual clusters by noting that pairs of deprotonated non-nearest neighbour molecules might be enclosed in any cluster bigger than the 14-mer. Therefore, the number of ions per aggregate could exceed the number of two, with the number of dipole pairs scaling quadratically with the cluster size. Consistently, the observed population of clusters larger than the 16-mer is almost null, since the repulsive energy between several couples of dipoles destabilises larger aggregates.

Following this approach, we can univocally assign an energy value for each cluster size in terms of attractive nearest-neighbours and repulsive $1/R^3$ interactions. These energies can be transformed into transition rates suitable to calculate the evolution of the cluster size population by means of a *kinetic Monte Carlo* (KMC) scheme, where couples of clusters can exchange single molecules. A detailed description of the model will be presented in the next Section together with the obtained results.

5.7 Clustering model: Implementation and results

To rationalize the clustering of molecule **2**, the discussion presented in the previous Section was translated into a simple model Hamiltonian based on a discrete hexagonal mesh, where the energy terms involved are van der Waals and dipolar interactions only.

We assume that the energy of each cluster size has a specific value, resulting from the number of intermolecular “bonds” between neighbour molecules (each one giving a negative contribution) and the number of molecular ions. We impose that repulsive energy within a cluster will be present only if the aggregate is large enough to accommodate more than one “internal” molecule. These molecules can undergo deprotonation (switching on the positive dipolar repulsion term) due to the polarisation of their neighbours, which is itself contributing to the total cluster energy with a negative screening contribution.

The evolution of the system is computed starting from a uniform cluster size distribution, which is then updated by allowing single molecule transfers between clusters pairs. The acceptance and the rejection of these Monte Carlo moves is controlled by a standard Metropolis scheme [83] performed in a loop that terminates when the equilibrium size population is reached. A reference temperature of 200 K was used in the Boltzmann acceptance rate for all calculations, since it is reasonable to assume that the experimental cluster size distribution represent the statistics obtained at temperatures high enough to allow for molecular diffusion.

In order to determine an energy value for each cluster size, the model has to be provided with a set of three parameters describing the attractive van der Waals term σ between nearest neighbours, the dipolar repulsion μ_1 and μ_2 for first and second neighbouring ions (related by inverse cubic scaling with relative distance) and a negative screening term β to account for the polarisation response of each molecule surrounding an ion.

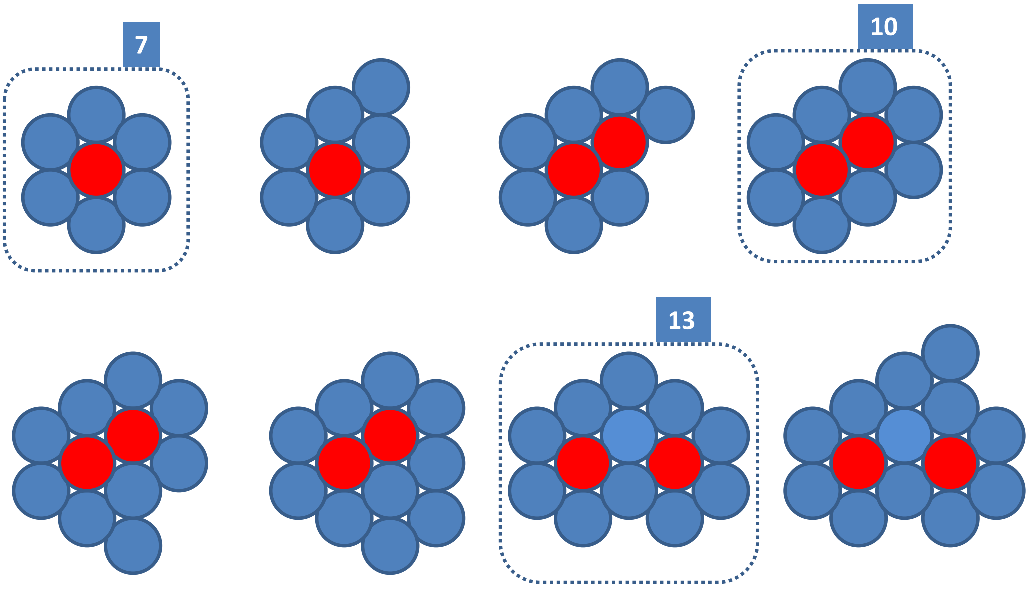

Figure 5.12 Schematic models of molecular clusters (from the 7-mer to the 14-mer), where the geometry is constructed assuming close-packed arrangement and on the basis of the STM observations. Charged molecules are represented by red filled circles (blue for neutral molecules). The dotted frames indicate the “magic” clusters corresponding to the main peaks in the histogram in Fig. 5.11, which represent the first compact cluster (7-mer), the first compact doubly charged cluster (10-mer) and the first cluster with non nearest neighbour charged molecules for (13-mer).

The typical conformations of clusters with size from the 7- to 14-mer were derived from STM images and are shown in Fig. 5.12, where the cluster morphologies are approximated by a simple hexagonal close packed connectivity. The total van der Waals contribution to the cluster energy is then immediately calculated by counting the number of intermolecular connections present in the cluster scheme in Fig. 5.12 (each one brings one σ to the sum). We assume that a molecule nested in an aggregate can undergo deprotonation when it has a minimum of four screening neighbours, implying that the formation of an ion has a fixed energy cost of 4β. In addition, when multiple deprotonation sites are available, the arrangement of the molecular ions within the cluster has to correspond to the minimum energy one. Finally, triple deprotonation is not allowed for the cluster sizes considered (*i.e.*, for cluster from the 4- to the 18-mer). One last parameter is included in the model to capture the rare occurrence of 14-mer and the exceptionally high 7-mer population observed in the experiments. To this aim, we occasionally allow a 14-mer cluster to split into two 7-mers accordingly to some small decay factor f.

The van der Waals interaction parameter σ was computed from molecular dynamics simulations, performed according to the procedure illustrated in Section 5.4.1. The value was easily calculated as $\sigma = (E_7 + 6E_S - 7E_1)/12 = -0.06$ eV, where E_7 is the total energy of a 7-mer adsorbed on the surface, E_S the total energy of the metal slab alone and E_1 the one of a single adsorbed molecule (the unit cell being equal for all the calculations), while the denominator is determined by the number of intermolecular contacts (*e.g.*, twelve in the 7-mer case). Furthermore, the atomistic structural optimization was functional to the estimation of the repulsive Coulomb parameters, since accurate measures of the adsorption geometry and the intermolecular distances were made available for the calculation of μ_1 and μ_2 by means of standard image charge model and dipole-dipole energy equation. Once determined the hydroxyl-surface distance (d_{ads} = 4.81 Å) and the image charge plane displacement for the Cu(111) surface (z = 1.20 Å [170]), the dipole length value was calculated as $l = 2(d_{\text{ads}} - z) = 7.22$ Å, while the distance between the hydroxyl moieties of two nearest neighbour molecules was assumed to be equal to the minimum distance between interacting dipoles (d = 15.00 Å, Fig. 5.13).

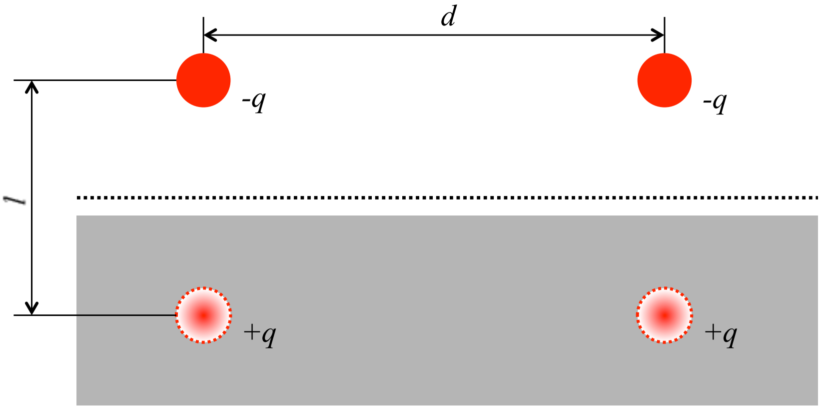

Figure 5.13 Schematic representation of two deprotonated molecules adsorbed on the Cu(111) surface (blue box). The red filled circles represent the hydroxyl radicals while the empty ones indicate the image charges within the metal bulk, generating the negative surface dipole. The distance between the radicals d is 15.00 Å and the dipole length l is 7.22 Å. The dotted line indicates the position of the image charge plane.

From the geometry reported above and consistently with the cluster conformations reported in Fig. 5.12, the repulsion parameters were easily determined with values μ_1= 0.11 eV and $\mu_2 = \mu_1 / 3^{3/2}$ = 0.02 eV for the first- and second-neighbour terms. The screening energy β and the decay ratio f were left as free fitting parameters of the model, with optimised values $\beta = -0.084$ eV and $f = 0.001$ (*i.e.*, the splitting rate of a 14-mer into two 7-mer is set to 0.001 times the decay rate of the competing reaction leading to the detachment of a single molecule and a 13-mer).

The calculated cluster size population nicely reproduces the experimental one (cf. Fig. 5.14), leading us to conclude that the competition between van der Waals attraction and dipole induced repulsion is responsible for the observed sparse clustering of molecule **2**. Even though our modelling approach is not expected to go beyond a qualitative description, we have shown that the main traits of the "magic" clustering can be captured by feeding realistic parameters into a simple aggregation model, if and only if charging effect are accounted for. In fact, if electrostatic repulsion was not considered, the model would invariably produce large aggregates, following the well-known Ostwald ripening process and in full agreement with the self-assembly observed for the non-acidic molecules **1** and **3**.

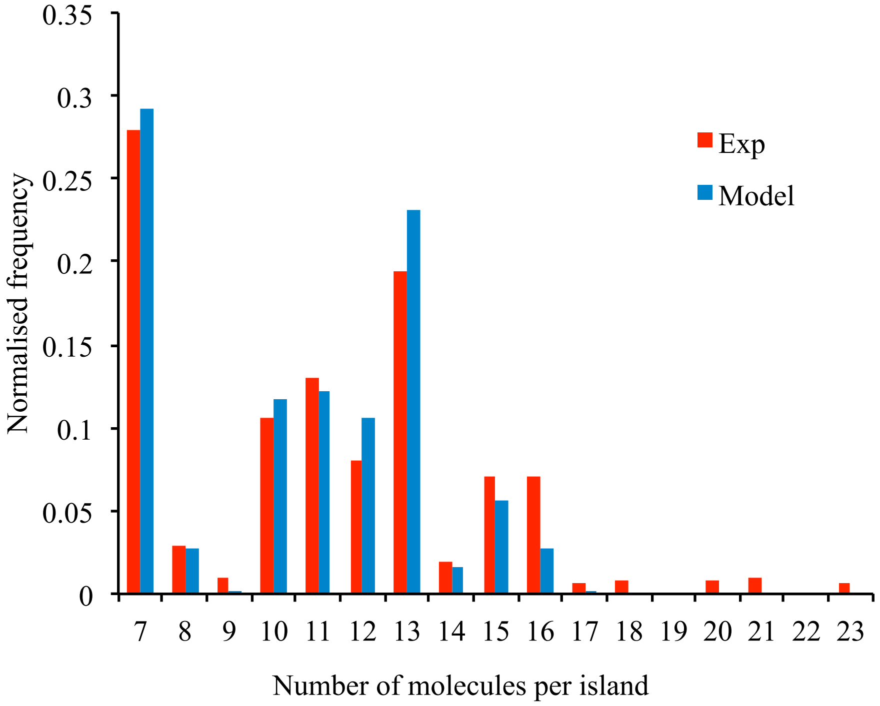

Figure 5.14 Comparison between the experimental (red bars) and the calculated cluster size population (blue bars) of molecule **2**.

This result suggests the possibility of selectively tuning the cluster population (*e.g.*, favouring the occurrence of 7-mers) by adjusting the ratio between attraction and repulsion in hypothetical modified borazines. In the next Section, we will use our Monte Carlo model to predict the effect of possible modifications of the molecular structure.

5.8 Towards monodispersion

The last part of our analysis aims to make use of our KMC model in order to identify the properties of this metal-organic system that can be realistically tuned to obtain some degree of control on the cluster size population.

This analysis entails a formidable task, as many structural and physical parameters could in principle be varied independently. Their list must include the size of the used monomers, the strength of the electric dipole created by deprotonation, and the strength of the attractive "contact" energy. Moreover, it could be extended to include other variables such as the deprotonation energy, the number of detachable protons per monomer, the HOMO and LUMO energy level position with respect to the vacuum level, the choice of the substrate and its related Fermi energy level, the strength of the "pillow" effect [42] and the adsorption coverage. Making reliable predictions across the whole range of all these parameters is clearly beyond the reach of our model, which explicitly contains only the first three items in the above list. However, it is still very interesting to try to isolate those system properties that could control the degree of monodispersion while still being both reliably described by our model and fully within the reach of realistic experiments.

The first structural modification examined was the variation of the radial size of molecule **2**, which would in turn change the distance between deprotonated molecules and thus the attraction/repulsion ratio. The molecular effective diameter might be increased by the insertion of ethynyl/polyphenyl spacers linking the borazine core to the peripheral aryl and mesityl groups.

However, assuming that deprotonation could still occur, this would result in a larger distance between dipoles with the consequent fall of the fast-decaying $1/R^3$ repulsion, which is expected to consistently favor the formation of large aggregates, reducing the selectivity towards a specific size. On the other hand, the reduction of the molecular radius of borazine **2** by substituting its aromatic moieties with bulky but shorter isoalkyl/isoalkenyl substituents would definitely favor small cluster sizes and thus promote *monodispersion*. Anyway, we note that the replacement of the aryl moieties, which are accountable for the rather strong π-π interactions, would drastically decrease the contact energy (thus severely limiting the formation of self-assembled structures).

Secondly, the intensity of the dipole generated by a molecular ion could be adjusted by varying the distance between the hydroxyl moiety and the surface. Such distance is thus a parameter acting on the repulsion strength without changing the molecular radius (*i.e.*, not changing the van der Waals attraction). The lifting of the molecule could be obtained by substituting the methyl terminals of the mesityl groups with bulkier ethenyl, *iso*-propyl or *tert*-butyl fragments, progressively increasing the adsorption distance. The electrostatic dipole would consequently increase, since it is proportional to the distance between the deprotonated hydroxyl and the image-charge plane of the metal surface, and thus strengthen the electrostatic terms, which are proportional to the square of the dipole magnitude. This effect could be easily reproduced in terms of our KMC model by correcting the dipole intensity with a multiplicative coefficient $\alpha \in [0.85, 1.30]$ ($\alpha = l_r / l$, where l_r is the modified dipole length and $l = 7.22$ Å is the original value calculated for molecule **2**). We note that – within the selected α range – the variation of the screening energy caused by an enhanced dipole strength was determined to be still sufficient to balance the accordingly altered deprotonation energy (due to the reduced image charge screening). Therefore, we could leave unmodified the original assumption for which deprotonation might occur for molecules surrounded by four or more others.

Finally, the attraction/repulsion ratio of adsorbed borazines **2** could be tuned by modifying the chemical and electronic nature of the lateral aryl moieties, without considerably changing either the radial size of the molecule or its distance to the substrate. Essentially, the π stacking interactions due to interdigitation of molecules **2** could be weakened or enhanced by introducing bulkier branched terminals or different heterogroups (acting as electron-acceptor or donor) to the aryl moieties. This would turn into the alteration of the van der Waals cohesive energy, without affecting the electrostatic terms.

Again, this scenario was represented in our KMC model by simply changing the van der Waals cohesive energy within the range $\sigma_r = \lambda\,\sigma$ with $\lambda \in [0.5, 1]$, where $\sigma = -0.06$ eV is the calculated value for molecule **2**, while leaving the electrostatic contributions unchanged.

The discussion above relies on the reasonable expectation that increasing the ratio between repulsive and attractive contributions would yield enhanced monodispersion by destabilising clusters containing more than one deprotonated molecule. This was readily tested with our KMC model by defining a set of values for the two parameters α and λ, acting on the electrostatic and van der Waals terms respectively, and by calculating the cluster size population as a function of α and λ within their stated range. The predicted evolution of the cluster size population is reported in Fig. 15, where the 7-mer cluster emerges as the selectively monodispersed species. For instance, we find that increasing the molecule-surface distance by as little as 0.5 Å (*i.e.*, increasing the dipole length by 1 Å) would increment the frequency count of 7-mer from ~30% to ~60% (cf. Fig. 5.15 for $\alpha = 1.00$ and $\alpha = 1.15$, respectively). A similar effect is predicted to occur for a reduced van der Waals energy term, with the population of 7-mers exceeding 75% after lowering the contact energy to 70% of the value calculated for the original molecule **2** (Fig. 5.15 bottom). Again, we note that although inevitably qualitative, the predictions reported above are attempted relatively to variations of physical properties – namely electrostatic scaling and van der Waals energy terms – that must follow the hypothesised structural modifications of borazine **2**. In this regard, it is reasonable to expect that the synergic combination of the two investigated approaches can be implemented in real experiments in order to compensate for any unexpected limitation in reproducing the proposed adjustments, *i.e.*, creating new systems in which the dipole strength and the cohesive energy are varied concertedly. Our results brought us to speculate that this approach could be applied to obtain a certain control on the self-assembly behaviour of metal-organic systems in which electrostatic repulsions are produced not only by irreversible processes like deprotonation.

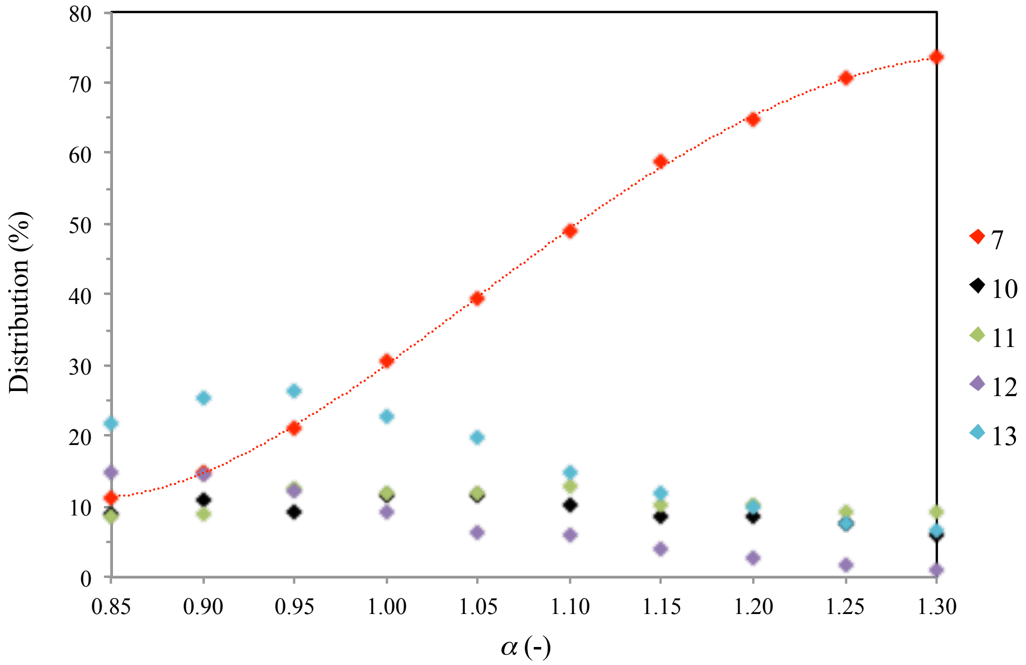

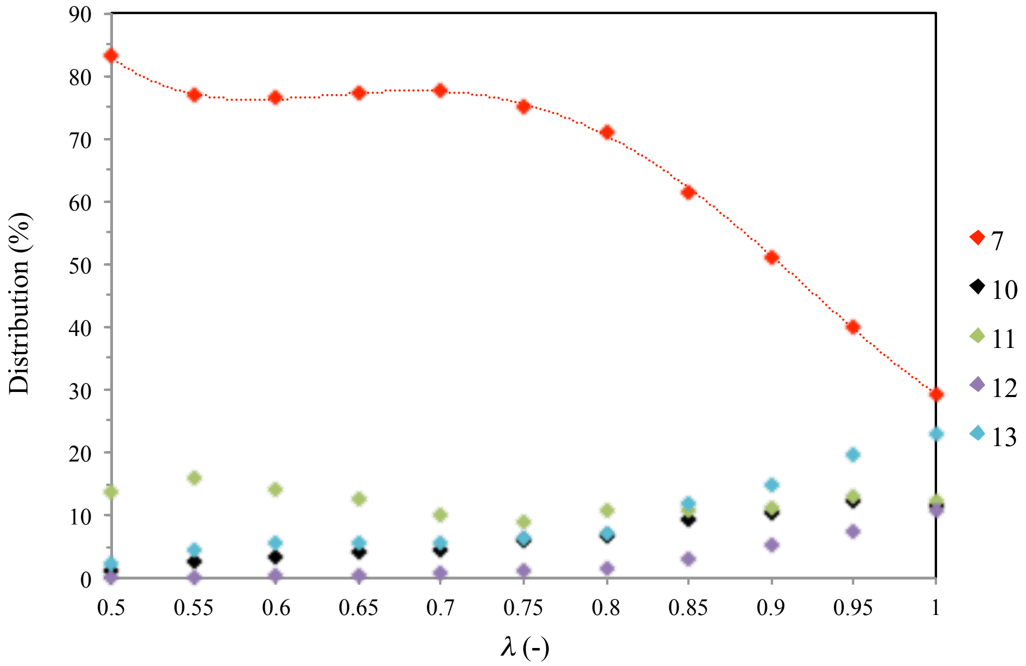

Figure 5.15 *Top panel*: predicted evolution of the “magic” cluster size distribution as a function of the relative dipole strength α, where $\alpha = 1$ corresponds to the original borazine **2** system. The graph suggests that monodispersion towards the 7-mer could be obtained increasing the adsorption distance of deprotonated borazines. *Bottom panel*: predicted cluster size population as a function of the relative contact energy λ, where $\lambda = 1$ returns the original system. A strongly monodispersed 7-mer population could be achieved by decreasing the contact energy between neighbour molecules to 50% of its original value (see text).

5.9 Conclusions

The investigation presented in this Chapter resolved the self-assembly behaviour of molecules subject to irreversible ionisation upon adsorption on the Cu(111) surface, with the formation of a distinctive cluster size population.

We acknowledge previous reports describing two-dimensional [27] and one-dimensional [26] structures, where repulsion was shown to be strong enough to shape the large-scale features of extended supramolecular structures. Additionally, arrays of isolated molecules – where electrostatic repulsions prevented any assembly – have also been presented before [60,122]. The main novelty we presented here is the degree of control of the repulsion-driven self-assembly, enabled by molecular design, assisted by theoretical modelling and verified by STM observations. This allowed a new balanced midway between the two general situations above, illustrated by the assembly of "magic cluster" structures due to partial deprotonation.

Our integrated approach involved the synthesis of novel boron nitride-doped materials, *i.e.*, unprecedented borazine molecules prepared by means of a new synthetic protocol, allowing the controlled insertion at the B atom centres of different functional groups (B–Mes, B–OH and B–CH_3 for borazine **1**, **2** and **3**, respectively) within a common molecular framework. This allowed enabling selective deprotonation of the (B–OH)-bearing **2** units, introducing long-range repulsions on top of essentially the same short-range van der Waals attractions acting between B–Mes and B–CH_3 substituted, neutral borazines **1** and **3**. Our goal was to use the on-the-surface deprotonation reactions to generate extended repulsive intermolecular forces driving the cluster self-assembly, and then check that repulsion controls the system's behaviour by "null experiments" on the neutral control molecule **3**.

The common molecular framework of the investigated unit molecules was optimized for efficient core-substrate decoupling by selecting bulky, sterically hindering phenyl and mesityl substituents. This caused all the units to behave essentially as van der Waals spheres, so that their supramolecular self-assembly is predictably guided by intermolecular forces rather than by surface-molecule interactions.

STM experiments revealed that for the case of our B–OH molecule **2**, the interplay of attractive and repulsive forces drives the formation of small supramolecular clusters. These clusters reach the optimal net charge for their precise shape and connectivity through selective deprotonation, such that only one or two molecules in each cluster actually deprotonate. The process yields an enhanced statistics for magic cluster size numbers. This result is by no means a coincidence, as the size and structure of our unit monomers is such that the two opposite interactions (with their different laws of decay with distance) approximately balance each other for small cluster sizes. Achieving a more complete control on the experimental cluster size distribution after further refinement of the molecular structure of the borazine tectons is certainly a possibility revealed by our work. Most notably, *controlling the degree of monodispersion* may be not unconceivable from here. This is an important point, even though we cannot experimentally investigate it without a full new synthesis cycle, which is anyway in process.

Chapter 6

Outlook and conclusions

This thesis addressed the self-assembly of novel carbon-based molecular units adsorbed on coinage metal surfaces, using an investigation scheme based on multiscale theoretical modelling and scanning tunneling microscopy techniques. Starting from the design of specific molecular units, we created metal-organic systems where the formation of surface dipoles, upon either charge transfer or surface-mediated reaction, could be clearly discerned by analysing their effects on the development of supramolecular structures. This strategy was applied to different metal-molecule combinations to shed light on the mechanisms and identify the factors involved in the formation of strong surface dipoles and their influence on the self-assembly motifs. In fact, the presence of dipoles generates repulsive forces acting in the medium-long range, which oppose the omnipresent attractive dispersion forces between molecules and lead to the formation of modulated phases, depending on the relative strength of the competing interactions.

We first investigated the self-assembly behaviour of a modified pyrene molecule (TBP) designed to weakly interact with the (111) surfaces of Cu and Au. In this case, the molecular electronic structure did not change upon adsorption due to the minimal hybridisation with metallic states. Therefore, the energy level alignment at the junction could be described by the *integer charge* *transfer model* (ICT), meaning that the occurrence of charge migration is determined exclusively by the position of the frontier molecular orbital relatively to the metal Fermi level. To assess the influence of the choice of the molecule-metal combination, TBP molecules were designed to have – upon adsorption – an ionisation potential similar to the work function of the chosen substrate. The observation of different self-assembly motifs for TBP molecules adsorbed on Cu(111) and Au(111) could then be strictly assigned to diverse charge transfer effects, since the molecule-molecule and molecule-surface interactions are analogous on both surfaces.

On the Au(111) surface, the *anomalous coarsening* observed at low coverage (*i.e.*, the formation of sparse molecular islands) and the coexistence of small and large aggregates at higher molecular deposition were explained as the result of the competition between van der Waals attraction and long-range repulsion between dipoles generated by *reversible charge transfer* through the metal-organic junction (as rationalised by our Monte Carlo model). Conversely, the observation of single compact aggregates for TBP molecules adsorbed on Cu(111) was compatible with the standard Ostwald ripening process driven by dispersion interactions, hence excluding charge migration for this molecule-metal combination. Therefore, our analysis allowed to clearly identify the importance of the choice of the molecule-metal couple in determining the occurrence of charge transfer, the formation of interfacial dipoles and, eventually, in driving the development of novel supramolecular structures. In this particular case, the occurrence of ICT could be activated or forbidden by changing the electrode.

The second investigation analysed the codeposition of TBP with an acceptor molecule (TCNQ). Our results demonstrated that the donation of charge from a donor species (TBP) could activate charge transfer from Au(111) to TCNQ, which would be otherwise forbidden. This is explained in terms of local modulations of the electrostatic potential induced by the donor molecules, whose effect is to locally reduce the work function of the substrate and thus to enable the transfer of electrons from the noble metal to the acceptor molecule.

This “induced charge transfer” picture was confirmed by the observation of self-assembled structures that could be explained only if both TBP and TCNQ were carrying opposite charge, as confirmed by our theoretical models. In particular, we observed the formation of several TCNQ islands surrounded by single-molecule-thick TBP frames. In these structures, the TCNQ was involved in the formation of an organic salt, where *positive* Au adatoms were incorporated in the *anionic* network with 1:1 stoichiometry in order to screen the electrostatic repulsion between negatively charged molecules.

In our last analysis, we studied the self-assembly of an unprecedented class of organic substituted borazine molecules deposited on the Cu(111) surface. Here, we demonstrated how electrostatic repulsion between adsorbed monomers could be achieved by following the route of surface-mediated chemical reaction, at variance with the charge transfer upon energy level alignment used in the previous investigations. In fact, the formation of size-selective molecular clusters was obtained by introducing a reactive hydroxyl moiety in a previously inert molecular structure. The added acidic character was found sufficient to activate deprotonation on the Cu(111) substrate. A simple Monte Carlo model, based on the balance between electrostatic repulsion and dispersion attraction, nicely reproduced the experimental cluster size distribution and predicted the possibility of tuning the molecular structure (*i.e.*, the ratio between attraction and repulsion) in order to selectively favour specific cluster sizes.

In conclusion, we believe that achieving control on the charge rearrangement processes that occur at the metal-organic interface can represent a new way for directing molecular self-assembly. The possibility of predicting and controlling the formation of self-assembled molecular structures over hundreds of nanometers, as suggested by our results, may be useful for the integration of bottom up and top down nanofabrication techniques. Moreover, our analysis highlighted the importance of the choice of the molecule-metal combination to selectively activate or inhibit the donor or acceptor properties of organic materials with potential application in organic electronics. This knowledge can be applied to the design and synthesis of “molecular dopants” for the fine-tuning of the work function of metal electrodes, which would be beneficial for the fabrication of devices with improved efficiency.

More molecular units are currently being prepared and studied with the aim of improving the prediction and control of the electronic properties of the metal-organic junction. In particular, we are studying molecules where factors such as molecular size/functionalisation, permanent dipole, adsorption height, ionisation potential, *etc*., are modified to further study their influence on the energy level alignment and surface chemistry. The information collected from this new series of investigations will help rationalise the approach to the design of metal-organic systems, which is currently based on the trial and error selection of the metal and organic materials.

Bibliography

[1]
G.M. Whitesides and B. Grzybowski, *Self-assembly at all scales*, Science **295**, 2418 (2002)

[2]
A. Klug, *From macromolecules to biological assemblies (Nobel Lecture)*, Angew. Chem. Int. Ed. **22**, 565 (1983)

[3]
B.D. Gates *et al*, *New approaches to nanofabrication: molding, printing and other techqniques*, Chem. Rev. **105**, 1171 (2005)

[4]
G. Binnig and H. Rohrer, *Scanning tunneling microscopy: from birth to adolescence*, Rev. Mod. Phys. **59**, 615 (1987)

[5]
D.M. Eigler and E.K. Schweizer, *Positioning single atoms with a scanning tunneling microscope*, Nature **344**, 524 (1990)

[6]
J.K. Gimzewski and C. Joachim, *Nanoscale science of single molecules using local probes*, Science **283**, 1683 (1999)

[7]
J.M. Lehn, *Supramolecular chemistry: concepts and perspectives*, WCH, Weinheim (1995)

[8]
M.T. Bohr, *Nanotechnology goals and challenges for electronics applications*, IEEE Trans. Nanotechnol. **1**, 56 (2002)

[9]
C.T. Black *et al*, *Polymer self-assembly in semiconductor microelectronics*, IBM J. Res. Dev. **51**, 605 (2007)

[10]
M.P. Stoykovich and P.F. Nealey, *Block copolymers and conventional lithography*, Materials Today **9**, 20 (2006)

[11]
J.V. Barth *et al*, *Engineering atomic and molecular nanostructures on surfaces*, Nature **437**, 671 (2005)

[12]
Z.Y. Zhang and M.G. Lagally, *Atomistic processes in the early stages of thin-film growth*, Science **276**, 377 (1997)

[13]
H. Brune, *Microscopic view of the epitaxial growth: Nucleation and aggregation*, Surf. Sci. Rep. **31**, 121 (1998)

[14]
J.V. Barth, *Transport of adsorbates at metal surfaces: From thermal migration to hot precursors*, Surf. Sci. Rep. **40**, 75 (2000)

[15]
G.M. Whitesides and M. Boncheva, *Beyond molecules: self-assembly of mesoscopic and macroscopic components*, PNAS **99**, 4769 (2002)

[16]
J.A. Venables, *Nucleation growth and pattern formation in heteroepitaxy*, Physica A **239**, 35 (1997)

[17]
J.V. Barth, *Molecular architectonics on metal surfaces*, Annu. Rev. Phys. Chem. **58**, 375 (2007)

[18]
G. Tomba *et al*, *Atomic-level studies of molecular self-assembly on metallic surfaces*, Adv. Mater. **21**, 1055 (2009)

[19]
M. Simard *et al*, *Use of hydrogen bonds to control molecular aggregation: Self-assembly of three-dimensional networks with large chambers*, J. Am. Chem. Soc. **113**, 4696 (1991)

[20]
M. Böhringer *et al*, *Two-Dimensional Self-Assembly of Supramolecular Clusters and Chains*, Phys. Rev. Lett. **83**, 324 (1999)

[21]
B.J. Holiday and C.A. Mirkin, *Strategies for the construction of supramolecular compounds through coordination chemistry*, Angew. Chem. Int. Ed. **40**, 2022 (2002)

[22]
J.A.W. Elemans *et al*, *Molecular materials by self-assembly of porphyrins, phthalocyanines, and perylenes*, Adv. Mater. **18**, 1251 (2006)

[23]
M. Lingenfelder *et al*, *Tracking the chiral recognition of adsorbed dipeptides at the single-molecule level*, Angew. Chem. Int. Ed. **46**, 4492 (2007)

[24]
R. Otero *et al*, *Elementary structural motifs in a random network of cytosine adsorbed on a gold(111) surface*, Science **319**, 312 (2008)

[25]
S. Vijayaraghavan *et al*, *Supramolecular assembly of interfacial nanoporous networks with simultaneous expression of metal-organic and organic-bonding motifs*, Chem. Eur. J. **19**, 14143 (2013)

[26]
G. Tomba *et al*, *Supramolecular self-assembly driven by electrostatic repulsion: the 1D aggregation of rubrene pentagons on Au(111)*, ACS Nano **4**, 7545 (2010)

[27]
D. Payer *et al*, *Ionic hydrogen bonds controlling two-dimensional supramolecular systems at a metal surface*, Chem. Eur. J. **13**, 3900 (2007)

[28]
S.M. Barlow and R. Raval, *Complex organic molecules at metal surfaces: bonding, organisation and chirality*, Surf. Sci. Rep. **50**, 201 (2003)

[29]
F. Rosei *et al*, *Properties of large organic molecules at surfaces*, Prog. Surf. Sci. **71**, 95 (2003)

[30]
S. Lukas *et al*, *Novel mechanism for molecular self-assembly on metal substrates: Unidirectional rows of pentacene on Cu(110) produced by substrate-mediated repulsion*, Phys. Rev. Lett. **88**, 028301 (2002)

[31]
A. Nilsson and L.G.M. Pettersson, *Chemical bonding on surfaces probed by X-ray emission spectroscopy and density functional theory*, Surf. Sci. Rep. **55**, 49 (2004)

[32]
N. Lin *et al*, *Real-time single-molecule imaging of the formation and dynamics of coordination compounds*, Angew. Chem. Int. Ed. **41**, 4779 (2002)

[33]
A. Michaelides and M. Scheffler, *An introduction to the theory of crystalline elemental solids and their surfaces*, in “Surface and interface science, Volume 1: Concepts and methods”, Wiley-VCH (2012)

[34]
N.W. Ashcroft and N.D. Mermin, *Solid State Physics*, Saunders College Publishing, Texas (1985)

[35]
P.C. Rusu *et al*, *Dipole formation at interfaces of alkanethiolate self-assembled monolayers and Ag (111)*, J. Phys. Chem. C **111**, 14448 (2007)

[36]
J. Perdereau *et al*, *Adsorption and surface alloying of lead monolayers on (111) and (110) faces of gold*, J. Phys. F Met. Phys. **4**, 798 (1974)

[37]
J.V. Barth *et al*, *Scanning tunneling microscopy observations on the reconstructed Au(111) surface - atomic structure, long-range superstructure, rotational domains, and surface-defects*, Phys. Rev. B **42**, 9307 (1990)

[38]
A. Gross, *Theoretical surface science: a microscopic perspective*, Springer, London (2002)

[39]
C.T. Rettner and D.J. Auerbach, *Chemical dynamics at the gas-surface interface*, J. Phys. Chem. **100**, 13021 (1996)

[40]
M. Scheffer and C. Stamp, *Theory of adsorption on metal substrates*, in “Handbook of Surface Science” (Volume 2), Elsevier, Amsterdam (2000)

[41]
K. Hagen, *Organic thin-film transistors*, Chem. Soc. Rev. **39**, 2643 (2010)

[42]
H. Ishii *et al*, *Energy level alignment and interfacial electronic structure at organic/metal and organic/organic interfaces*, Adv. Mater. **11**, 605 (1999)

[43]
I.G. Hill *et al*, *Molecular level alignment at organic semiconductor/metal interfaces*, Appl. Phys. Lett. **73**, 662 (1998)

[44]
A. Kahn *et al*, *Electronic structure and electrical properties of interfaces between metals and π-conjugated molecular films*, J. Polym. Sci. Pol. Phys. **41**, 2529 (2003)

[45]
M. Fahlman *et al*, *Electronic structure of hybrid interfaces for polymer-based electronics*, J. Phys. Condens. Mat. **19**,183202 (2007)

[46]
P.S. Bagus *et al*, *Exchange-like effects for closed-shell adsorbates: interface dipole and work function*, Phys. Rev. Lett. **89**, 096104 (2002)

[47]
G. Witte *et al*, *Vacuum level alignment at organic/metal junctions: "cushion" effect and the interface dipole*, Appl. Phys. Lett. **87**, 263502 (2005)

[48]
H. Vazquez *et al*, *Dipole formation at metal/PTCDA interfaces: role of the charge neutrality level*, Europhys. Lett. **65**, 802 (2004)

[49]
H. Vazquez *et al*, *Barrier formation at metal-organic interfaces: dipole formation and the charge neutrality level*, Appl. Surf. Sci. **234**, 107 (2004)

[50]
H. Vazquez *et al*, *A unified model for metal-organic interfaces: IDIS, "pillow" effect and molecular permanent dipoles*, Appl. Surf. Sci. **254**, 378 (2007)

[51]
P.S. Davids *et al*, *Nondegenerate continuum model for polymer light-emitting diodes*, J. Appl. Phys. **78**, 4244 (1995)

[52]
P.S. Davids *et al*, *Non-degenerate continuum model for polymer light emitting diodes*, J. Appl. Phys. **78**, 4244 (1995)

[53]
C. Tengstedt *et al*, *Fermi-level pinning at conjugated polymer interfaces*, Appl. Phys. Lett. **88**, 053502 (2006)

[54]
E.V. Tsiper and Z.G. Soos, *Electronic polarization in pentacene crystals and thin films*, Phys. Rev. B **68**, 085301 (2003)

[55]
F. Amy *et al*, *Polarization at the gold/pentacene interface*, Org. Electron. **6**, 85 (2005)

[56]
J.B. Neaton *et al*, *Renormalization of molecular electronic levels at metal-molecule interfaces*, Phys. Rev. Lett. **97**, 216405 (2006)

[57]
M. Böhringer *et al*, *Two-dimensional self-assembly of supramolecular clusters and chains*, Phys. Rev. Lett. **83**, 324 (1999)

[58]
J. Weckesser *et al*, *Mesoscopic correlation of supramolecular chirality in one-dimensional hydrogen-bonded assemblies*, Phys. Rev. Lett. **87**, 096101 (2001)

[59]
A.E. Baber *et al*, *Dipole-driven ferroelectric assembly of styrene on Au(111)*, J. Am. Chem. Soc. **129**, 6368 (2007)

[60]
T. Yokoyama *et al*, *Quantitative analysis of long-range interactions between adsorbed dipolar molecules on Cu(111)*, Phys. Rev. Lett. **98** , 206102 (2007)

[61]
R.M. Martin, *Electronic structure: Basic theory and practical methods*, Cambridge University Press, Cambridge (2004)

[62]
D. Frenkel and B. Smit, *Understanding molecular simulation: from algorithms to applications*, Academic Press, New York (2001)

[63]
A. Della Pia and G. Costantini, *Scanning tunneling microscopy*, in “Surface science techniques”, Springer, London (2013)

[64]
L. Verlet, *Computer "experiments" on classical fluids: Thermodynamical properties of Lennard-Jones molecules*, Phys. Rev. **159**, 98 (1967)

[65]
W.D. Cornell *et al*, *A second generation force field for the simulation of proteins, nucleic acids and organic molecules*, *J. Am. Chem. Soc.* **117**, 5179 (1995)

[66]
T. Darden *et al*, *Particle mesh Ewald: An* $N \cdot \log(N)$ *method for Ewald sums in large systems*, J. Chem. Phys. **98**, 10089 (1993)

[67]
P.L. Freddolino *et al*, *Molecular dynamics simulations of the complete satellite tobacco mosaic virus*, Structure **14**, 437 (2006)
[68]
F. Iori and S. Corni, *Including image charge effects in the molecular dynamics simulations of molecules on metal surfaces*, J. Comput. Chem. **29**, 1656 (2008)

[69]
F. Iori *et al*, *GolP: An atomistic force-field to describe the interaction of proteins with Au(111) surfaces in water*, J. Comput. Chem. **30**, 1465 (2009)

[70]
A.C.T. van Duin *et al*, *ReaxFF: A Reactive Force Field for Hydrocarbons*, J. Phys. Chem. A **105**, 9396 (2001)

[71]
P. Hohenberg and W. Kohn, *Inhomogeneous electron gas*, Phys. Rev. **136**, B864 (1964)

[72]
W. Kohn and L.J. Sham, *Self-consistent equations including exchange and correlations effects*, Phys. Rev. **140**, A1133 (1965)

[73]
Y. Gao and X.C. Zeng, *Ab initio study of hydrogen adsorption on benzenoid linkers in metal-organic framework materials*, J. Phys. Condens. Mat. **19**, 386220 (2007)

[74]
M. Dion *et al*, *Van der Waals density functional for general geometries,* Phys. Rev. Lett. **92**, 22 (2004)

[75]
G. Roman-Perez and J.M. Soler, *Efficient implementation of the van der Waals density functional: Application to double-wall carbon nanotubes,* Phys. Rev. Lett. **103**, 096102 (2009)

[76]
A.J. Cohen *et al*, *Insights into current limitations of density functional theory*, Science **321**, 792 (2008)

[77]
J.P. Perdew and A. Zunger, *Self-interaction correction to density-functional approximations for many-electron systems*, Phys. Rev. B **23**, 5048 (1981)

[78]
L. Kleinman and D.M. Bylander. *Efficacious form for model pseudopotentials*, Phys. Rev. Lett. **48**, 1425 (1982)

[79]
D. Vanderbilt, *Soft self-consistent pseudopotentials in a generalized eigenvalue formalism*, Phys. Rev. B **41**, 7892 (1990)

[80]
D. Chandler, *Introduction to modern statistical mechanics*, Oxford University Press, Oxford (1987)

[81]
T.R. Weikl and R. Lipowsky, *Local adhesion of membranes to striped surface domains*, Langmuir **16**, 9338 (2000)

[82]
T.R. Weikl *et al*, *Adhesion of membranes with competing specific and generic interactions*, Eur. Phys. J. E **8**, 59 (2002)

[83]
N. Metropolis *et al*, *Equation of state calculations by fast computing machines*, J. Chem. Phys. **21**, 1087 (1953)

[84]
G. Binnig, H. Rohrer *et al*, *Tunneling through a controllable vacuum gap*, Appl. Phys. Lett. **40**, 178 (1982)

[85]
G. Binnig, H. Rohrer *et al*, *Surface studies by scanning tunneling microscopy*, Phys. Rev. Lett. **49**, 57 (1982)

[86]
J. Tersoff and D.R. Hamann, *Theory of the scanning tunneling microscope*, Phys. Rev. B **31**, 805 (1985)

[87]
M. Harada *et al*, *Ionisation energies for aromatic hydrocarbons*, Chem. Phys. Lett. **303**, 489 (1999)

[88]
A.I.S. Holm *et al*, *Dissociation and multiple ionization energies for five polycyclic aromatic hydrocarbon molecules*, J. Chem. Phys. **134**, 044301 (2011)

[89]
L. Crocker *et al*, *Electron affinities of some polycyclic aromatic hydrocarbons, obtained from electron-transfer equilibria*, J. Am. Chem. Soc. **115**, 7818 (1993)

[90]
A. Della Pia, M. Riello *et al*, *Anomalous coarsening driven by reversible charge transfer at metal-organic interfaces*, Nat. Commun., Submitted (2013)

[91]
I. Fernandez-Torrente *et al*, *Long-Range Repulsive Interaction between Molecules on a Metal Surface Induced by Charge Transfer*, Phys. Rev. Lett. **99**, 176103 (2007)

[92]
M. Seul and D. Andelman, *Domain Shapes and Patterns: The Phenomenology of Modulated Phases*, Science **267**, 476 (1995)

[93]
Y. Bar-Yam, *Dinamics of complex systems*, Westview Press, Oxford (1997)

[94]
S. Braun *et al*, *Energy level alignment at organic/metal and organic/organic interfaces*, Adv. Mater. **21**, 1450 (2009)

[95]
A. Ferretti *et al*, *Mixing of Electronic States in Pentacene Adsorption on Copper*, Phys. Rev. Lett. **99**, 046802 (2007)

[96]
W. Liu *et al*, *Structure and energetics of benzene adsorbed on transition-metal surfaces: density-functional theory with van der Waals interactions including collective substrate response*, New J. Phys. **15**, 053046 (2013)

[97]
D. Wan *et al*, *Adlayer structures of pyrene and perylene on Cu(111): An in situ STM study*, Surf. Sci. Lett. **478**, L320 (2001)

[98]
C.B. France and B. A. Parkinson, *Chiral morphologies and interfacial electronic structure of naphtho[2,3-a]pyrene on Au(111)*, Langmuir **20**, 2713 (2004)

[99]
P. Giannozzi *et al*, *QUANTUM ESPRESSO: a modular and open-source software project for quantum simulations of materials*, J. Phys. Condens. Matter **21**, 395502 (2009)

[100]
J.P. Perdew *et al*, *Generalized Gradient Approximation Made Simple*, Phys. Rev. Lett. **77**, 3865 (1996)

[101]
G. Makov and M. C. Payne, *Periodic boundary conditions in ab initio calculations,* Phys. Rev. B **51**, 4014 (1995)

[102]
L. Bengtsson, *Dipole correction for surface supercell calculations*, Phys. Rev. B **59**, 12301 (1999)

[103]
J. Neugebauer and M. Scheffler, *Adsorbate-substrate and adsorbate-adsorbate interactions of Na and K adlayers on Al(111)*, Phys. Rev. B **46**, 16067 (1992)

[104]
D.A. Case *et al*, *The Amber biomolecular simulation programs*, J. Computat. Chem. **26,** 1668 (2005)

[105]
S. Plimpton, *Fast parallel algorithms for short-range molecular dynamics*, J. Comp. Phys. **117**, 1 (1995)

[106]
J. Wang *et al*, *Development and testing of a general AMBER force field*, J. Computat. Chem. **25**, 1157 (2004)

[107]
S. Lukas *et al*, *Adsorption of acenes on flat and vicinal Cu(111) surfaces: Step induced formation of lateral order*, J. Chem. Phys. **114**, 10123 (2001)

[108]
S.M. Wetterer *et al*, *Energetics and kinetics of the physisorption of hydrocarbons on Au(111)*, J. Phys. Chem. B **102**, 9266 (1998)

[109]
T.E. Dirama *et al*, *Conformation and dynamics of arylthiol self-assembled monolayers on Au(111)*, *Langmuir* **23**, 12208 (2007)

[110]
C.F. Macrae *et al*, *Mercury CSD 2.0 - new features for the visualization and investigation of crystal structures*, J. Appl. Cryst. **41**, 466 (2008)

[111]
I. Horcas *et al*, *WSXM: A software for scanning probe microscopy and a tool for nanotechnology*, Rev. Sci. Instrum. **78**, 013705 (2007)

[112]
P.M. Voorhees, *The theory of Ostwald ripening*, J. Stat. Phys. **38**, 231 (1985)

[113]
B.K. Chakraverty, *Grain size distribution in thin films. I. conservative systems*, J. Phys. Chem. Solids **28**, 2401 (1967)

[114]
P. Wynblatt and N.A. Gjostein, *Supported metal crystallites*, Prog. Solid State Chem. **9**, 21 (1975)

[115]
F. Bussolotti and R. Friedlein, *Hybridization and charge transfer at the anthracene/Cu(110) interface: Comparison to pentacene*, Phys. Rev. B **81**, 115457 (2010)

[116]
E.V. Chulkov *et al*, *Image potential states on metal surfaces: binding energies and wave functions*, Surf. Sci. **437**, 330 (1999)

[117]
F.T. Smith, *Capacitive Energy and Ionization of Aromatic Hydrocarbons*, J. Chem. Phys. **34**, 793 (1961)

[118]
L. Vitali *et al*, *Portrait of the potential barrier at metal–organic nanocontacts*, Nat. Mater. **9**, 320 (2010)

[119]
G. Rojas *et al*, *Surface state engineering of molecule–molecule interactions*, Phys. Chem. Chem. Phys. **14**, 4971 (2012)

[120]
G. Binnig and H. Rohrer, *Scanning tunneling microscopy*, Surf. Sci. **126**, 236 (1983)

[121]
C. Hückstädt *et al*, *Work function studies of rare-gas/noble metal adsorption systems using a Kelvin probe*, Phys. Rev. B **73**, 075409 (2006)

[122]
J. Fraxedas *et al*, *Modulation of surface charge transfer through competing long-range repulsive versus short-range attractive interactions*, J. Phys. Chem. C **115**, 18640 (2011)

[123]
M.C. Blüm *et al*, *Conservation of chirality in a hierarchical supramolecular self-assembled structure with pentagonal symmetry*, Angew. Chem. Int. Ed. **44**, 5334 (2005)

[124]
A.D. Jewell *et al*, *Magic electret clusters of 4-fluorostyrene on metal surfaces*, J. Phys. Chem. Lett. **3**, 2069 (2012)

[125]
A.D. Stoycheva and S.J. Singer, *Computer simulations of a two-dimensional system with competing interactions*, Physical Review E **65**, 036706 (2002)

[126]
R. Rüger and R. Valentí, *Pattern formation in the dipolar Ising model on a two-dimensional honeycomb lattice*, Phys. Rev. B **86**, 024431 (2012)

[127]
M.C. Blüm *et al*, *Probing and locally modifying the intrinsic electronic structure and the conformation of supported nonplanar* molecules, Phys. Rev. B **73**, 195409 (2006)

[128]
T. Yokoyama *et al*, *Nonplanar adsorption and orientational ordering of porphyrin molecules on Au(111)*, J. Chem. Phys. 115, 3814 (2001)

[129]
L. Gross *et al*, *Tailoring molecular self-organization by chemical synthesis: Hexaphenylbenzene, hexa-peri-hexabenzocoronene, and derivatives on Cu (111)*, Phys. Rev. B **71**, 165428 (2005)

[130]
D. Écija *et al*, *Molecular conformation, organizational chirality, and iron metalation of meso-tetramesitylporphyrins on copper(100)*, J. Phys. Chem. C **112**, 8988 (2008)

[131]
S.R. Forrest, *The path to ubiquitous and low-cost organic electronic appliances on plastic*, Nature **428**, 911 (2004)

[132]
C. Brabec *et al*, *Plastic solar cells*, Adv. Funct. Mater. **11**, 15 (2001)

[133]
T.-C. Tseng *et al*, *Charge-transfer-induced structural rearrangements at both sides of organic/metal interfaces*, Nat. Chem. **2**, 374 (2010)

[134]
G. Heimel *et al*, *Charged and metallic molecular monolayers through surface-induced aromatic stabilization*, Nat. Chem. **5**, 187 (2013)

[135]
M.N. Faraggi *et al*, *Bonding and charge transfer in metal-organic coordination networks on Au(111) with strong acceptor molecules*, J. Phys. Chem. **C** 116, 24558 (2012)

[136]
T.R. Umbach *et al*, *Atypical charge redistribution over a charge-transfer monolayer on a metal*, New J. Phys. **15**, 083048 (2013)

[137]
C. Wäckerlin *et al*, *Assembly of 2D ionic layers by reaction of alkali halides with the organic electrophile 7,7,8,8-tetracyano-p-quinodimethane (TCNQ)*, Chem. Commun. **47**, 9146 (2011)

[138]
M. Garnica *et al*, *Long-range magnetic order in a purely organic 2D layer adsorbed on epitaxial graphene*, Nat. Phys. **9**, 368 (2013)

[139]
N. Abdurakhmanova *et al*, *Stereoselectivity and electrostatics in charge-transfer Mn- and Cs-TCNQ$_4$ networks on Ag(100)*, Nat. Commun. **3**, 940 (2012)

[140]
N. Abdurakhmanova *et al*, *Superexchange-mediated ferromagnetic coupling in two-dimensional Ni-TCNQ networks on metal surfaces*, Phys. Rev. Lett. **110**, 027202 (2013)

[141]
T.-C. Tseng *et al*, *Hierarchical assembly and reticulation of two-dimensional Mn- and Ni–TCNQx (x=1,2,4) coordination structures on a metal surface*, J. Phys. Chem. C **115**, 10211 (2011)

[142]
R. Otero *et al*, *Molecular self-assembly at solid surfaces*, Adv. Mater. **23**, 5148 (2011)

[143]
W. Erley and H. Ibach, *Vibrational spectra of tetracyanoquinodimethane (TCNQ) adsorbed on the Cu(111) surface*, Surf. Sci. **178**, 565 (1986)

[144]
I. Fernandez-Torrente *et al*, *Structure and electronic configuration of TCNQ layers on a Au(111) surface*, Int. J. Mass Spectrom. **277**, 269 (2008)

[145]
J.I. Martinez *et al*, *Simulating the organic-molecule/metal interface TCNQ/Au(111)*, Phys. Status Solidi B **248**, 2044 (2011)
[146]
T. Katayama *et al*, *Reactive rearrangements of step atoms by adsorption and asymmetric electronic states of tetrafluoro-tetracyanoquinodimethane on Cu(100)*, Phys. Rev. B **83**, 153403 (2011)

[147]
R. Smoluchowski, *Anisotropy of the electronic work function of metals*, Phys. Rev. **60**, 661 (1941)

[148]
J. Tersoff and L.M. Falicov, *Electronic structure and local atomic configurations of flat and stepped (111) surfaces of Ni and* Cu, Phys. Rev. B **24**, 754 (1981)

[149]
G. Henkelman *et al*, *A fast and robust algorithm for Bader decomposition of charge density*, Comput. Mater. Sci. **36**, 254-360 (2006)

[150]
I. Fernandez-Torrente *et al*, *Vibrational Kondo effect in pure organic charge-transfer assemblies*, Phys. Rev. Lett. **101**, 217203 (2008)

[151]
I. Fernandez-Torrente *et al*, *Gating the Charge State of Single Molecules by Local Electric Fields*, Phys. Rev. Lett. **108**, 036801 (2012)

[152]
S. Kervyn, N. Kalashnyk, M. Riello *et al*, *“Magic” surface clustering of borazines driven by repulsive intermolecular forces*, Angew. Chem. Int. Ed. **52**, 7410 (2013)

[153]
Z.Q. Liu and T.B. Marder, *B-N versus C-C: How Similar Are They?*, Angew. Chem. Int. Ed. **47**, 242 (2008)

[154]
L. Ci *et al*, *Atomic layers of hybridized boron nitride and graphene domains*, Nat. Mater. **9**, 430 (2010)

[155]
A. Stock and E. Pohland, *Borwasserstoffe, IX: $B_3N_3H_6$*, Ber. Dtsch. Chem. Ges. B **59**, 2215 (1926)

[156]
M. Corso *et al*, *Boron nitride nanomesh*, Science **303**, 217 (2004)

[157]
J. Xue *et al*, *Scanning tunneling microscopy and spectroscopy of ultra-flat graphene on hexagonal boron nitride*, Nat. Mater. **10**, 282 (2011)

[158]
K. Watanabe *et al*, *Far-ultraviolet plane-emission handheld device based on hexagonal boron nitride*, Nat. Photonics **3**, 591 (2009)

[159]
S. Kervyn *et al*, *Polymorphism, fluorescence, and optoelectronic properties of a borazine derivative*, Chem. Eur. J. **19**, 7771 (2013)

[160]
A. Wakamiya *et al*, *Toward pi-conjugated molecule bundles: synthesis of a series of B,B',B''-trianthryl-N,N',N''-triarylborazines and the bundle effects on their properties*, J. Am. Chem. Soc. **127**, 14859 (2005)

[161]
F. Rosei *et al*, *Organic molecules acting as templates on metal surfaces*, Science **296**, 328 (2002)

[162]
L. Gross *et al*, *Trapping and moving metal atoms with a six-leg molecule*, Nat. Mater. **4**, 892 (2005)

[163]
A.K. Rappé *et al*, *UFF, a full periodic table force field for molecular mechanics and molecular dynamics simulations*, J. Am. Chem. Soc. **114**, 10024 (1992)

[164]
T. Classen *et al*, *Templated growth of metal-organic coordination chains at surfaces*, Angew. Chem. Int. Ed. **44**, 6142 (2005)

[165]
L.-A. Fendt *et al*, *Modification of supramolecular binding motifs induced by substrate registry: Formation of self-assembled macrocycles and chain-like patterns*, Chem. Eur. J. **15**, 11139 (2009)

[166]
J. Chaiken and J. Goodisman, *Interpreting magic-numbers and evaporation effects in cluster size distributions*, J. Cluster Sci. **6**, 319 (1994)

[167]
J.V. Barth *et al*, *Supramolecular architectures and nanostructures at metal surfaces*, Appl. Phys. A **76**, 645 (2003)

[168]
C.C. Perry *et al*, *Face specificity and the role of metal adatoms in molecular reorientation at surfaces*, Surf. Sci. **409**, 512 (1998)

[169]
N. Lin *et al*, *Two-dimensional adatom gas bestowing dynamic heterogeneity on surfaces*, Angew. Chem. Int. Ed. **44**, 1488 (2005)

[170]
N.V. Smith and C. T. Cohen, *Distance of the image plane from metal surfaces*, Phys. Rev. B **40**, 7565 (1989)

Acknowledgments

It feels a bit weird to find myself in front of a last empty page, thinking about the three years and half spent quite far from the place I used to call home, for a good quarter of a century, and that it is not anymore. I was working in a Chemical Engineering faculty and living in a small village in the heart of the Venetian countryside. Then I left to embark in a PhD in Physics, in a huge city, with no friends at all and the need to start all over again.

In this respect, I want to thank my supervisor, *Prof De Vita*, for having considered me up for the task from the very beginning. I still remember his call, five minutes after having sent my application! This first chat was filled with his enthusiasm, which he always put in every problem we tackled ever since then. A big thank also to *Andrea*, who has thought me everything I know about quantum mechanics (starting from scratch). A special mention goes to *Ada*, for all the discussions and theories developed during countless Skype calls and endless mail exchanges. She is the best teammate possible!

I was lucky enough to have friends (who happen to be also good physicist) willing to read through my work, giving precious advices and support. Thank you *Chiara* and *Giulia*!

It is impossible to appropriately mention all the friends I have left in Italy and that I always feel close to me. They make me feel as if I hadn't ever left, every single time I come back. Like the immutable warmth of my family house, where I will soon come back to hug my beloved niece *Sara*.

Last, I want to thank *Elena* for all the time spent together and for all that still have to be.